Deadbeat Direct Torque and Flux Control (DB-DTFC) Algorithm Evaluation and Optimization for Automotive Traction Applications

By
Mario Peña López

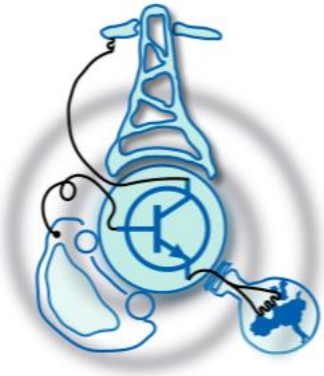

Submitted to the Department of Electrical Engineering, Electronics, Computers and Systems
in partial fulfillment of the requirements for the degree of
Erasmus Mundus Joint Master Degree in Sustainable Transportation and Electrical Power Systems
at the
UNIVERSIDAD DE OVIEDO
September 2019

Author……...
Mario Peña López

Certified by……..…….
Michael Saur
Dr. -Ing
Thesis Supervisor

Certified by……..…….
Pablo Garcia
Associate Professor
Thesis Supervisor

Deadbeat Direct Torque and Flux Control (DB-DTFC) Algorithm Evaluation and Optimization for Automotive Traction Applications

By
Mario Peña López

Submitted to the Department of Electrical Engineering, Electronics, Computers and Systems
On August 30th, 2019, in partial fulfillment of the requirements for the degree of Erasmus Mundus Joint Master Degree in Sustainable Transportation and Electrical Power Systems

Abstract

This research project studies the application of Deadbeat Direct Torque and Flux Control (DB-DTFC) for its implementation with Interior Permanent Magnet Synchronous Machines (IPMSMs) in traction applications.

DB-DTFC is a discrete control method that can achieve the desired torque and flux commands in one sampling instant. The voltage command generation process and the controller nature have great potential for providing a more efficient and effective control strategy particularly around the voltage limit and for high speed operation

First, the state of the art was considered and the operation of DB-DTFC in the MTPA and MTPF regions was studied. Particularly, the Square Root Condition (SRC) method applied to the DB-DTFC algorithm was proven to be a viable MTPF strategy with better performance than classic Current Vector Control (CVC) approaches.

Second, the capabilities of the already implemented systems presented. For the development of this project a testbench was available that provided opportunities for better analysis of the behaviour of the drive.

Finally, the concept of overmodulation is studied for its application to DB-DTFC. Multiple reference adaptation methods were tested, as well as classic Direct Torque Control (DTC) strategies and a new algorithm for six-step voltage selection emerging from the DB-DTFC insights was introduced.

Thesis Supervisor: Michael Saur
Title: Dr. -Ing

Thesis Supervisor: Pablo García
Title: Associate Professor

Acknowledgements

First, I would like to thank the teachers, coordinators and fellow students and friends from EMJMD STEPS. Taking part on this program has provided me with the experience of a lifetime, both personally and professionally. In particular, thanks to the professors of University of Oviedo and specially to Prof. Pablo Garcia, who has been my supervisor for this thesis as well as my bachelor thesis, and has always provided good advice and mentoring throughout my academic career.

Next, I am greatly thankful to Dr. -Ing. Michael Saur, for the opportunity to develop my thesis with Audi and his guidance during this project. This has been an amazing learning experience and I look forward to keeping working with you in the future. Also, thanks to Hadi El Khatib for the assistance and insightful conversations, as well as to Dr. -Ing. Harald Hofmann for his support at the testbench.

Finally, my immeasurable gratitude goes to my family, who has been the greatest support through all the good and the bad.

Contents

List of Figures

List of Tables

List of Symbols

Symbols	Description
$V_{ds}{}^{r}$, V_{ds}	d-axis stator voltage
$V_{qs}{}^{r}$, V_{qs}	q-axis stator voltage
V_{dq}	dq-stator voltage vector
V_s	Stator voltage amplitude
V_{s1}	Stator voltage first harmonic component amplitude
V_α	α-axis stator voltage
V_β	β-axis stator voltage
$V_{\alpha\beta}$	αβ-stator voltage vector
$u_{\alpha\beta}$	Normalized αβ- stator voltage vector
u_a	Normalized a-phase stator voltage
V_{max}	Maximum stator voltage
V_{dc}	DC bus voltage
$i_{ds}{}^{r}$, i_{ds}	d-axis stator current
$i_{qs}{}^{r}$, i_{qs}	q-axis stator current
i_{dq}	dq-voltage stator current
$i_{\alpha\beta}$	αβ-voltage stator current
i_s	Stator current amplitude
I_{max}	Maximum stator current
$\lambda_{ds}{}^{r}$, λ_{ds}	d-axis stator flux linkage
$\lambda_{qs}{}^{r}$, λ_{qs}	q-axis stator flux linkage
λ_{qd}	dq-stator flux linkage vector
λ_s	Stator flux linkage amplitude
δ	Stator flux linkage angle in the dq-reference frame

λ_α	α-axis stator flux linkage
λ_β	β-axis stator flux linkage
$\lambda_{\alpha\beta}$	αβ-stator flux linkage vector
R_s	Stator resistance
L_d	d-axis stator inductance
L_q	q-axis stator inductance
λ_{pm}	Permanent magnet flux
ω_r , ω_e	Rotor electrical angular speed
T_{em}	Electromagnetic airgap torque
P	Machine pole pairs
t	Time
λ_s^*	Stator flux command
${\Delta T_{em}}^*$	Differential torque command
M_D	DB-DTFC differential torque line slope
B_D	DB-DTFC differential torque line q-intercept
λ_{ds1}	d-axis flux decoupling term
λ_{qs1}	q-axis flux decoupling term
M	Modulation index
d_a	Phase a duty command
χ	Stator flux linkage limit for positive slope near zero flux angle
B'	DB-DTFC null change in torque line q-intercept
B_k	k-six-step voltage projection in the volt-second q-axis
l_k	k-six-step voltage distance to the flux circle centre
$U_d Ts_k$	k-six-step voltage d-coordinate in the synchronous reference frame
$U_q Ts_k$	k-six-step voltage q-coordinate in the synchronous reference frame
${\lambda^{ref}}_{max}$	Limit for flux reference saturation in the flux weakening region
k_{margin}	Voltage margin limit applied to $\lambda_{\max FW}$
λ_{MTPA}	Stator flux linkage MTPA reference
T^a	Temperature
$\lambda_{ds\ MTPF}$	d-axis stator flux linkage MTPF operating point
$i_{ds\ MTPF}$	d-axis stator current MTPF operating point
$i_{qs\ MTPF}$	q-axis stator current MTPF operating point

Chapter I

State of the Art

1.1. Role of Electrical Machines in Traction Applications

Electric vehicles are a key part of the transition of the transportation industry towards more sustainable technologies. According to [1], the basic characteristics that machines and drives must fulfil for traction applications include:

- High torque density and power density
- High torque for starting, at low speed and hill climbing, and high power for high speed cruising
- Wide speed range, with a good compromise between peak torque requirement of the machine and the inverter ratings
- High efficiency over wide speed and torque ranges
- Intermittent overload capability
- High reliability and robustness appropriate to the vehicle environment
- Acceptable cost
- Low acoustic noise and low torque ripple

Given these requirements, the most common electrical machines employed for traction applications are Induction Machines (IM) and Permanent Magnet Synchronous Machines (PMSM).

IMs are a more mature technology, they are robust, relatively low cost and have a simple construction [2]. However, they have reduced efficiency with respect to PMSMs due to the joule losses in the rotor conductors.

Alternatively, PMSMs avoid these losses with the use of permanent magnets (PM), require less cooling and provide a higher torque and power density. However, they increase material costs due to the use of rare earth materials [3]. Interior Permanent Magnet Synchronous Machines (IPMSM) have an even greater advantage due to the additional torque resultant from rotor saliency, extended speed range, better thermal and mechanical robustness and good overload capacity [4].

1.2. IPMSM Modelling and Operation

In IPMSMs the magnets are located below the surface of the rotor, providing two distinct flux line paths with different reluctances (saliency) as seen in Figure 1.1 [5]. These machines are most simply modelled in the rotor reference frame (d-q) and their anisotropy is captured in the different values of the axes inductances.

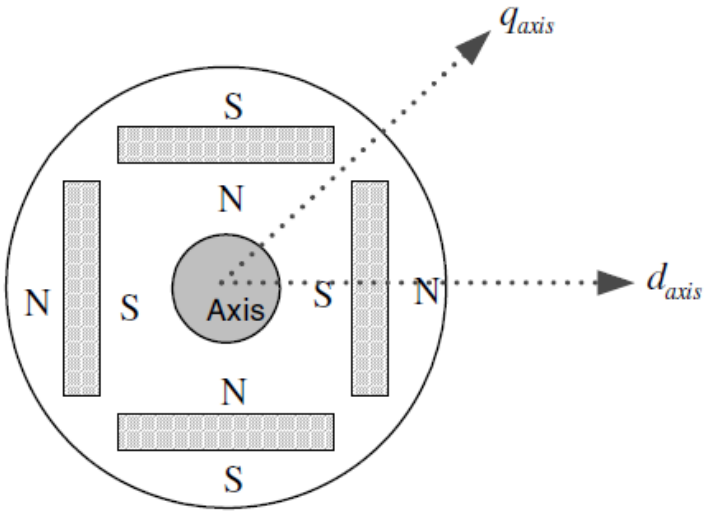

Figure 1.1: Schematic representation of a four-pole IPMSM [5].

The reference frame convention used during this report is shown in Figure 1.2 [5].

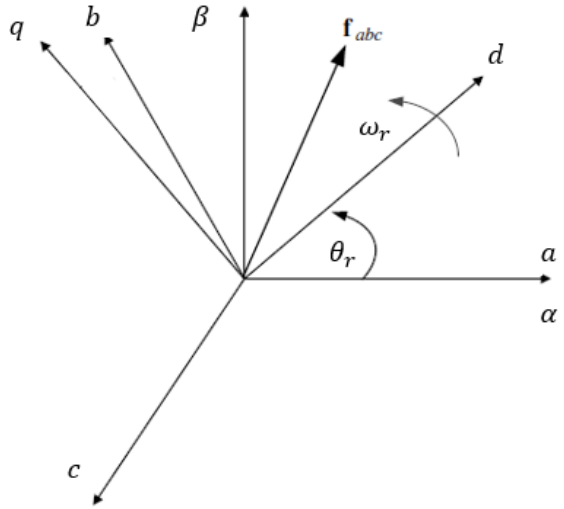

Figure 1.2: Convention used for transformation between rotor (dq) and stator (αβ or abc) reference frames [5].

In IPMSMs, the stator voltage and stator flux equations can be expressed in scalar form as

$$V_{ds}{}^{r} = R_s i_{ds}{}^{r} + \frac{d\lambda_{ds}{}^{r}}{dt} - \omega_r \lambda_{qs}{}^{r} \tag{1.1}$$

$$V_{qs}{}^{r} = R_s i_{qs}{}^{r} + \frac{d\lambda_{qs}{}^{r}}{dt} + \omega_r \lambda_{ds}{}^{r} \tag{1.2}$$

$$\lambda_{ds}{}^{r} = L_d i_{ds}{}^{r} + \lambda_{pm} \tag{1.3}$$

$$\lambda_{qs}{}^{r} = L_q i_{qs}{}^{r} \tag{1.4}$$

In all equations hereafter the dq-subindexes will always refer to the rotor reference frame, and super-index ‘r’ is omitted for simplicity. For stator reference frame variables, the subindexes αβ or abc are used. Throughout the report, the RMS convention is used, and the equations will refer to stator variables unless stated otherwise.

The electromagnetic torque developed in the airgap can be expressed as

$$T_{em} = \frac{3P}{2}(\lambda_{pm} + (L_d - L_q) i_{ds}) i_{qs} \tag{1.5}$$

As it can be seen in Eq. 1.5, the torque has a magnetic component due to the interaction between permanent magnet flux and the stator current, and a reluctance component that appears when there is a non-zero current in the d-axis, due to the difference between the

inductances. Since the inductance is lower in the d-axis than in the q-axis, a negative value of the d-axis current increases the torque.

1.2.1. IPMSM Physical Limits

The operation of AC drives with a PWM inverter is limited by the available voltage and current limitations (given by thermal constraints of the machine and inverter). The goal of any control algorithm will be to obtain the desired behaviour while maintaining the operation within the constraints and maximizing efficiency. The drive losses have multiple components (copper losses, iron losses, switching losses, stray losses, …). In general terms, the copper losses are dominant at low speeds, and the iron losses become more significant with increasing speeds. Switching losses are dependent on switching frequency and output power. Stray losses combine the effect of mechanical losses and other phenomena difficult to estimate, which are most significant at very high speeds.

It is useful to interpret the drive limits in terms of the contours they form in the dq-current plane. For the current limit, the constraint is given by Equation 1.6, which forms a circle. The current dynamics are limited by the stator time constants, and so the current limit affects mostly the steady state operation limit.

$$i_{ds}^2 + i_{qs}^2 < I_{max} \tag{1.6}$$

The consideration of the voltage limit is more complex, since it limits both the transient (the maximum change in current or flux in a single period is directly proportional to the applied voltage) and steady state capabilities of the drive. The voltage setpoint must fulfil Equation 1.7

$$V_{ds}^2 + V_{qs}^2 < V_{max} \tag{1.7}$$

The value of V_{max} will depend on the DC bus voltage and the modulation technique used (Sine-triangle, triplen harmonic injection, Space Vector Modulation, …). In case of overmodulation, the maximum voltage also depends on the angle (hexagon limit). The concept of overmodulation and maximum utilization of inverter voltage is explored in Chapter IV.

The voltage constraint imposes limits on the machine performance. The flux in the rotating machine creates an electromotive force (back-EMF), generating a voltage in the stator

windings that needs to be compensated by the inverter to maintain a certain operating point. Therefore, with increasing speed, the flux in the machine will need to be reduced in order to stay within the voltage limit. This is done through flux weakening techniques. Considering the voltage equations (Eq. 1.1, 1.2) in steady state, under the assumption of null stator resistance and expressing the flux in terms of current (Eq. 1.3, 1.4), the voltage limit can be rewritten as Equation 1.8, which forms an ellipse in the dq-current plane

$$\left(L_d i_{ds} + \lambda_{pm}\right)^2 + \left(L_q i_{qs}\right)^2 < \left(\frac{V_{max}}{\omega_r}\right)^2 \tag{1.8}$$

It should be noted that the consideration of stator resistance modifies the shape of the voltage limit (the axes of the ellipse will no longer be parallel to the dq-axes). However, the ellipse given by Equation 1.8 represents the points with equal flux regardless of other effects (if the values of the inductances are correctly estimated). This notion will be important in Chapter II, where the MTPF operation is discussed.

1.2.2. IPMSM Operating Regions

The limits discussed in the previous section can be observed in the dq-current plane in Figure 1.3 [5], as well as the operating regions of the machine. In Figure 1.4 the same regions are represented terms of maximum torque, flux, current and voltage with respect to speeed.

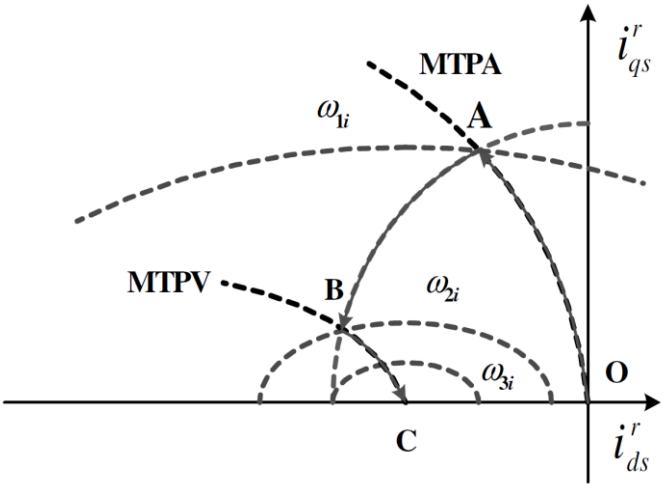

Figure 1.3: IPMSM operating regions in the dq-current synchronous reference frame [5]

The operation of electrical machines can generally be divided into two regions: the constant torque region below base speed; and the flux-weakening region above base speed. For those PMSMs in which the short circuit current is smaller than the current limit (i.e. they

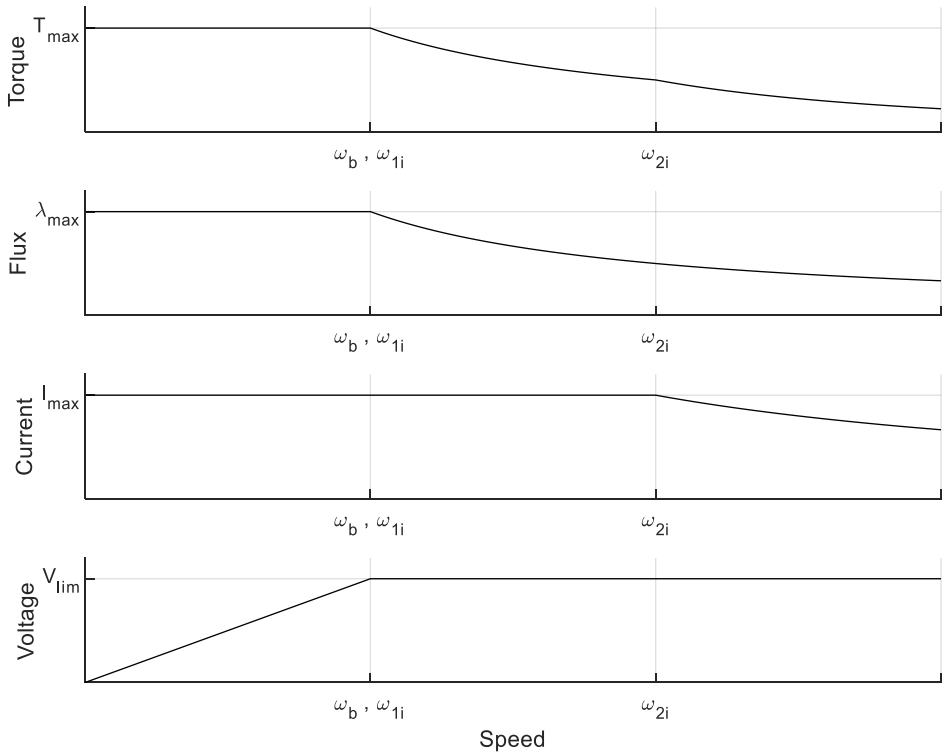

Figure 1.4: IPMSM maximum performance curves with respect to speed.

$$I_{max} > \left|\frac{-\lambda_{pm}}{L_d}\right| \tag{1.9}$$

fulfil the condition in Equation 1.9), the latter region is split in two: the first and second flux weakening regions. The short circuit current is the centre of the flux (or voltage) ellipses. These machines are also referred to as infinite speed drives, since there is no maximum speed given by the electromagnetic constraints. This is not true in reality, as other phenomena will prevent the operation beyond a certain speed.

The main characteristics of the IPMSM operating regions are as follows:

- Constant torque region: The operation is limited by the maximum current. The efficiency in this region is dominated by the copper losses, and so the most common strategy for controlling the machine is to follow the Maximum Torque per Ampere (MTPA) path. Maximum torque performance will be achieved in the intersection between the MTPA line and the current limit (point A in Figure 1.3).
- First flux weakening region: with increasing speed, the required voltage for maximum performance increases (Figure 1.4), and the voltage limit ellipse decreases. At a certain speed, the voltage reaches the limit (base speed ω_b or ω_{1i}).

From this point forward, the flux must be decreased (inversly proportionally to the speed increase) to stay within the voltage limit. Maximum torque performance will be obtained at the current limit (arc from A to B in Figure 1.3).

- Second flux weakening region: at a certain speed (ω_{2i}), the maximum torque for the same voltage (or flux) ellipse is not found at the current limit. If the operation was continued at the current limit, the maximum torque in this speed range would be reduced and the drive could not go beyond a certain speed (ω_{3i}). Form this point forward, maximum torque performacnce can only be achieved by operating at the Maximum Torque per Flux (MTPF) or Maximum Torque per Voltage (MTPV) path (path from B to C in Figure 1.3).

The operation in the MTPA and MTPF regions is further explored in detail in Chapter II.

1.3. IPMSM Control Methods

1.3.1. Current Vector Control (CVC)

The most widely used approach for control of IPMSMs is the use of Current Vector Control (CVC) in a synchronous reference frame with the rotor (Field Oriented Control) [6]. This method applies the knowledge of the operation of the machine in the dq-current plane to recreate the desired behaviour through independent closed loop control of the d- and q-currents. A general block diagram for CVC implementation is shown in Figure 1.5 [5].

While this method offers very good current dynamics and allows for the use of classic control theory analysis and design tools, it has several disadvantages. With this strategy, both airgap torque and stator flux are open loop variables [7]. The reference generation is often based on a precalculated Look-Up-Table (LUT) for optimum performance (for example for MTPA or MTPF reference), which is very sensitive to parameter estimation errors. Moreover, the controller dynamics are compromised close to the voltage limit, causing integrator windup and poor torque dynamics when the machine operates at high speed. Finally, flux weakening techniques are challenging and difficult to implement to guarantee maximum drive performance at high speeds. The controller performance can be improved with the use of anti-windup techniques, feedforward compensation and other methods.

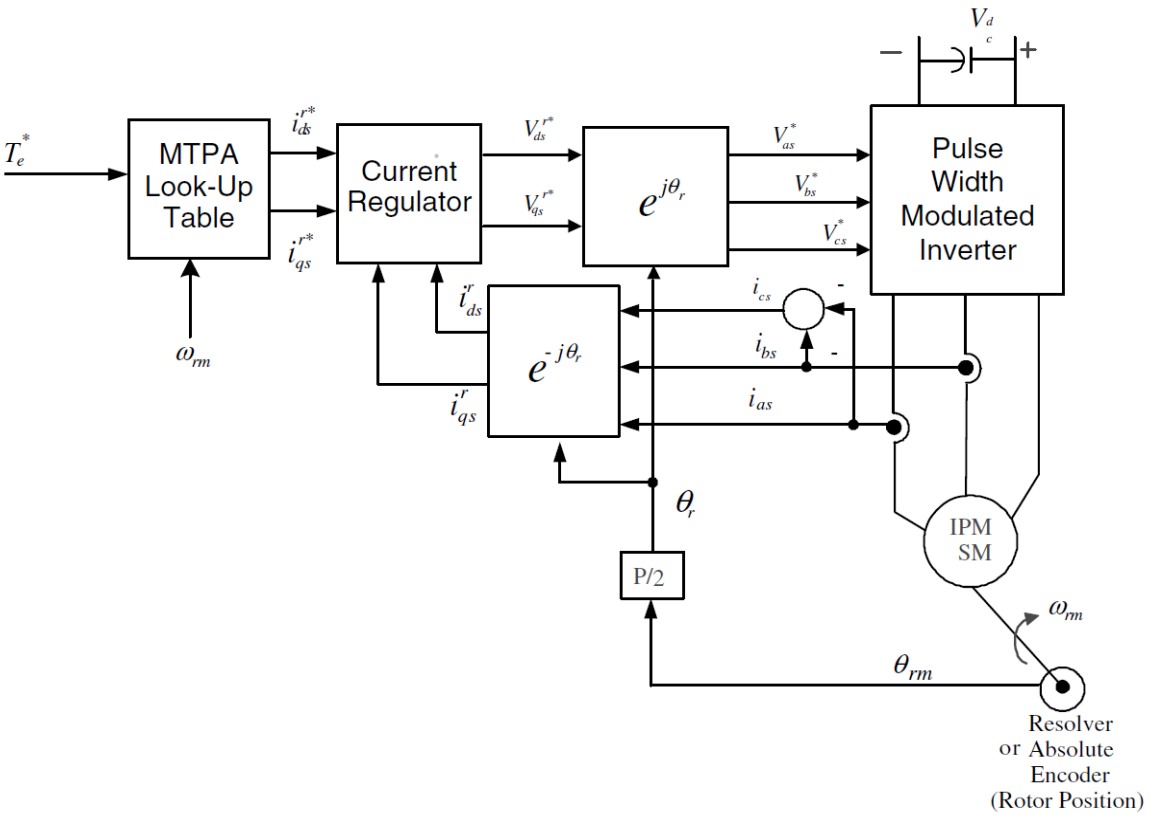

Figure 1.5: CVC control block diagram for IPMSM [5]

1.3.2. Direct Torque Control (DTC)

The application of Direct Torque Control (DTC) was introduced for PMSMs over two decades ago [8] after it had been presented for induction drives. Previously, several attempts to introduce torque control for PMSMs had been implemented by combining it with the current controllers or substituting one of them, but these methods suffered from the same problems of parameter sensitivity and armature dynamics that affect current control.

The idea behind DTC is to select the proper stator voltage vector to control the change in torque and flux based on the angle change and amplitude of the stator flux linkage. A switching table will select a voltage based on the output of two hysteresis controllers tracking the desired change in torque and flux. This voltage will be applied until the command is different or the selected voltage no longer produces the desired change (the switching frequency is not constant). The general control scheme is shown in Figure 1.6.

To achieve this, DTC operates under the assumption that the derivative of torque with respect to the flux angle (δ) is always positive. Under this condition, it is possible to select

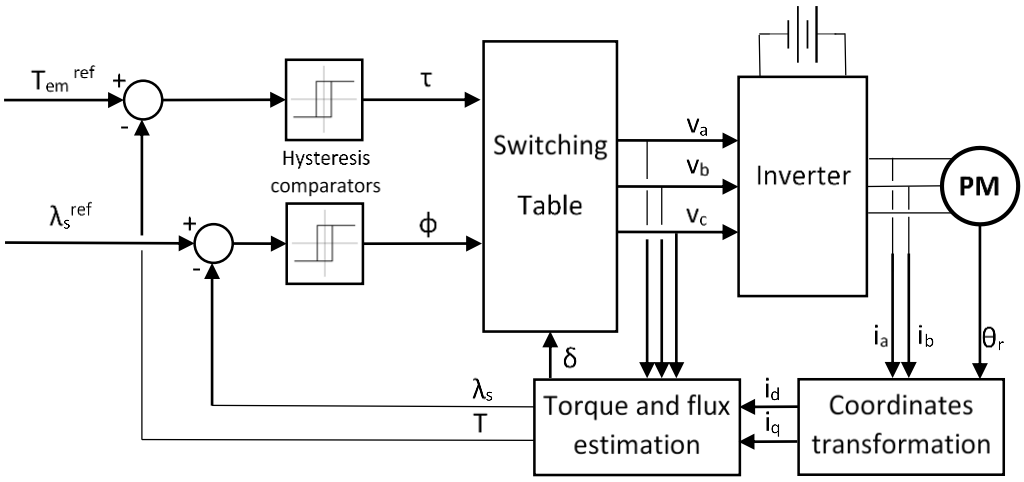

Figure 1.6: DTC control block diagram for IPMSMs.

the applied voltage so that the direction of change in flux angle and amplitude produces the desired direction of change in torque and flux. For the selection of the appropriate voltage, the volt-second plane is divided into six regions according to the current position of the stator flux as seen in Figure 1.7 [9], and the voltage selection is done following the switching table in Table 1.1.

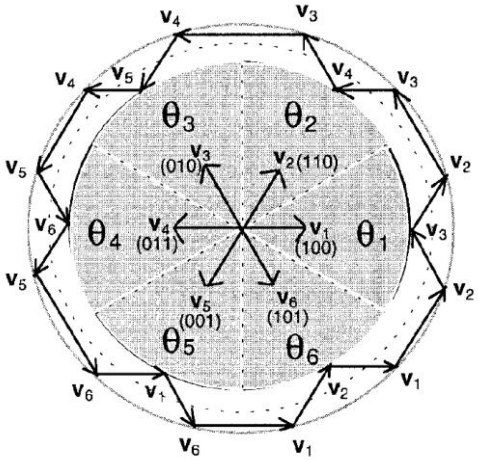

Figure 1.7: Stator voltage control in DTC using six votage vectors [9].

ϕ	τ	θ					
		θ(1)	θ(2)	θ(3)	θ(4)	θ(5)	θ(6)
ϕ = 1	τ = 1	V_2(110)	V_3(010)	V_4(011)	V_5(001)	V_6(101)	V_1(100)
	τ = 0	V_6(101)	V_1(100)	V_2(110)	V_3(010)	V_4(011)	V_5(001)
ϕ = 0	τ = 1	V_3(010)	V_4(011)	V_5(001)	V_6(101)	V_1(100)	V_2(110)
	τ = 0	V_5(001)	V_6(101)	V_1(100)	V_2(110)	V_3(010)	V_4(011)

Table 1.1: DTC Switching table for IPMSM control [8].

In each of the regions, the two voltage vectors in the directions closest to being parallel with the flux vector (e.g. in section 1, voltage vectors V_1 and V_4) are not used, as the other four voltage vectors can achieve the desired change while giving the minimum switching frequency [8]. Since for PMSMs the stator flux will change even when zero voltage vectors are applied due to the permanent magnet, these voltage configurations (V_0 and V_7) are not used.

DTC offers the advantage of closed loop control of airgap torque and stator flux, which are the fastest possible dynamics (within the limitations of stator voltage) [7]. However, it requires non-constant switching frequency which produces unpredictable ripple in torque and current, degrading the control dynamics. Other similar methods have been introduced, as Direct Mean Torque Control (DTMC) or the use of additional systems in the control method to improve the performance.

1.3.3. Deadbeat-Direct Torque and Flux Control (DB-DTFC)

Deadbeat Direct Torque and Flux Control (DB-DTFC) combines the concepts of deadbeat control and DTC. It uses a digital control technique in which the inverse machine model is solved for the inputs (dq-voltage) that would achieve the desired outputs (airgap torque and stator flux) in just one PWM period ("dead in one beat") [7]. DB-DTFC was introduced for induction machines [10], where it was shown to be simple to implement and demonstrated low sensitivity to parameter estimation errors. This method can also be used in the voltage limit with no degradation to the control performance, considering the physical limits of the drive. The use of DB-DTFC for controlling IPMSMs was introduced in [7].

The block diagram for the DB-DTFC algorithm is shown in Figure 1.8 [11]. The implementation of DB-DTFC requires the use of a stator current and flux observer. They are needed to obtain the necessary knowledge for the inverter machine model and calculate the airgap torque in the next sampling instant for closed loop control. In this project, other ancillary systems were implemented to improve or guarantee the operation within the machine limits:

- MTPA flux command (orange): in DB-DTFC the flux is used as the degree of freedom to define the operating point for a given torque. In the constant torque

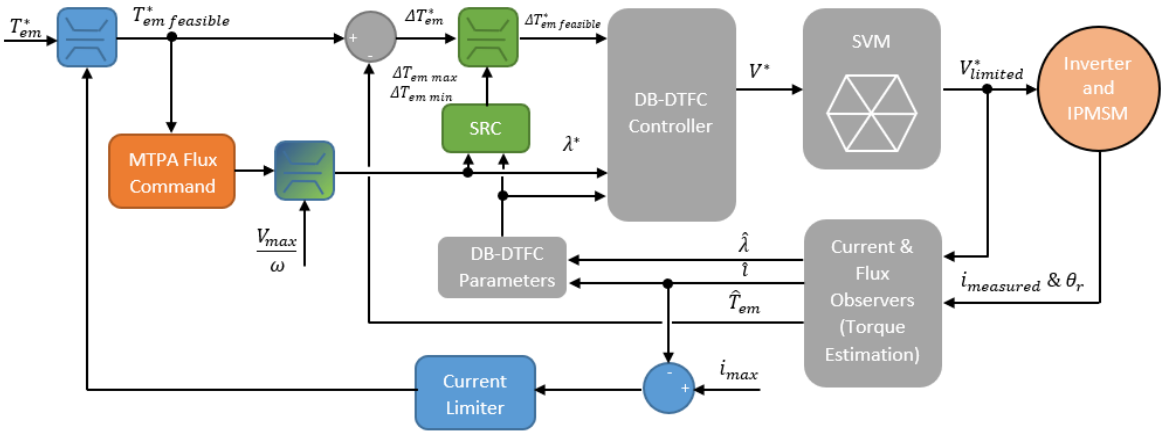

Figure 1.8: Block diagram of DB-DTFC algorithm. Grey: necessary features of the DB-DTFC algorithm; Orange: systems acting during constant torque region; Blue: systems acting during the first flux weakening region; Green: systems acting during the second flux weakening region [11].

region, the operation is optimized by the MTPA path at each given torque, so a reference generation stage is implemented. This feature is studied in Section 2.1.

- Current limiter and torque command saturation (blue): in DB-DTFC the current is an open loop variable. To guarantee that the operation does not exceed the machine and inverter thermal constraints, an external loop is implemented. It reduces the torque command when the operation exceeds the current limit with a dynamic non-parameter dependent scheme [12].
- Flux weakening saturation (blue/green): flux weakening strategies are very simple in DB-DTFC, as the flux is a controlled variable. A reference saturation stage is included in which the limit is defined by the available DC bus voltage and the speed. This stage could include a closed loop voltage controller similar to the current control implemented.
- SRC and differential torque command saturation (green): the SRC is an inherent feature of DB-DTFC that achieves MTPF operation in the second flux weakening region [11]. This feature is studied in Section 2.2.

1.3.3.1. DB-DTFC Algorithm for IPMSMs

The algorithm presented hereafter was developed in [7]. Starting from Equations 1.1 to 1.5, the differential flux equation can be expressed as Equations 1.10 and 1.11. The derivatives of stator currents can also be expressed in terms of the stator flux as Equations 1.12 and 1.13.

$$\dot{\lambda_{ds}} = V_{ds} + \frac{R_s}{L_d}(\lambda_{ds} - \lambda_{pm}) + \omega_r \lambda_{qs} \tag{1.10}$$

$$\dot{\lambda_{qs}} = V_{qs} + \frac{R_s}{L_q}\lambda_{qs} - \omega_r \lambda_{ds} \tag{1.11}$$

$$\dot{\iota_{ds}} = \frac{\dot{\lambda_{ds}}}{L_d} \tag{1.12}$$

$$\dot{\iota_{qs}} = \frac{\dot{\lambda_{qs}}}{L_q} \tag{1.13}$$

The inversed machine model is based on solving the differential torque equation for the stator voltage. The differential torque equation can be obtained as

$$T_{em} = \frac{3P}{2}(\lambda_{ds} i_{qs} - \lambda_{qs} i_{ds}) \tag{1.14}$$

$$\dot{T_{em}} = \frac{3P}{2}(\dot{\lambda_{ds}} i_{qs} + \lambda_{ds}\dot{\iota_{qs}} - \dot{\lambda_{qs}} i_{ds} - \lambda_{qs}\dot{\iota_{ds}}) \tag{1.15}$$

The differential torque line can be rewritten in discrete form as

$$\dot{T_{em}} = \frac{T_{em}(k+1) - T_{em}}{T_s} \tag{1.16}$$

$$\begin{aligned}
&\frac{T_{em}(k+1) - T_{em}}{T_s} \\
&\quad = \frac{3P}{2}\left[V_{ds}(k)\lambda_{qs}(k)\left(\frac{L_d - L_q}{L_d L_q}\right)\right. \\
&\quad + V_{qs}(k)\frac{(L_d - L_q)\lambda_{ds}(k) + \lambda_{pm} L_q}{L_d L_q} \\
&\quad + \frac{\omega_r(k)}{L_d L_q}\Big((L_q - L_d)\big(\lambda_{ds}(k)^2 - \lambda_{qs}(k)^2\big) - L_q \lambda_{ds}(k)\lambda_{pm}\Big) \\
&\quad \left. + \frac{R_s \lambda_{qs}(k)}{{L_d}^2 {L_q}^2}\Big(\big({L_d}^2 - {L_q}^2\big)\lambda_{ds}(k) - {L_q}^2 \lambda_{pm}\Big)\right]
\end{aligned} \tag{1.17}$$

For a command change in torque as given by Equation 1.18, Eq. 1.17 can be rewritten as Equation 1.19

$$\Delta T_{em}(k) = T_{em}(k+1) - T_{em}(k) \tag{1.18}$$

$$V_{qs}(k) T_s = M_D V_{ds}(k) T_s + B_D \tag{1.19}$$

where

$$M_D = \frac{-\left(L_d - L_q\right)\lambda_{qs}(k)}{\left(L_d - L_q\right)\lambda_{ds}(k) + L_q\lambda_{pm}} \tag{1.20}$$

$$B_D = \frac{L_d L_q}{\left(L_d - L_q\right)\lambda_{ds}(k) + L_q\lambda_{pm}}\left[\frac{2\Delta T_{em}(k)}{3P} - \frac{\omega_r(k)T_s}{L_d L_q}\left(\left(L_q - L_d\right)\left(\lambda_{ds}(k)^2 - \lambda_{qs}(k)^2\right) - L_q\lambda_{pm}\lambda_{ds}(k)\right) - \frac{R_s T_s \lambda_{qs}(k)}{{L_d}^2 {L_q}^2}\left(\left({L_q}^2 - {L_d}^2\right)\lambda_{ds}(k) - {L_q}^2\lambda_{pm}\right)\right] \tag{1.21}$$

Equation 1.19 is the locus of points in the dq-volt-second plane that will achieve the desired change in torque and takes the shape of a line. To simultaneously control the total flux Equation 1.22 must be considered

$$\lambda_s^{*2} = \lambda_s(k+1)^2 = \lambda_{ds}(k+1)^2 + \lambda_{qs}(k+1)^2 \tag{1.22}$$

Considering the discrete form of Equations 1.10 and 1.11, this can be rewritten as

$$\lambda_s^{*2} = (V_{ds}(k)T_s + \lambda_{ds1})^2 + \left(V_{qs}(k)T_s + \lambda_{qs1}\right)^2 \tag{1.23}$$

where λ_{ds1} and λ_{qs1} are the flux decoupling terms and can be expressed as

$$\lambda_{ds1} = -R_s i_{ds}(k)T_s + \omega_r(k)T_s\lambda_{qs}(k) + \lambda_{ds}(k) \tag{1.24}$$

$$\lambda_{qs1} = -R_s i_{qs}(k)T_s - \omega_r(k)T_s\lambda_{ds}(k) + \lambda_{qs}(k) \tag{1.25}$$

Equation 1.23 is the locus of points in the dq-volt-second plane that will achieve the desired flux, and takes the shape of a circle. Solving the system of equations given by 1.19 and 1.23, a soluiton can be found that achieves the command change in torque at the desired stator flux in the next sampling instant. Depending on the relative location of the differential torque line and the flux circle, multiple solutions may fulfill both conditions. In this case, the one corresponding to a smaller stator voltage amplitude will be selected.

1.3.3.2. Graphical Interpretation of DB-DTFC Algorithm

The equations presented in the previous section can be represented graphically in the volt-second plane as Figure 1.9 [7]. In this figure, the differential torque line is represented in red, the reference flux circle and the hexagon voltage limit in black, and the two voltage solutions for achieving the desired control output in blue. The graphical representation changes as

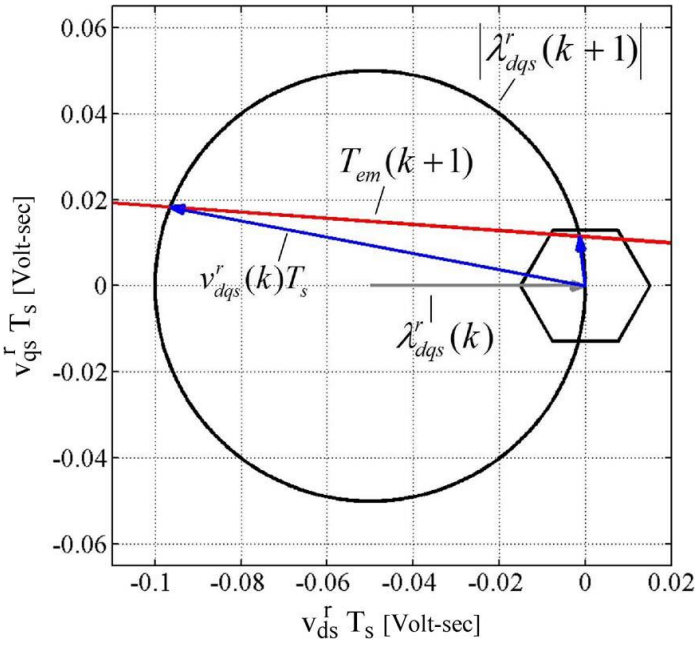

Figure 1.9: Graphical interpretation of the DB-DTFC algorithm [7]

operating conditions and parameters vary [13]. It can be observed how of the two solutions, only one is within the voltage constraints for this case. From the DB-DTFC algorithm other geometries can be generated that are useful to the understanding of the transient and steady state behaviour of the drive.

For example, the contour representing the current limit under steady state and null stator resistance assumptions takes the shape of an ellipse with centre in the q-volt-second axis. The radius and q-axis coordinate of its centre will increase with increasing speed as seen in Figure 1.10 [14]. Some attempts were made in this project to include this and other representations of the current limit (considering transient phenomena) in the control

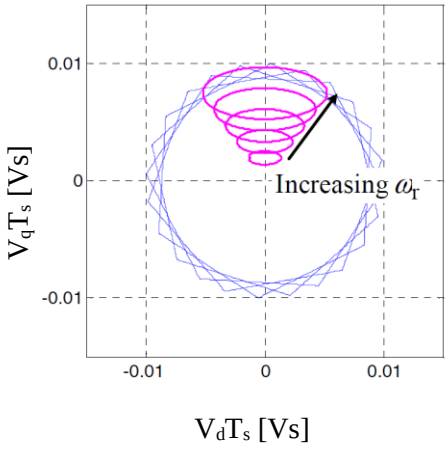

Figure 1.10: Current limit for increasing speed in the DB-DTFC algorithm [14]

algorithm for consideration of current constraints and the creation of a dynamic MTPA operating point calculation but this effort was not successful.

1.3.3.3. Current and Flux Observers

The design, optimization, tuning and analysis of the current and flux observers was a main focus of the previous stage of this project [15], and where developed from the systems presented in [7].

To satisfy the requirement of current estimation at the next sampling instant, a discrete time Luenberger-style stator current observer in the rotor reference frame is used (Figure 1.11). The current observer is based on the IPMSM state equations and the cross-coupling decoupling terms are added as feed-forward signals to the system.

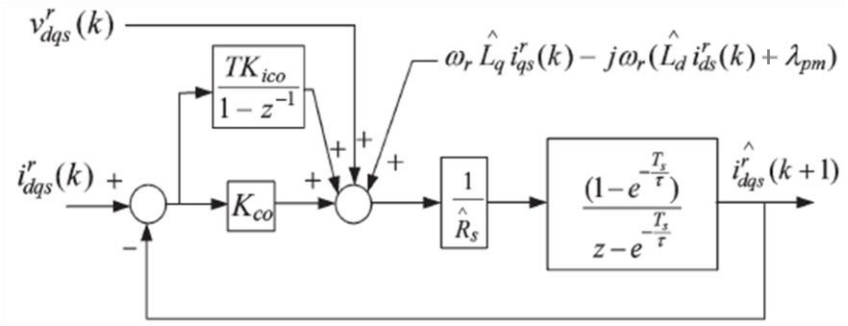

Figure 1.11: Block diagram of the implemented discrete time Luenberger-style stator current observer [7]

For the estimation of the stator flux in the next sampling instant, a Gopinath-style flux observer is used. The implemented observer was designed according to Figure 1.12. This structure combines the use of a current model at low speeds with a voltage model at high

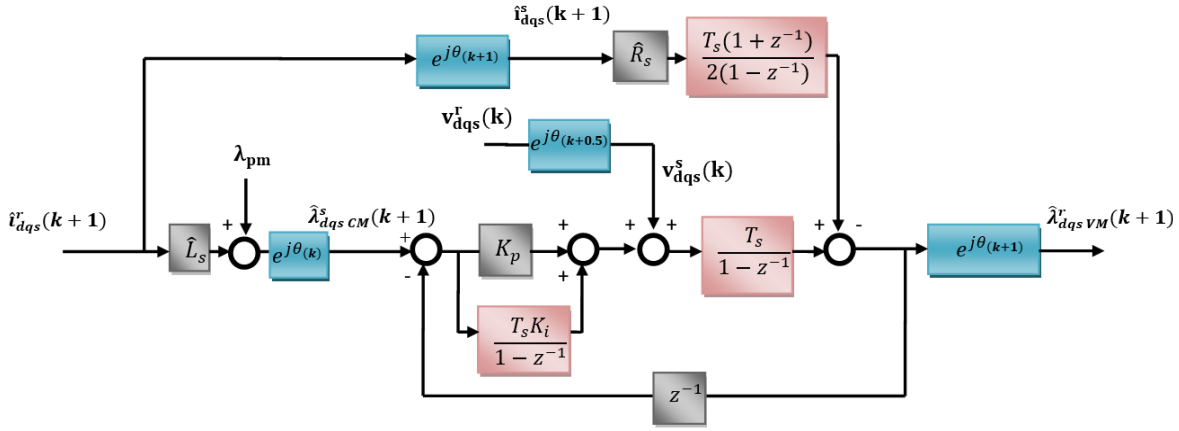

Figure 1.12: Block diagram of the implemented discrete time Gopinath-style stator flux observer [15]

speeds. The transition between the two models is governed by a PI controller, whose bandwidth determines the speed at which the voltage model starts being dominant. The design and tuning of the observer is a challenging task and must take into account the signal types (for continuous-time to discrete-time conversion), the angle used in each of the coordinate transformations and the feedforward compensation terms.

The observers estimate the operation in the next sampling instant to overcome unwanted system dynamics due to sampling and computational delays. The processor discrete timing diagram for DB-DTFC is shown in Figure 1.13 [16]. The command stator voltage for instant (k+1) is calculated between (k) and (k+1), removing computational delays by virtue of the predictive nature of the observers.

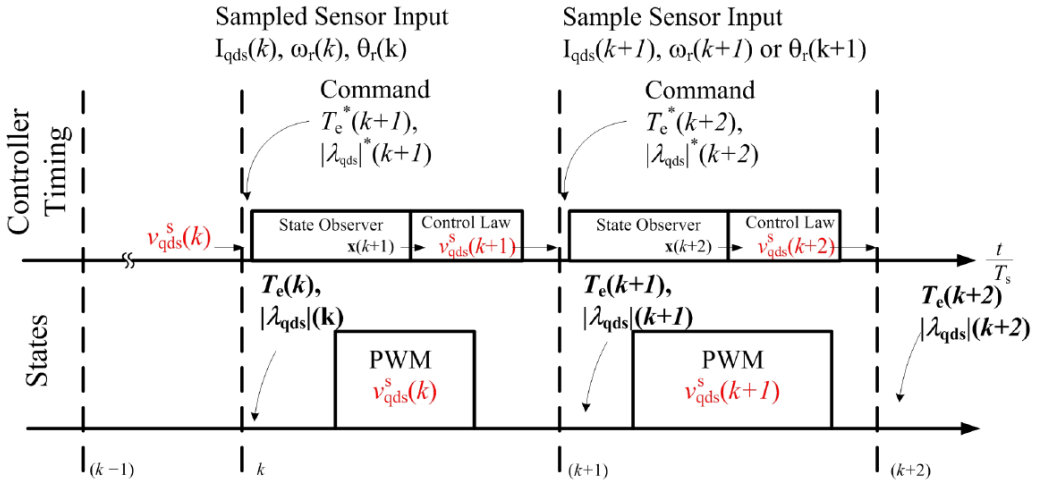

Figure 1.13: Processor discrete timing diagram for DB-DTFC [16]

1.4. Motivation

The motivation for the study of DB-DTF as opposed to other methodologies as CVC or DTC lies in the superior torque dynamics achievable, the lack of performance degradation when operating close to the voltage limit and the ease of implementation of flux weakening strategies.

In previous stages of this project, the behaviour of DB-DTFC in all operating regions was studied and simulated [12]; special emphasis was later put in the implementation in a testbench through a dSPACE system and optimization of the current and flux observers [15]. These stages demonstrated great capabilities and insensitivity to parameter estimation errors.

The goal of this stage was to study and optimize the behaviour of the system in the MTPA and MTPF regions, with special emphasis on the capabilities of DB-DTFC against established CVC methods; make better use of the testbench equipment to study and evaluate the system behaviour and performance; and explore the operation at the voltage limits and the opportunities for operating in the overmodulation region.

1.5. Research Opportunities

The main body of this report is structured around the following research opportunities:

- With classic CVC control, the operation for maximum performance in the constant torque region and second flux weakening region is attempted following the MTPA and MTPF paths respectively. Alternatively, DB-DTFC does not follow current references. In Chapter II Section 1, several methods to address the MTPA operation through appropriate flux reference generation are explored. Chapter II Section 2 studies the application of the Square-Root-Condition, a feature emerging from the DB-DTFC algorithm, that inherently achieves MTPF operation. The behaviour of DB-DTFC is evaluated analytically, numerically and experimentally under perfect and erroneous parameter estimation, and the operation is compared with several CVC methods
- The testbench used during the project was equipped with multiple measurement instruments and three of the systems provided an opportunity for easily exporting data: an 8-channel oscilloscope (LeCroy MDA); the dSPACE system itself which allowed the storage of signals during operation; and a labview application logging and organizing multiple sensors including torque, speed, temperature, mechanical harmonics in the gearbox, and data from a precision power analyser. However, no tool had been developed to easily combine and analyse the data in a convenient way. Chapter III describes the systems included in the testbench, the tools developed for processing of the data obtained and some examples of the analysis opportunities this provides.
- DB-DTFC can operate at the voltage limit without degradation to the performance (within physical limits). The intuitive voltage command generation and graphical interpretation of the algorithm allow to understand and study the operation in these

conditions in a much simpler way than CVC, whose operation degrades close to the voltage limit, and DTC, that only employs six voltage vectors to achieve the desired behaviour. The concept of overmodulation in DB-DTFC is explored in Chapter IV, with the implementation of classic reference adaptation techniques and the creation of a new algorithm for six-step voltage selection based on the ideas presented in [13] and [17].

Chapter II

MTPA and MTPF for DB-DTFC

2.1. MTPA Operation

2.1.1. Introduction

At low speeds, the total drive losses are dominated by the total current (joule losses) [18]. For this reason, control strategies attempt to produce the maximum torque at the minimum current, following the Maximum Torque per Ampere (MTPA) path. For each current, a unique id-iq combination exists that can maximize the torque. In the dq-current plane, this corresponds to the point in which a torque line is tangent to a current circle, as seen in Figure 2.1.

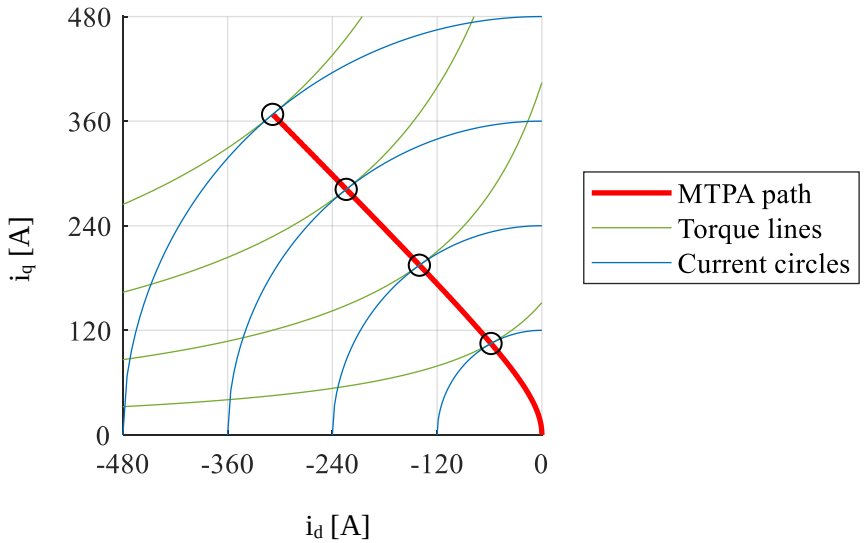

Figure 2.1: Geometric representation of the MTPA line in the dq-current plane

This is done in CVC controllers by following a reference in both currents produced by a pre-calculated Look-up-Table (LUT) in terms of torque. For DB-DTFC, there exists two degrees of freedom due to the inputs to the control. Ideally, the torque reference guarantees the operation at the desired torque. Therefore, the flux reference is used as the degree of freedom to control the operation of the drive. In the same way that the MTPA path can be pre-calculated to obtain the dq-pair for a certain torque, the total flux can be obtained as well. This is shown in Figure 2.2,where the x- and y-axis are normalized with respect to maximum torque and permanent magnet flux respectively.

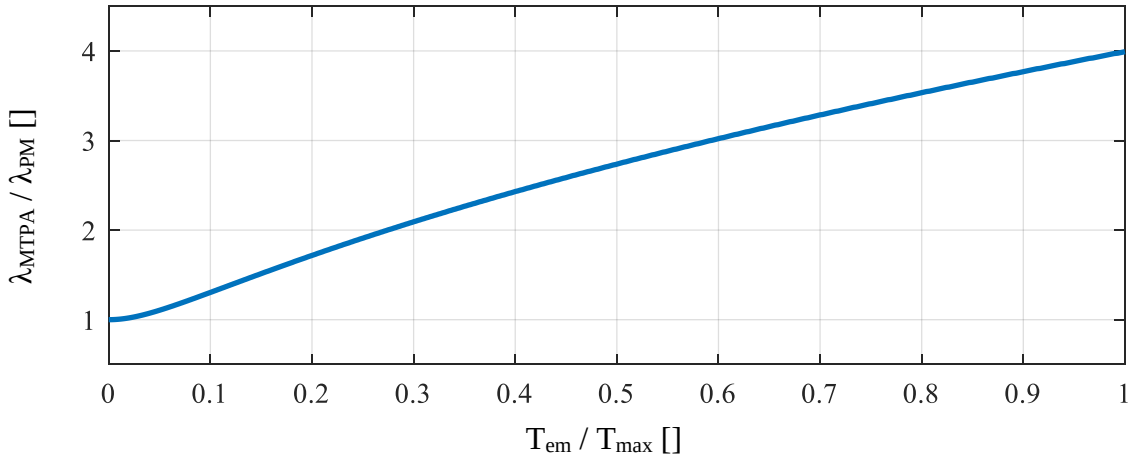

Figure 2.2: Normalized MTPA flux reference based on desired airgap torque.

While this approach is effective, there are two main problems with it:

- Parameter estimation errors in the pre-calculation produce deviations from the true MTPA path, increasing the losses of the drive.
- The LUT are a computational burden on the system if they must be accessed in a fast task.

2.1.2. MTPA Flux Approximations

In an effort to solve these issues, several approximation methods were studied to minimize the computational effort through approximations and the sensitivity to parameter errors, in particular for permanent magnet flux. Permanent magnet flux errors are common since its value is very sensitive to rotor temperature changes (a temperature increase of 100 K reduces the PM flux around 10% [5]).

There are two critical points for the estimation of the MTPA flux reference:

- Null torque command: generating a reference different from the permanent magnet flux would cause the drive to unnecessarily spend current, either weakening or strengthening the d-axis flux, in all regions.
- Maximum torque command: if the reference at maximum current is different from the true MTPA point, the performance of the drive is degraded in terms of maximum torque and power.

The first of these issues is addressed with the addition of the permanent magnet flux estimation to methods 2 to 4. The models were developed and tested considering operating point dependent machine parameters and introducing temperature differences to compare the reference generated with the true MTPA flux. The permanent magnet flux estimation would include these temperature differences.

1. Method 1: Single LUT based on the pre-calculated MTPA flux

$$\lambda_{MTPA\,1} = LUT(T_{em}^{*}) \tag{2.1}$$

2. Method 2: First order approximation including real time permanent magnet flux estimation

$$\lambda_{MTPA\,2} = k * T_{em}^{*} + \lambda_{pm} \tag{2.2}$$

3. Method 3: Substitution of the constant in Method 2 by a pre-calculated LUT

$$\lambda_{MTPA\,3} = LUT * T_{em}^{*} + \lambda_{pm} \tag{2.3}$$

4. Method 4: Modified approach including real time permanent magnet flux estimation

$$\lambda_{MTPA\,4} = (k * T_{em}^{*} + 1) * \lambda_{pm} \tag{2.4}$$

The results are shown for each method in Figure 2.3 and separated for each temperature scenario in Figure 2.4. The importance of accurate permanent magnet flux can be appreciated comparing the results shown in Figure 2.3 (a) at low torque with the rest. Method 1 is the only that does not include the permanent magnet flux estimation in the reference generation process, and so the command at low torque deviates from the real MTPA.

Methods 2 and 4 produce the highest relative error consistently, as seen in Figure 2.4, especially for temperatures deviating from the one at which the fitting was performed (90°C).

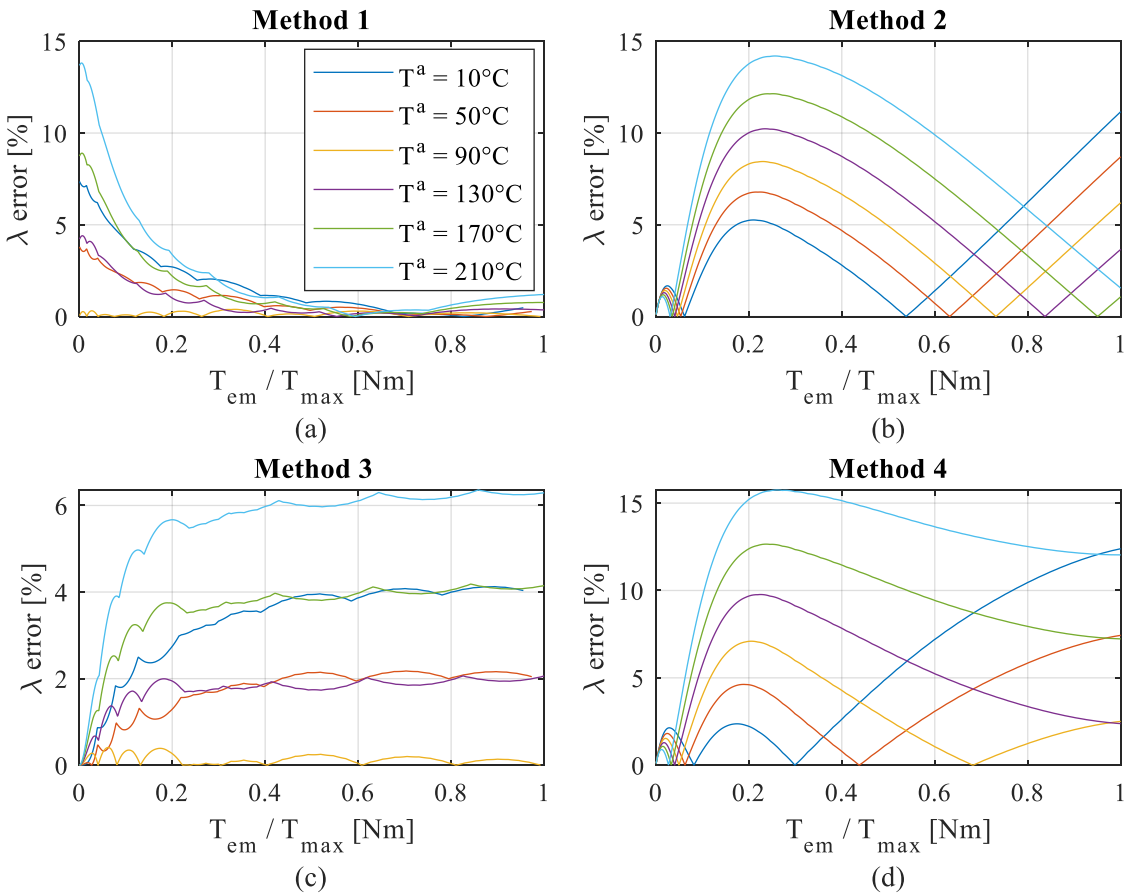

Figure 2.3: Evaluation of temperature variation on MTPA flux estimation error for the proposed approximation method in simulation.

The LUT in method 3 captures the nonlinearities in the MTPA flux, and it shows clear advantages over method 1 despite being the same kind of approximation.

Method 3 also shows great accuracy at low torque and is not very temperature dependent. However, at high torque it deviates significantly from the theoretical MTPA flux. For high torque operation, method 1 is consistently superior to the rest. This indicates a low dependency on permanent magnet flux during high torque operation.

Since no method offered a satisfying solution to the parameter sensitivity problem, the effect of permanent magnet flux variations was investigated more thoroughly. Figure 2.5 (a) shows the effect of permanent magnet estimation error on MTPA flux reference error. Each line in this figure corresponds to a different temperature throughout the torque range. By plotting together the points corresponding to the same torque, Figure 2.5 (b) is obtained. It was observed that the behavior was linear with respect to the change in permanent magnet

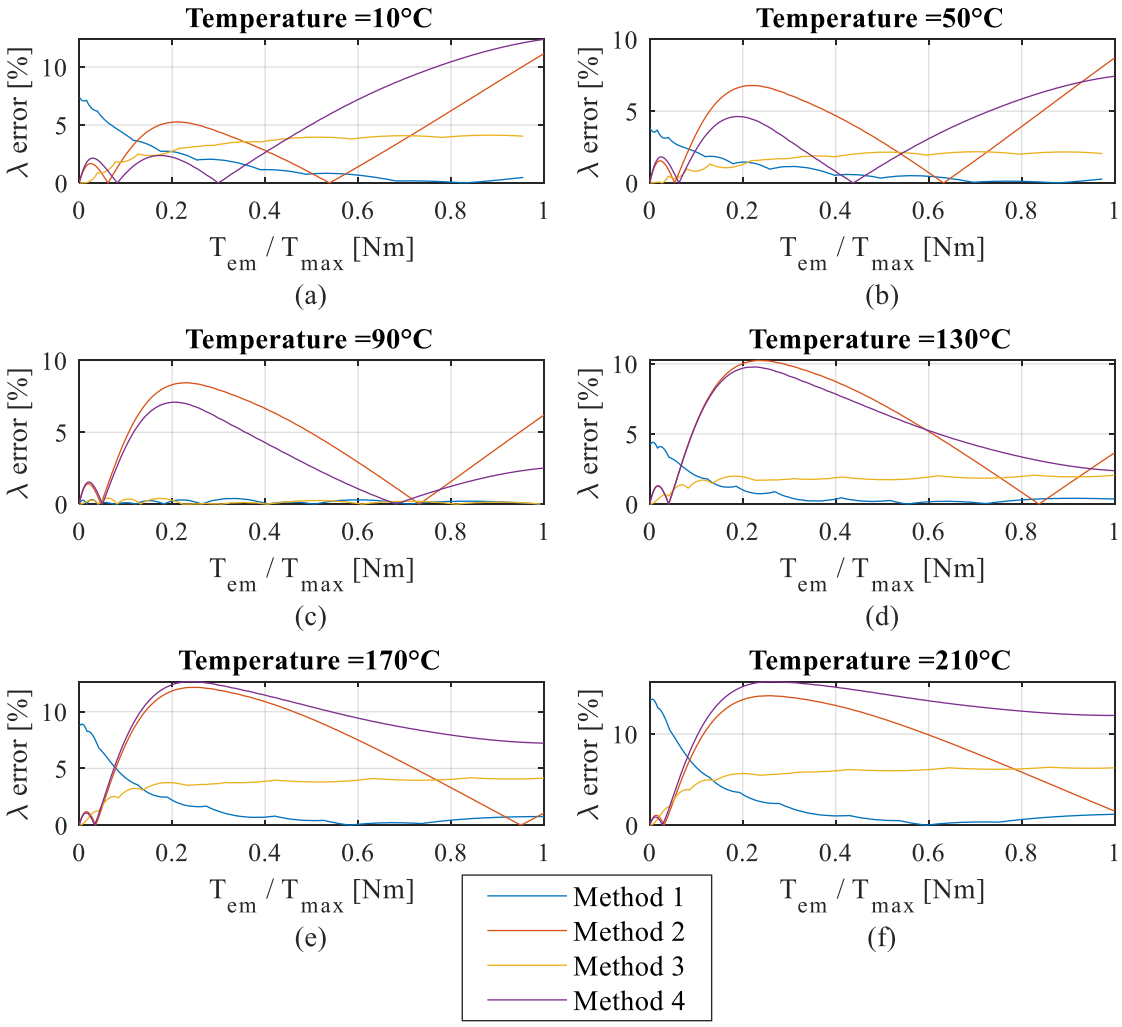

Figure 2.4: Comparisson of MTPA flux approximation error for the proposed methods methods in multiple temperature scenrios in simulation.

flux estimation. The slope of these lines was plotted against the torque they correspond to in Figure 2.5 (c). There is very little deviation between the slopes given by each of the points as evidenced by the proximity of the data points to the averaged line (black). Based on these results, a new method (method 5) is proposed as Equation 2.5

$$\lambda_{MTPA\,5} = LUT_1 + LUT_2 * (\lambda_{pm} - LUT_3) \tag{2.5}$$

In which LUT_1 is the same as in method 1, LUT_2 contains the information about the slope captured in Figure 2.5(c) and LUT_3 contains the information of the permanent magnet flux used for the calculation of LUT_1. All LUT take the torque command as input. The method was tested in simulation analogously to the previous ones and the results are shown in Figure 2.6. The lines correspond to the same temperatures as Figure 2.3.

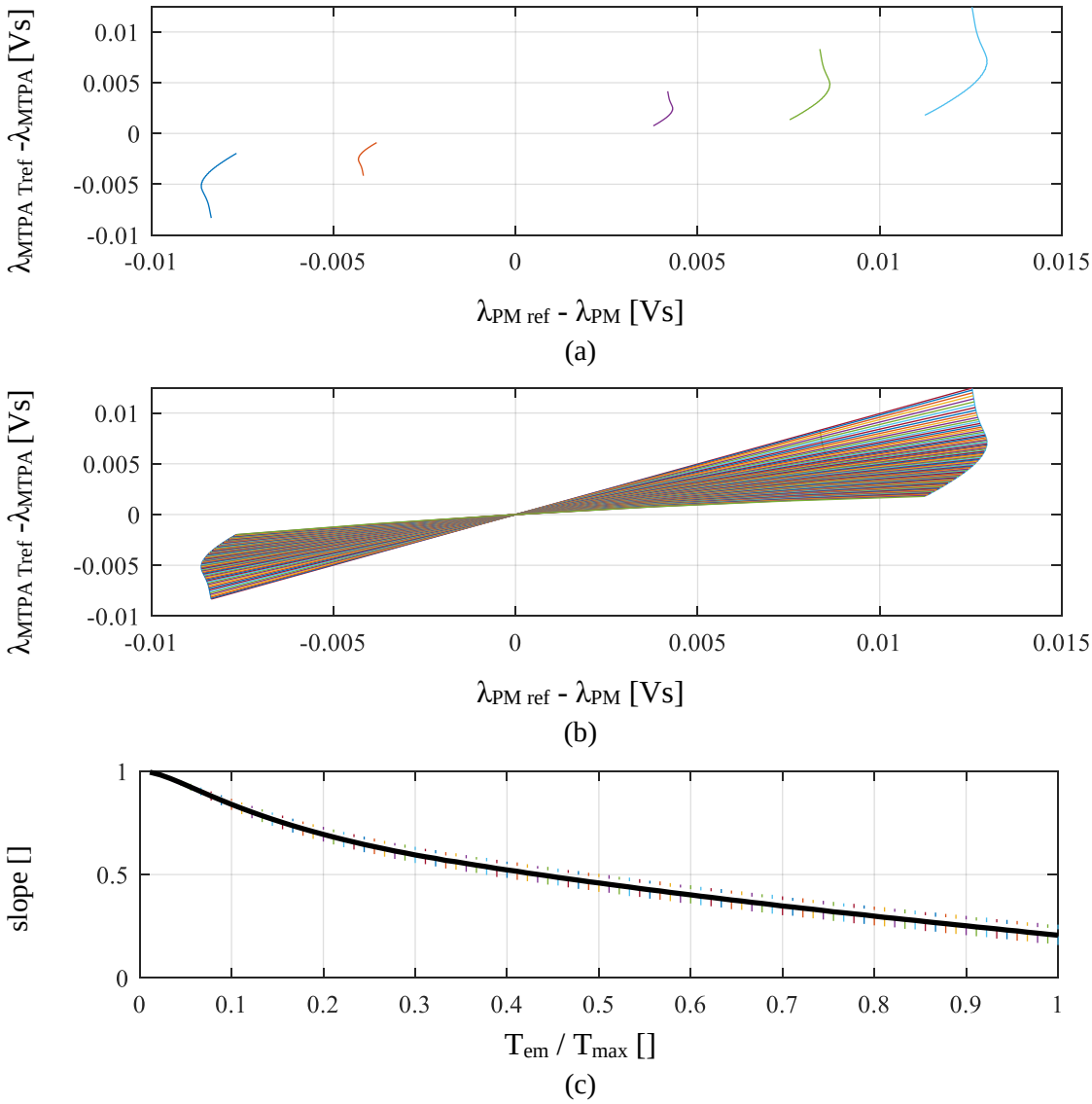

Figure 2.5. MTPA reference error evaluation based on permanent magnet estimation error.

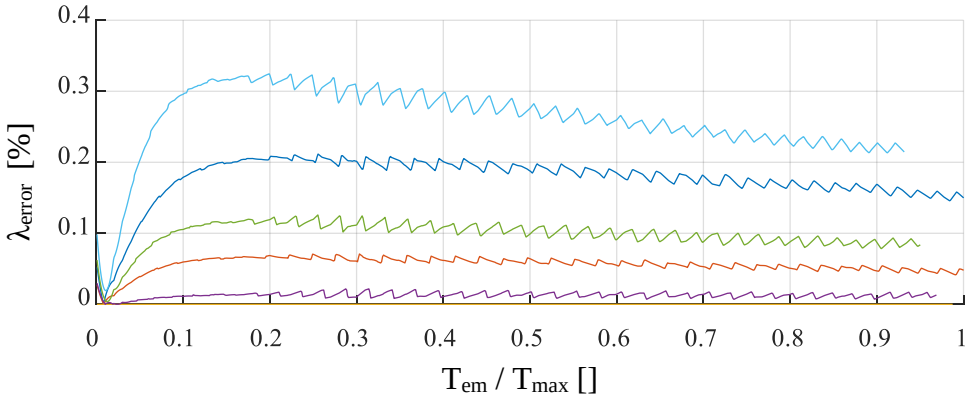

Figure 2.6. Evaluation of temperature variation on MTPA flux estimation error for the approximation method 5 in simulation.

The new method appears to drastically reduce the error, to a maximum of around 0.3% in the worst-case scenario. These results are shown for a high number of points in the LUT, and for time and task priority constraints it was not further optimized. The number of points of the LUT should be reduced in a tradeoff between computation time, memory and error in MTPA flux reference.

2.1.3. Experimental Results

The last method was implemented in the testbench with 10 points LUTs and compared to the previously used algorithm for the MTPA operation, which was Method 2 from the previous section. The speed was kept constant at 500 rpm and the torque command was increased in 10 Nm steps from 0 to 200 Nm. The test was replicated at four different rotor temperatures.

Figure 2.7 shows the saved data of total current with respect to the estimated torque from the dSPACE. In addition, an averaged line is superposed for clarity. The new method requires

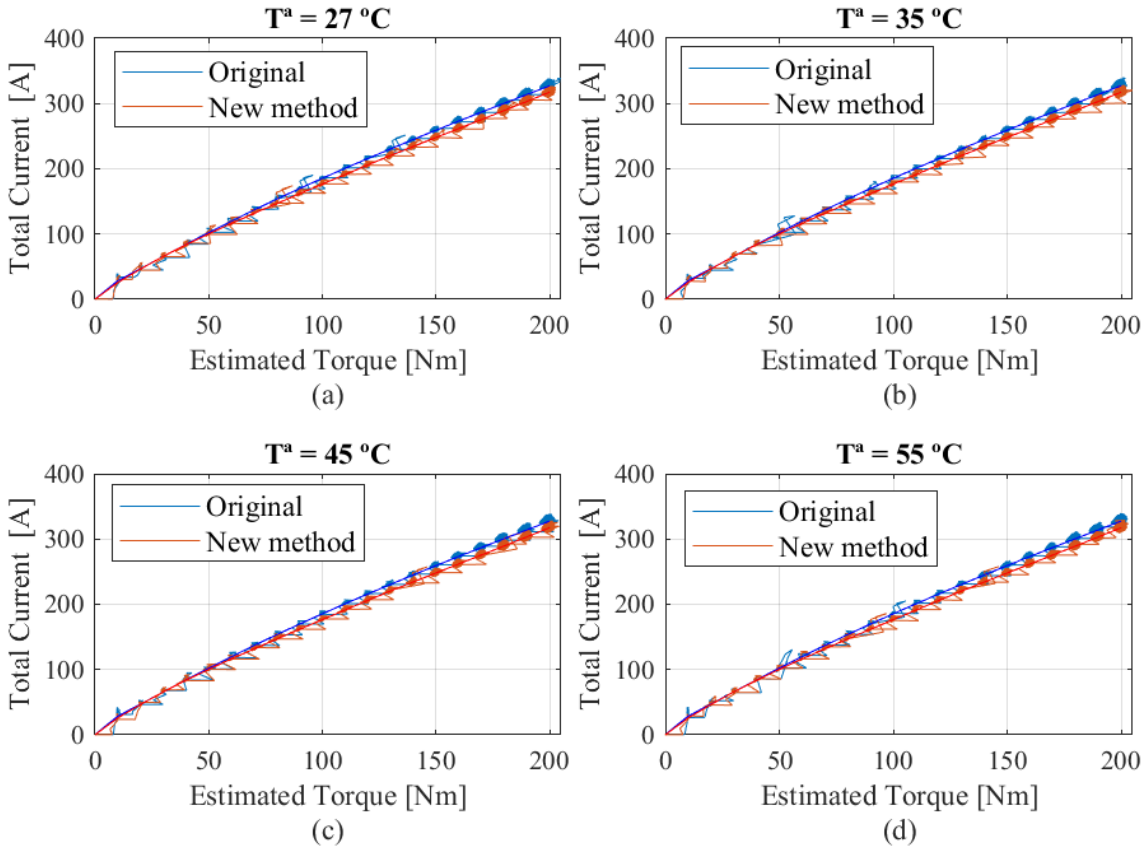

Figure 2.7: Experimental results comparing total current in the MTPA region (500 rpm) of orignal and new MTPA flux reference generation methods at different rotor temperatures at low speed.

less current to maintain the same torque, so it can be considered successful. However, no differences are observed in terms of temperature, which may be due to the temperature measurement was incorrect, the new method does not work as expected, or the torque estimation is incorrect. In simulation the temperature effect was directly applied to the permanent magnet, while in the experiment the actual rotor temperature may not have varied as expected. For this experiment no more data was saved from the rest of the measurement instruments. This method should be further tested and, in case of being selected for implementation, the location and number of points in the LUTs should be optimized.

2.1.4. Other Methods Considered

An attempt was made to create a dynamic MTPA reference generation based on the geometries in the DB-DTFC algorithm but was discarded for task priority and time constraints. It is possible that an appropriate flux reference can be obtained through the interaction between the current ellipse (either with or without considering the transient phenomena and stator resistance) and the differential torque line for null change in torque. In the same way as the center of the flux circle and the slope of the differential torque line are not dependent on the command (only on the machine parameters and the previous operating point), the same happens with the center of the current ellipse. Therefore, some algorithm optimizing the ellipse radius (and so minimizing the total current) to the final operating point (given in steady state by the differential torque line for null change in torque) should be attainable.

2.2. MTPF Operation

2.2.1. Introduction

As explained in Section 1.2.2, if the short circuit current is inside the current limit, above a certain speed the maximum torque can no longer be achieved by operating at the current limit. Here, the most limiting factor is the machine stator flux. The machine performance will be maximized by operating in the MTPF (also called MTPV, since the flux is limited by the available inverter voltage) i.e. for each flux there is a unique id-iq combination that can

maximize the torque. In the dq-current plane, this corresponds to the point in which a torque line is tangent to a flux ellipse, as seen in Figure 2.8.

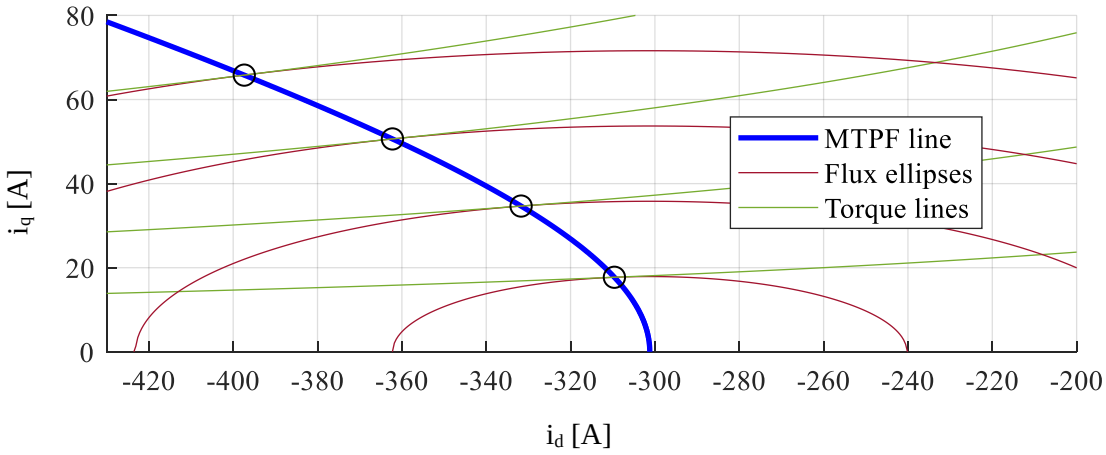

Figure 2.8: Geometric representation of the MTPF line in the dq-current plane

It is important to note that for the same flux ellipse within a big neighborhood of the MTPF point, an increase in distance to this point decreases torque. The equations for MTPF can be obtained by considering the torque Equation 2.6 in terms of the d-axis flux as Eq. 2.7

$$T_{em} = \frac{3}{2}P\left(\lambda_{ds}i_{qs} - \lambda_{qs}i_{ds}\right) \tag{2.6}$$

$$T_{em} = \frac{3}{2}P\left(\lambda_{ds}\frac{\sqrt{{\lambda_s}^2 - {\lambda_{ds}}^2}}{L_q} - \sqrt{{\lambda_s}^2 - {\lambda_{ds}}^2}\frac{\lambda_{ds} - \lambda_{pm}}{L_d}\right) \tag{2.7}$$

The solution for the operating point that maximizes torque for a given stator flux can be obtained by differentiating Eq. 2.7 with respect to the flux in the d-axis as Equation 2.8

$$\frac{\partial T_{em}}{\partial \lambda_{ds}} = 0 \;\Rightarrow 2\left(L_d - L_q\right){\lambda_{ds}}^2 + L_q\lambda_{pm}\lambda_{ds} - {\lambda_s}^2\left(L_d - L_q\right) = 0 \tag{2.8}$$

The quadratic equation can be solved as Eq. 2.9

$$\lambda_{ds\,MTPF} = \frac{-L_q\lambda_{pm} + \sqrt{\left(L_q\lambda_{pm}\right)^2 + 8\left(L_d - L_q\right)^2{\lambda_s}^2}}{4\left(L_d - L_q\right)} \tag{2.9}$$

Finally, using Equations 1.3 and 1.4 the current path can be obtained as Equation 2.10 and 2.11. This is illustrated in Figure 2.8.

$$i_{ds\,MTPF} = \frac{\lambda_{ds\,MTPF} - \lambda_{pm}}{L_d} \tag{2.10}$$

$$i_{qs\,MTPF} = \frac{\sqrt{{\lambda_s}^2 - {\lambda_{ds\,MTPF}}^2}}{L_q} \tag{2.11}$$

Moreover, under the assumption of null stator resistance, the maximum stator flux can be expressed as a function of the voltage limit and rotor electrical speed as Equation 2.12. Therefore, a relation between speed and d-axis current for MTPF can be calculated.

$$\lambda_{s\,max} = \frac{V_{max}}{\omega} \tag{2.12}$$

2.2.2. Square Root Condition Applied to the DB-DTFC Algorithm

As seen in Section 1.3.3.1, DB-DTFC generates the voltage references for the inverter by finding an intersection between the reference differential torque line (Eq. 2.13) and the reference flux circle (Eq. 2.14). This is done mathematically by solving the following system of equations

$$V_{qs}(k)T_s = V_{ds}(k)T_s M_D + B_D \tag{2.13}$$

$${\lambda_s^*}^2 = (V_{ds}(k)T_s + \lambda_{ds1})^2 + \left(V_{qs}(k)T_s + \lambda_{qs1}\right)^2 \tag{2.14}$$

where

$$M_D = \frac{-\left(L_d - L_q\right)\lambda_{qs}(k)}{\left(L_d - L_q\right)\lambda_{ds}(k) + L_q\lambda_{pm}} \tag{2.15}$$

$$\begin{aligned} B_D = \left(\frac{L_d L_q}{\left(L_d - L_q\right)\lambda_{ds}(k) + L_q\lambda_{pm}}\right)\Bigg[&\frac{4\Delta {T_{em}}^*}{3P} \\ &- \frac{\omega_r(k)T_s}{L_d L_q}\Big(\left(L_q - L_d\right)\left(\lambda_{ds}(k)^2 - \lambda_{qs}(k)^2\right) - L_q\lambda_{pm}\lambda_{ds}(k)\Big) \\ &- \frac{R_s T_s \lambda_{qs}(k)}{{L_d}^2{L_q}^2}\Big(\left({L_q}^2 - {L_d}^2\right)\lambda_{ds}(k) - {L_q}^2\lambda_{pm}\Big)\Bigg] \end{aligned} \tag{2.16}$$

$$\lambda_{ds1} = -R_s i_{ds}(k)T_s + \omega_r(k)T_s\lambda_{qs}(k) + \lambda_{ds}(k) \tag{2.17}$$

$$\lambda_{qs1} = -R_s i_{qs}(k)T_s - \omega_r(k)T_s\lambda_{ds}(k) + \lambda_{qs}(k) \tag{2.18}$$

This leads to a quadratic equation in $V_{ds}(k)T_s$ that can be solved as Equation 2.19

$$V_{ds}(k)T_s = \frac{-b \pm \sqrt{b^2 - 4ac}}{2a} \tag{2.19}$$

where

$$a = 1 + M_D{}^2 \tag{2.20}$$

$$b = 2\left(\lambda_{ds1} + M_D\left(B_D + \lambda_{qs1}\right)\right) \tag{2.21}$$

$$c = \lambda_{ds1}{}^2 + \left(B_D + \lambda_{qs1}\right)^2 - \lambda_s^{*2} \tag{2.22}$$

Note that in these equations the only modifiable parameters are $\Delta T_{em}{}^*$ (which only affects B_D, and is present in *b* and *c*) and λ_s^* (which only affects *c*), the rest of the parameters are determined by the estimated machine parameters and the previous operating point. Therefore, the term *a* is fixed.

There are three distinct scenarios for the voltage solution depending on the value inside the square root of Equation 2.19, which can also be interpreted geometrically

1. The value is positive: This leads to two intersecting points, and one of them (the one with lower voltage amplitude) will be chosen as the command voltage
2. The value is null: There is only one intersecting point, which means the differential torque line and the flux circle are tangent.
3. The value is negative: There are no intersecting points, and the solution to Eq. 2.19 is a complex number.

The physical interpretation of the third scenario is that the command flux is too low to attain the desired torque increment, or vice versa, the torque command is too high for the desired machine flux. For this case, a real solution must be found for the real-time implementation of the algorithm. There are two possibilities emerging from the manipulation of the values inside the square root. This is illustrated in Figure 2.9.

1. Solution 1 (torque prioritized): Considering the real part of the complex solution of Eq. 2.19 [10]. This is equivalent to force the value inside the square root to be null by modifying the term *c* while maintaining the term *b* constant. This inherently modifies the command flux λ_s^* and yields a solution on the reference differential torque line, where a flux circle with bigger radius would be tangent.
2. Solution 2 (flux prioritized): Enforce the value inside the square root is null by modifying the term *b* while maintaining the flux command λ_s^* constant. This can

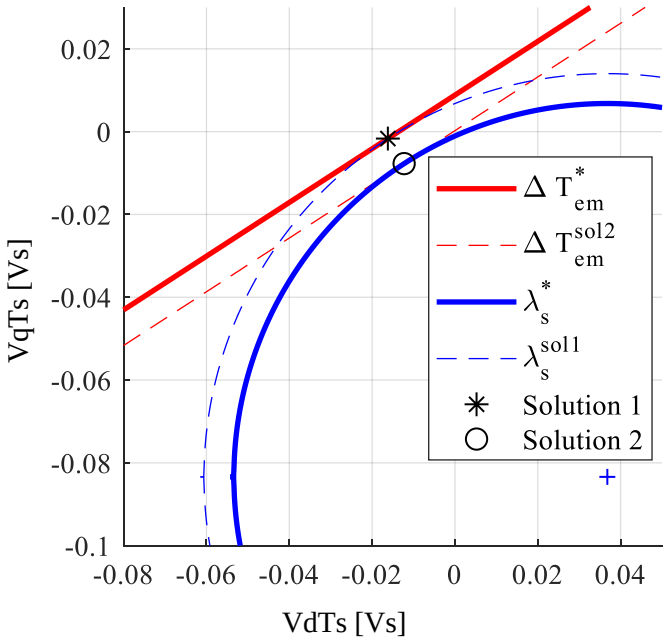

Figure 2.9: Graphical interpretation of the DB-DTFC algorithm for the case of no intersection between flux circle and the differential reference torque line.

only be done by modifying the term B_D, and yields a solution on the reference flux circle, where a torque line with smaller y-intercept (corresponding to a smaller change in torque) would be tangent [17].

At high speeds where the voltage limit dominates the capability of the drive, accurate control of the flux is critical for high performance operation. Therefore, the second solution (Square-Root-Condition or SRC) is chosen. This provides a limitation for B_D according to Equation 2.23

$$b^2 - 4ac \geq 0 \Longrightarrow \left(\left(B_D + \lambda_{qs1}\right) - M_D\lambda_{ds1}\right)^2 \leq \lambda_s^{*2}(1 + {M_D}^2) \tag{2.23}$$

2.2.3. Analytical Evaluation of SRC as a MTPF Strategy

2.2.3.1. Equivalence under Correct Machine Parameters

The SRC method can be shown to be analytically equivalent to MTPF under identical parameters and steady state. The only effect of this assumption in the equations is to remove the term depending on $\Delta {T_{em}}^*$ from the expression of B_D. This means this analysis explores the operating point for which for a given flux circle the maximum change in torque is null (i.e. maximum torque operation). The analysis can be further simplified by assuming a null

stator resistance, but it can be shown that this assumption is not necessary. This analysis is shown explicitly in Appendix A.

The term B_D from the DB-DTFC equations can be expressed as follows for the considered conditions:

$$B_D = \omega_r(k)T_s\left(\lambda_{ds}(k) + M_D\lambda_{qs}(k)\right) + \frac{R_sT_s}{L_dL_q}\left(L_q\lambda_{qs}(k) - M_DL_d\lambda_{ds}(k)\right) \tag{2.24}$$

The SRC from Equation 2.23 can then be rewritten as follows. The *(k)* is removed from this point on for simplicity

$$\left(\lambda_{qs} - M_D\lambda_{ds}\right)^2 \leq \lambda_s^{*2}(1 + {M_D}^2) \tag{2.25}$$

Substituting the term M_D, and rearranging the equation

$$\begin{aligned} 4\left(L_d - L_q\right)^2{\lambda_{ds}}^4 + 4\left(L_d - L_q\right)L_q\lambda_{pm}{\lambda_{ds}}^3 + \left({L_q}^2{\lambda_{pm}}^2 - 4\lambda_s^{*2}\left(L_d - L_q\right)^2\right){\lambda_{ds}}^2 \\ - 2\lambda_s^{*2}\left(L_d - L_q\right)L_q\lambda_{pm}\lambda_{ds} + \lambda_s^{*4}\left(L_d - L_q\right)^2 \geq 0 \end{aligned} \tag{2.26}$$

Identifying the terms in Eq. 2.26 with those of a squared quadratic equation, it can be expressed as

$$2\left(L_d - L_q\right){\lambda_{ds}}^2 + L_q\lambda_{pm}\lambda_{ds} - \lambda_s^{*2}\left(L_d - L_q\right) \geq 0 \tag{2.27}$$

Note that this equation is, on its limit, equal to Eq. 2.8, demonstrating that the SRC inherent to the DB-DTFC algorithm is equivalent to the MTPF strategy under correct machine parameter estimation.

2.2.3.2. Effect of Parameter Estimation Errors

Parameter estimation errors must be considered, as they are an unavoidable circumstance in real applications. Machine parameters may vary due to temperature changes, manufacturing effects and accuracy of the experimental parameter identification process.

To perform an analytical study of the effect of parameter estimation errors it is useful to consider the assumptions of null stator resistance and perfect flux estimation by the flux observers. The operating point calculation from the controller point of view will remain unaffected by the real machine parameters. As proven in the previous subsection, this will lead to the controller attempting to follow the MTPF calculated for the control parameters.

Under the assumption of null stator resistance, the stator voltage produced by the applied voltage can be expressed as

$$\lambda_{ds} = \int \left(V_{ds} T_s - \omega_r \lambda_{qs}(k) \right) dt \tag{2.28}$$

$$\lambda_{qs} = \int \left(V_{qs} T_s + \omega_r \lambda_{ds}(k) \right) dt \tag{2.29}$$

These equations have no dependency on the real machine parameters if the flux estimation is accurate. Hence, the same applied voltage will produce the same flux in the machine. Provided the flux estimation is correct and the voltage drop effect of the stator resistance is negligible, the achieved operating point in terms of dq-flux for maximum torque operation in the second flux weakening region is unaffected by parameter estimation errors.

This means that the SRC works as an online calculation and control of the flux operating point in the MTPF region for the control estimated parameters. This flux will be achieved in the machine as modeled by the Equations 1.3 and 1.4 in which the parameters would be the real ones. Therefore, the changes in machine parameters will modify the operating point produced by the SRC only in terms of the dq-currents as shown by Table 2.1.

Parameter changed	i_{ds}	i_{qs}
λ_{PM}	$\downarrow \lambda_{PM} \Rightarrow \downarrow \lvert i_{ds} \rvert$	Constant
L_d	$\downarrow L_d \Rightarrow \uparrow \lvert i_{ds} \rvert$	Constant
L_q	Constant	$\downarrow L_q \Rightarrow \uparrow i_{qs}$

Table 2.1: Effect of change in real machine parameters on the change in current for a constant dq-flux.

The effect of following the MTPF reference in terms of flux as opposed to doing so in terms of current can be seen in Figure 2.10. The upper plots show the MTPF reference compared to the real MTPF curve when there are parameter estimation errors. It is immediate to observe that the MTPF locus in terms of flux is shows little sensitivity to parameter changes (the lines barely diverge from the control one).

In terms of the dq-current plane, the effect of parameter estimation errors is much larger. In particular, permanent magnet flux and d-axis inductance directly affects the short circuit current, which moves the MTPF curve along the d-axis.

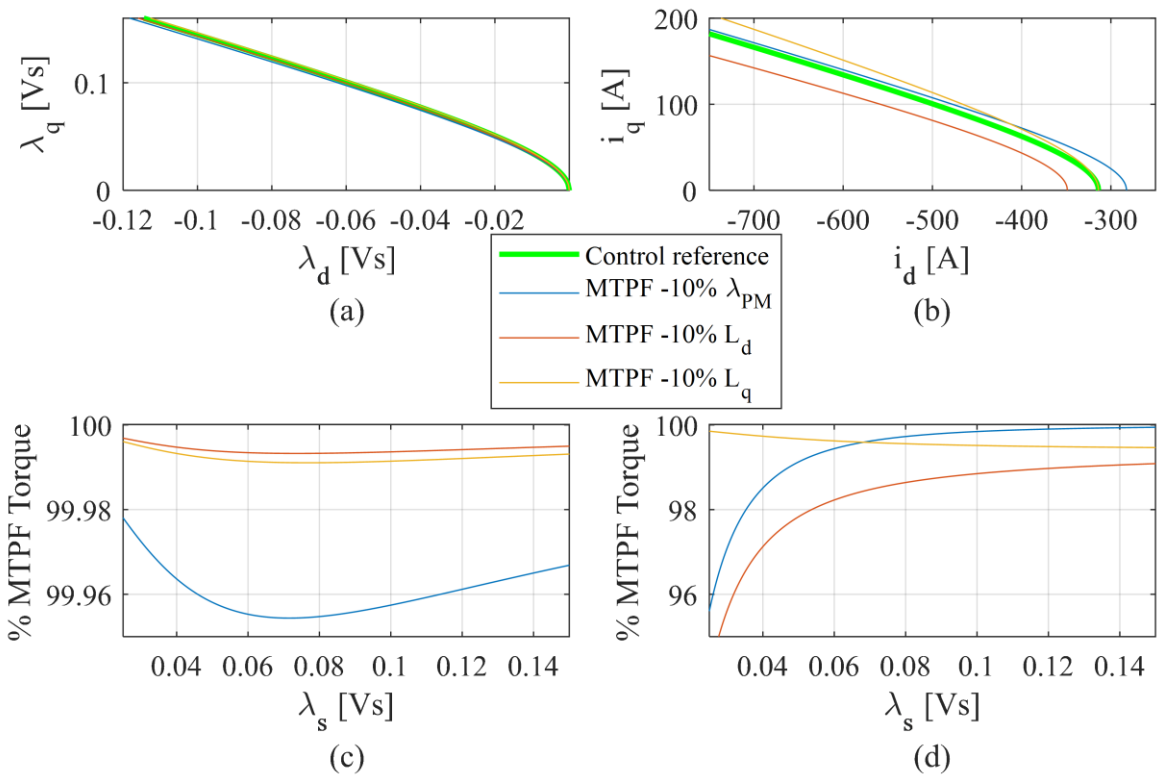

Figure 2.10: Effect of parameter estimation errors in the deviation of the estimated MTPF path from the real one. Comparison in terms of the (a) flux and (b) current path in the synchronous reference frame and (c and d) achieved torque performance.

The lower plots show the comparison, for equal real flux, between the torque achieved by the reference line and the real MTPF torque in each condition. Following a flux reference for MTPF, which is done inherently by the SRC, the error with respect to the maximum torque operation is less than 0.05% and reduces for very high speeds (low flux). On the other hand, following a current reference has torque error much higher, and for errors in d-axis inductance and permanent magnet flux at very high speeds it rapidly increases.

2.2.4. Square Root Condition Implementation

The Square Root Condition can be implemented with very little additional computational effort to the DB-DTFC algorithm. This method does not require the use of any pre-calculated Look-up-table (LUT), and in the case of online parameter estimation, the updated parameters can be used directly. There are no specific ancillary systems required for the implementation other than the limit calculation and the differential torque line saturation, as was seen in Figure 1.8.

The SRC block consists on the Eq. 2.23 expressed as a limit for B_D (Equation 2.30)

$$-\lambda_s^*\sqrt{1+{M_D}^2}+\ M_D\lambda_{ds1}-\lambda_{qs1}\leq B_D\leq\lambda_s^*\sqrt{1+{M_D}^2}+M_D\lambda_{ds1}-\lambda_{qs1} \tag{2.30}$$

The other systems present in the figure are necessary for the implementation of DB-DTFC and were explained in Section 1.3.3.

2.2.5. Simulation Results for SRC

In order to study the behavior of the SRC method, some simulations were performed commanding maximum torque at high speed. The machine parameters were changed from the control ones to observe the effect of estimation errors. The response is studied in terms of the volt-second plane as well as the transient produced in the control variables, the flux in the synchronous rotor reference frame and the dq-current path. No overmodulation was implemented.

In the following studies, darker colors (blue, red) are used for correct parameter estimation and light colors (cyan, magenta) for the scenario introducing parameter estimation errors.

Figure 2.11, Figure 2.14 and Figure 2.17 show the graphical interpretation of the DB-DTFC algorithm for each of the sampling instants during the transient for both perfect estimation (blue, red and black) and parameter estimation errors (cyan, magenta and grey). Since the command torque reference was set to an unachievable value, only the line saturated by the SRC algorithm is shown ($\Delta T_{em\,SRC}$), as well as the command flux circle (λ_s^*). In addition, the geometries corresponding to null change in torque ($\Delta T_{em}=0$) and flux ($\Delta\lambda_s=0$) are shown in discontinuous lines. These geometries are further explained in Section 4.3.3.

The hexagonal and linear voltage limits can be seen for each of the time instants, although in this test the linear limit was used. One of the vertexes of the hexagon is marked with a circle to track its rotation. Lastly, the unsaturated (intersect) and saturated voltage set points calculated by the algorithm and sent to the inverter are displayed. The first time instant is chosen one sampling period before applying the maximum torque command. All subsequent instants show one sampling period increment with respect to the previous one, except the last which is chosen to show the final steady state.

To better interpret these results, the evolution against time of the DB-DTFC parameters and the response in torque and flux is shown in Figure 2.12, Figure 2.15 and Figure 2.18. As

before, red and blue lines correspond to the simulation with perfect estimation while cyan and magenta lines show the effect of changing the machine parameters. In these figures, the markers (x) show the time instants corresponding to each subfigures in Figure 2.11, Figure 2.14 and Figure 2.17 respectively. The sub-figures show the following variables:

(a) Slope of the differential torque line
(b) q-axis intercept of the differential torque line. The value corresponding to the command line saturated by the SRC is shown in a solid line, and the one for the null change in torque line is shown in a discontinuous line.
(c) Electromagnetic torque (solid line). The maximum torque (MTPF) at the final flux is shown in a discontinuous line for comparison.
(d) Decoupling of d-axis flux. In the DB-DTFC algorithm geometry, it is the additive inverse of the d-coordinate of the center of the flux-circle.
(e) Decoupling of q-axis flux. In the DB-DTFC algorithm geometry, it is the additive inverse of the q-coordinate of the center of the flux-circle.
(f) Total stator flux.

. Finally, Figure 2.13, Figure 2.16 and Figure 2.19 show the transient in the d and q-axis flux ((a) and (b) respectively), as well as the current path in the dq-reference frame (c).

2.2.5.1. Changes in Permanent Magnet Flux

For a detuning of the permanent magnet flux, the dq-flux transient is virtually unaffected, and so the operation in terms of the DB-DTFC variables shows no differences between the two scenarios.

Once the torque step is applied (t = 0.1s, Figure 2.11 (b)), the command torque line is saturated by the SRC. From this point on, it will be tangent to the command flux circle. The null change in torque line remains in the same location, as the flux in the machine has not change yet. The same applies for the null change in flux circle. However, the applied voltage is no longer in the intersection between these two geometries. The new intersection is on top of the flux circle, and the voltage set point is calculated with the same phase but limited amplitude to respect the inverter constraints. This results in the set point for t = 0.1s being inside the null change in flux circle and below the null change in torque line. Therefore, it is

expected that for the next time step both these variables will be reduced. This is the case, as can be appreciated in Figure 2.12 (c) and (f).

For all subsequent time instants, the voltage set point remains above the null change in torque line, and so the torque is always increasing. This does not happen with respect to the null change in flux circle until t = 1.003 (Figure 2.11 (e)). It is important to note that the command differential torque line saturated by the SRC and the null change in torque line merge together when the steady state is reached (Figure 2.11 (o), Figure 2.12 (b)). In other words, the final operating point produced by the SRC method is such that the highest allowable change in torque for a certain flux is null (i.e. the controller is operating at the MTPF).

The movement of the intersection point is produced by the evolution of the flux circle (Figure 2.11, Figure 2.12 (d) and (e)) and the change in the differential torque line slope (Figure 2.12 (a)). The algorithm inherently evolves in a direction that allows the tangent point to end within the voltage limit provided the command flux is low enough.

As predicted in Section 2.2.3.2 Table 2.1, the current path and final steady state operating point in terms of dq-current changes (Figure 2.13 (c)), despite the dq-flux being unaffected by the changes in real permanent magnet flux. For a reduction in λ_{PM} the final q-axis current is unmodified while the d-axis current is decreased in amplitude.

Finally, the steady state torque in Figure 2.12 (c) is shown to be very close to the MTPF in both scenarios. For correct parameter estimation, the operation oscillates with decreasing amplitude around the correct point, while for the detuned case it does so around a torque 0.05 Nm lower than the maximum. This represents a torque performance of 99.96%, which is consistent with the study shown in Figure 2.10.

2.2.5.2. Changes in d-axis Inductance

The general response of the system is equivalent to that explained in the previous subsection. In Figure 2.14 (a), before the torque command, the control maintains a similar but not exactly equal operating point. This can also be appreciated in Figure 2.15 and Figure 2.16 (a), (b), in which both lines oscillate around the same operating point, but are not exactly equal. This is consistent with the analysis in previous sections, as the only points expected to be unaffected by machine parameters are steady states dominated by the SRC saturation.

The detuning of the d-axis inductance modifies the flux transient, and so the evolution is slightly different for the case with parameter estimation errors. The geometries for null change in torque and flux are also different, despite being calculated with correct machine parameters, due to the differences in flux during the transient. The detuned controller has a delay with respect to the case of correct parameter estimation (Figure 2.15 (b), (d), (e), (f), Figure 2.16 (a), (b)).

Despite showing differences in the transient, the final operating point in terms of flux is unaffected by the real machine parameters (Figure 2.14 (o), Figure 2.16 (a), (b)), and the same voltage set point will be chosen in steady state. However, the current path and final steady state point in terms of dq-current is changed (Figure 2.16 (c)). In addition, as predicted in Table 2.1, for a reduction in L_{ds} the final q-axis current is unmodified while the d-axis current is increased in amplitude.

As before, the steady state torque in Figure 2.15 (c) appears to approach the MTPF in both scenarios. This is the case for correct parameter estimation, while the detuned case settles around a toque 0.01 Nm lower than the maximum. This represents a torque performance of 99.99%, as expected by the study in Figure 2.10. It is important to note that the final torque for lower d-axis inductance in the machine is higher because the machine has higher capabilities under these conditions, but the relative performance with respect to the MTPF is higher for correct parameter estimation.

2.2.5.1. Changes in q-axis Inductance

The detuning of the q-axis inductance has a less significant effect in the flux transient than the previous case, and a significant delay is not appreciated (Figure 2.19 (a), (b)).

As expected, the final operating point in terms of dq-flux and in the volt-second plane (Figure 2.19 (a), (b), Figure 2.17 (o)) is unaffected by the change in real machine parameters. The reduction of L_{qs} modifies the final dq-current operating point as predicted by Table 2.1, maintaining the d-axis current constant while in the q-axis it is increased (Figure 2.19 (c)).

The MTPF torque is less sensitive to changes in q-axis inductance (Figure 2.18 (c)) than in the other studied parameters. The final torque compared to the MTPF point is analogous to the previous cases, with a 99.99% of the maximum torque in the detuned operation.

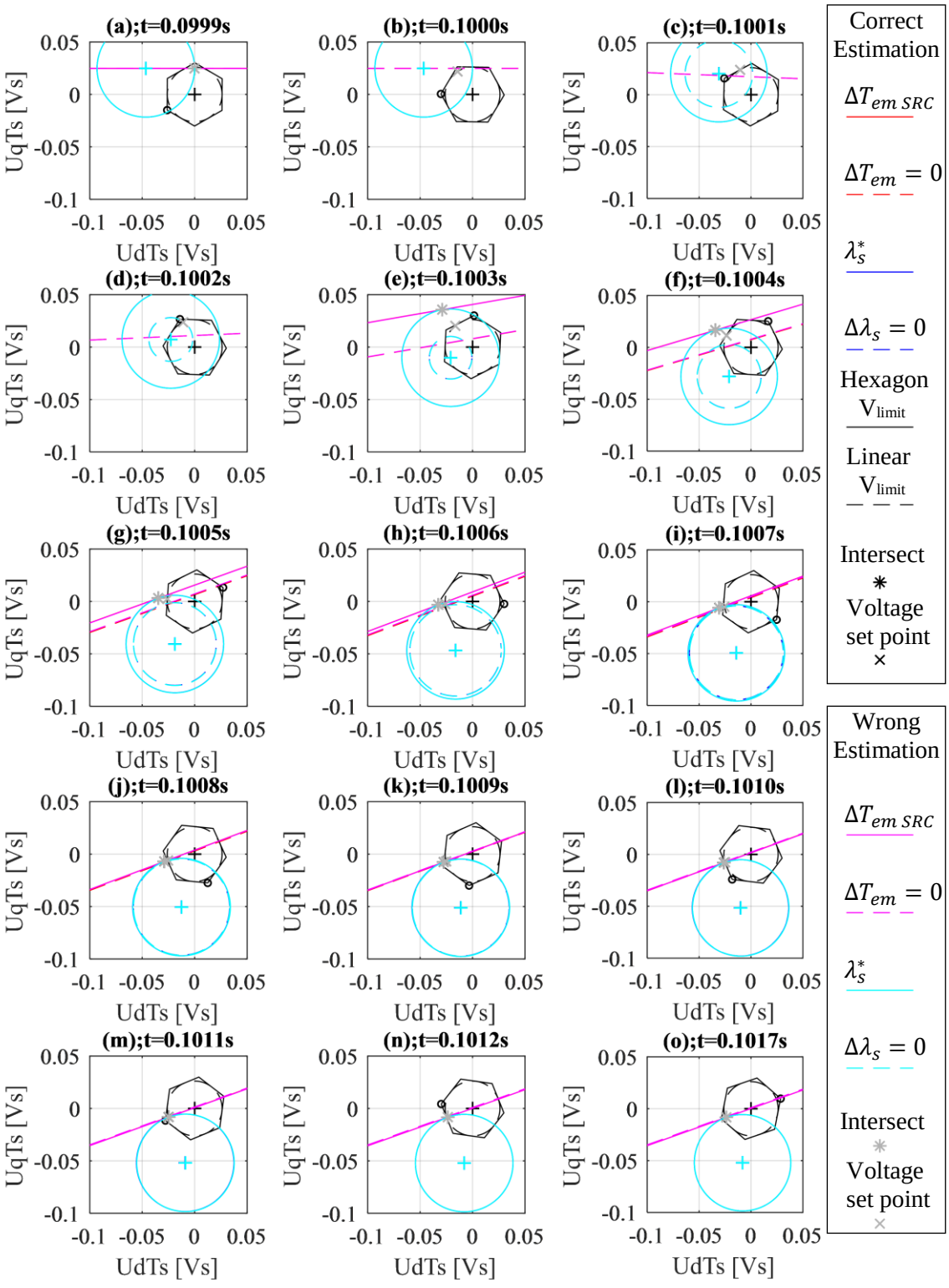

Figure 2.11: DB-DTFC algorithm graphic interpretation in the synchronous reference frame volt-second plane. Transient in the second flux weakening region from null to maximum torque. Shown for correct parameter estimation (blue and red) and detuning of λ_{pm} of -10% (cyan and magenta).

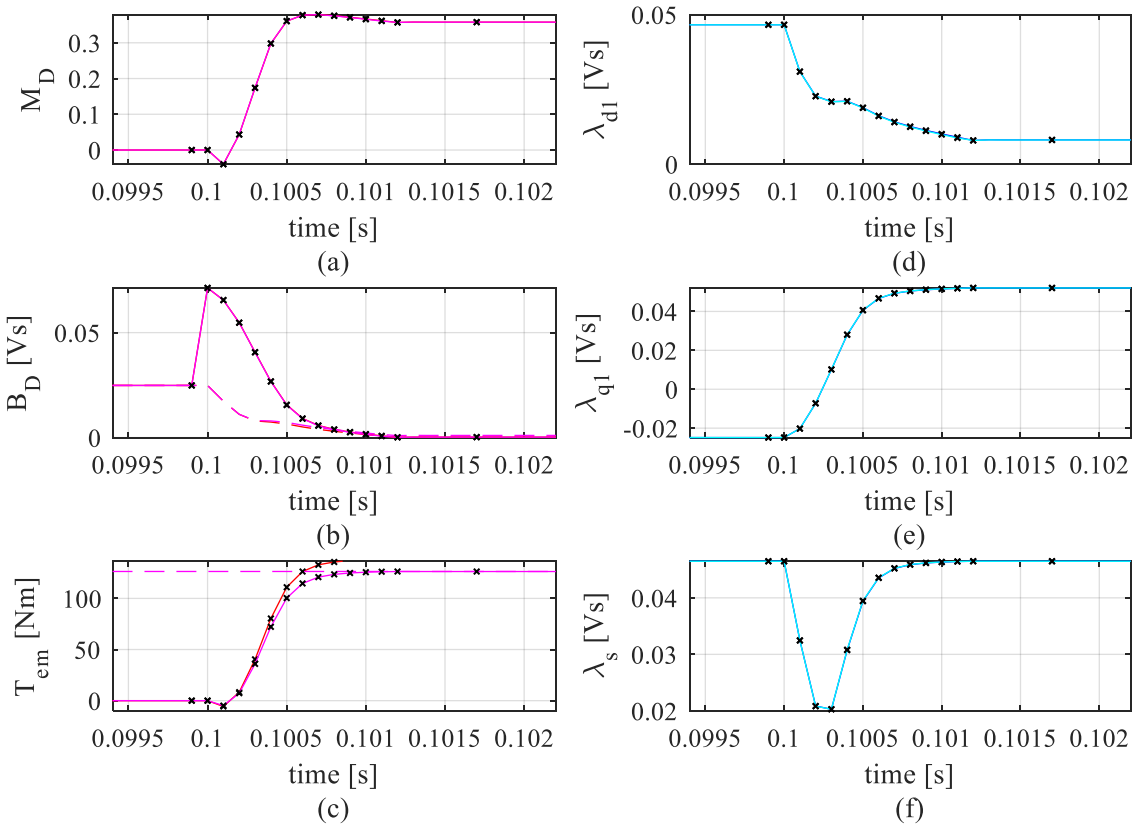

Figure 2.12: Transients in the DB-DTFC variables and response in torque and flux for a step torque command from null to maximum at t = 0.1s in the secon flux weakening region. Shown for correct parameter estimation (blue and red) and detuning of λ_{pm} of -10% (cyan and magenta).

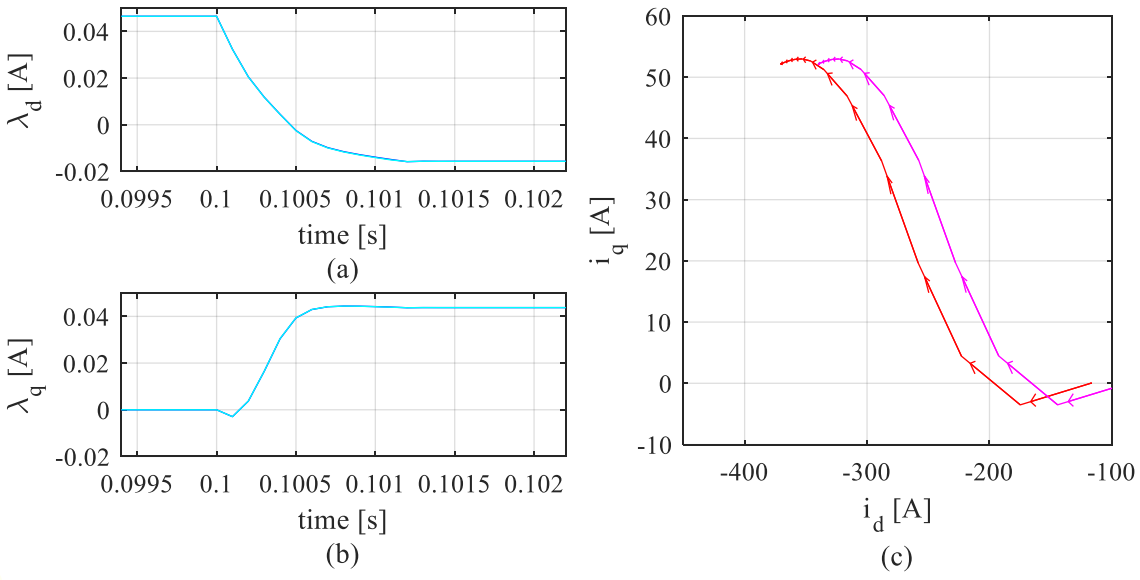

Figure 2.13: Transients in dq-flux ((a) and (b)) and current path (c) for a step torque command from null to maximum at t = 0.1s in the secon flux weakening region. Shown for correct parameter estimation (blue and red) and detuning of λ_{pm} of -10% (cyan and magenta).

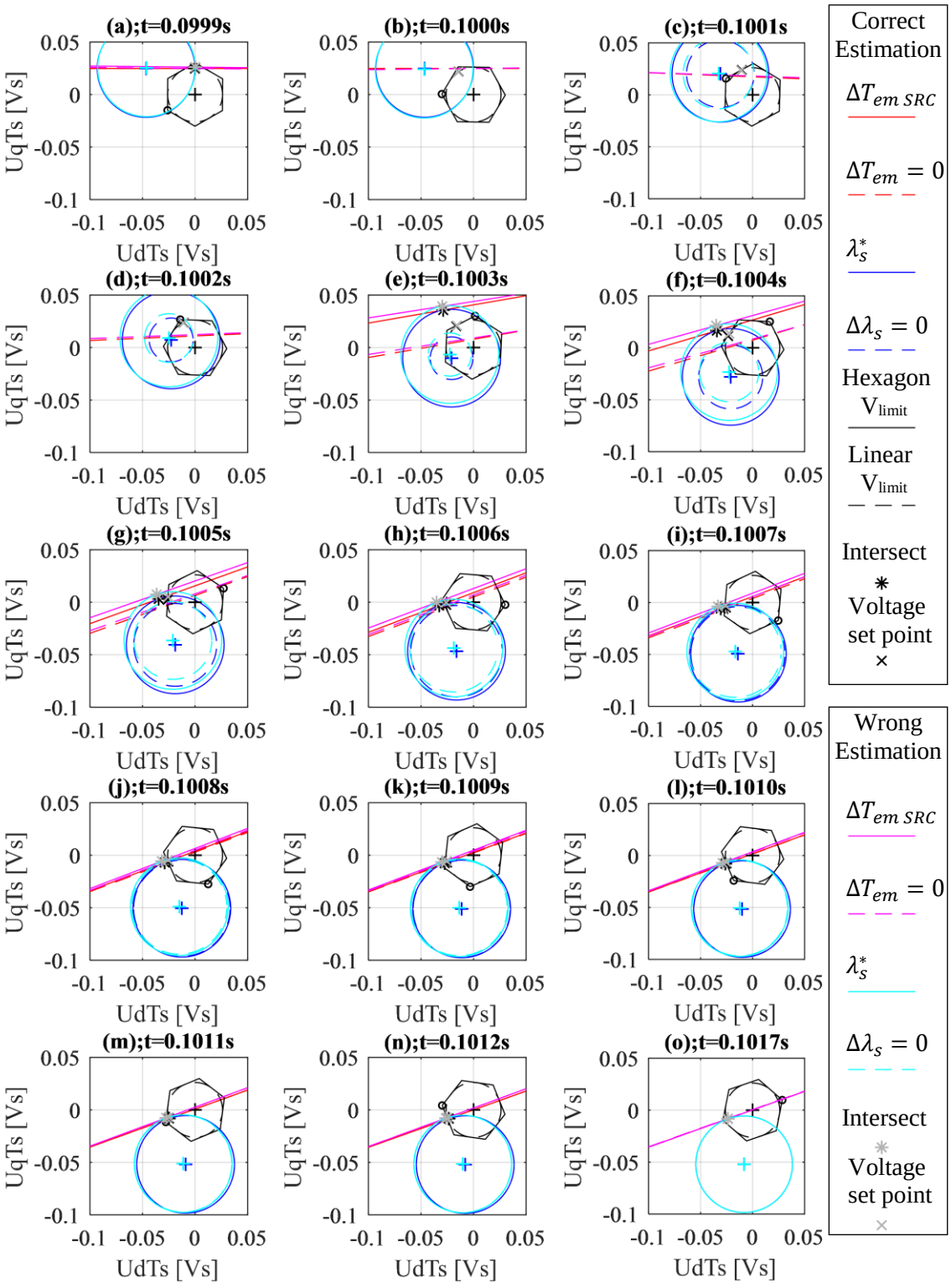

Figure 2.14: DB-DTFC algorithm graphic interpretation in the synchronous reference frame volt-second plane. Transient in the second flux weakening region from null to maximum torque. Shown for correct parameter estimation (blue and red) and detuning of L_d of -10% (cyan and magenta).

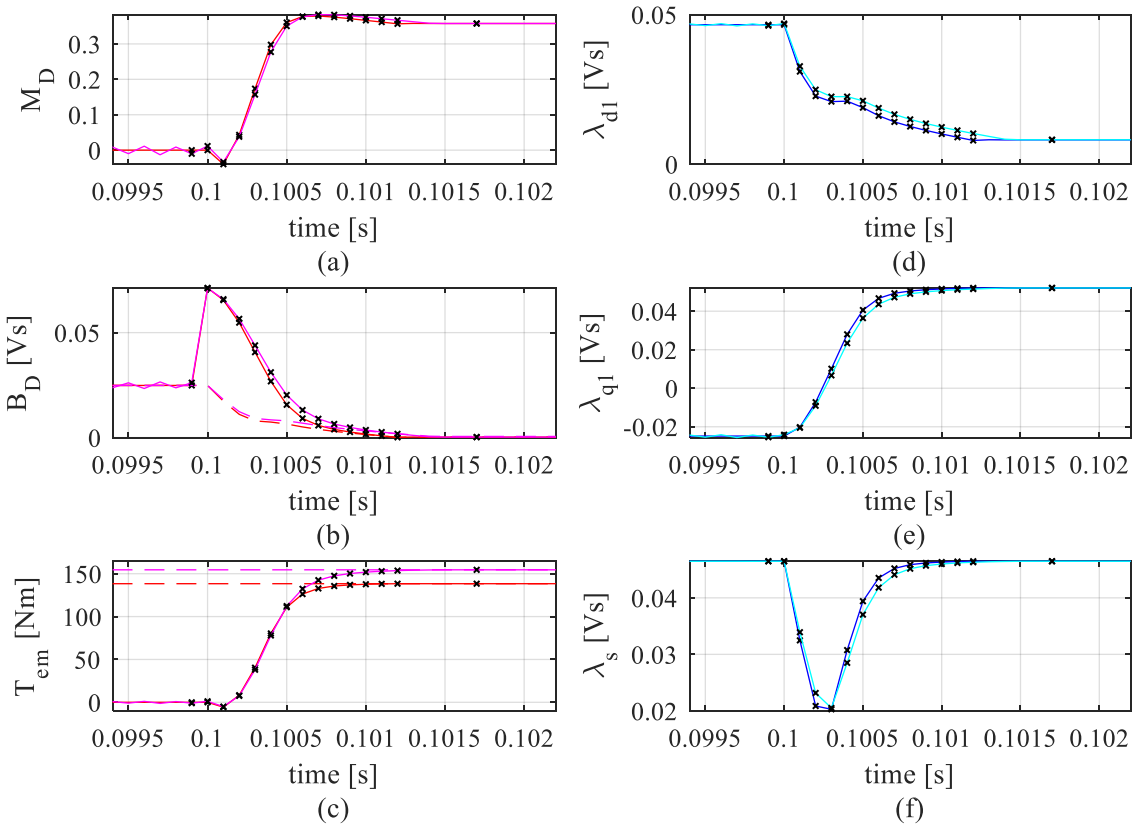

Figure 2.15: Transients in the DB-DTFC variables and response in torque and flux for a step torque command from null to maximum at t = 0.1s in the secon flux weakening region. Shown for correct parameter estimation (blue and red) and detuning of L_d of -10% (cyan and magenta).

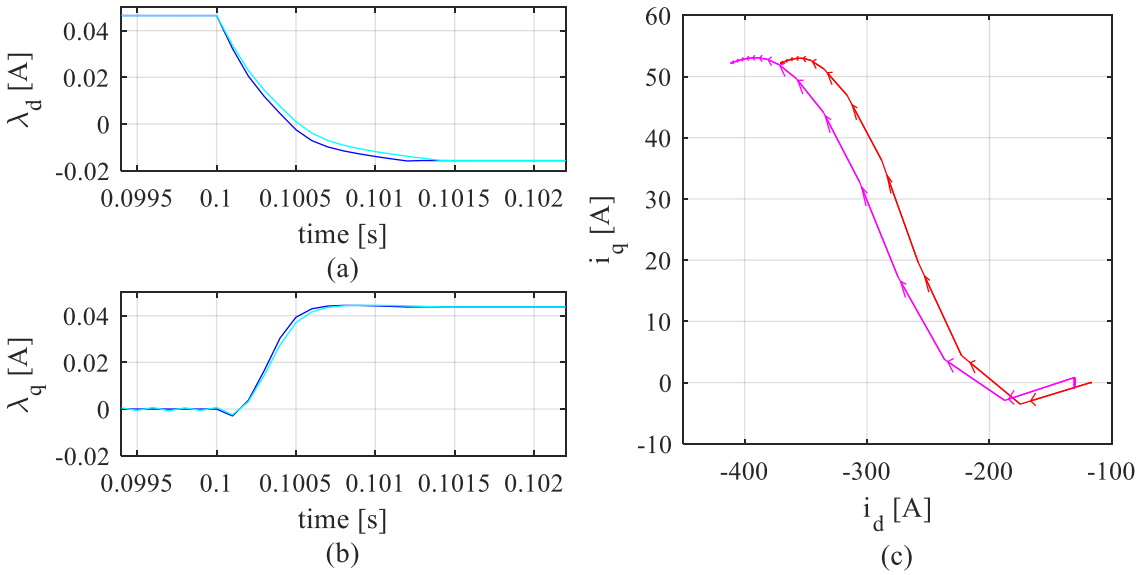

Figure 2.16: Transients in dq-flux ((a) and (b)) and current path (c) for a step torque command from null to maximum at t = 0.1s in the secon flux weakening region. Shown for correct parameter estimation (blue and red) and detuning of L_d of -10% (cyan and magenta).

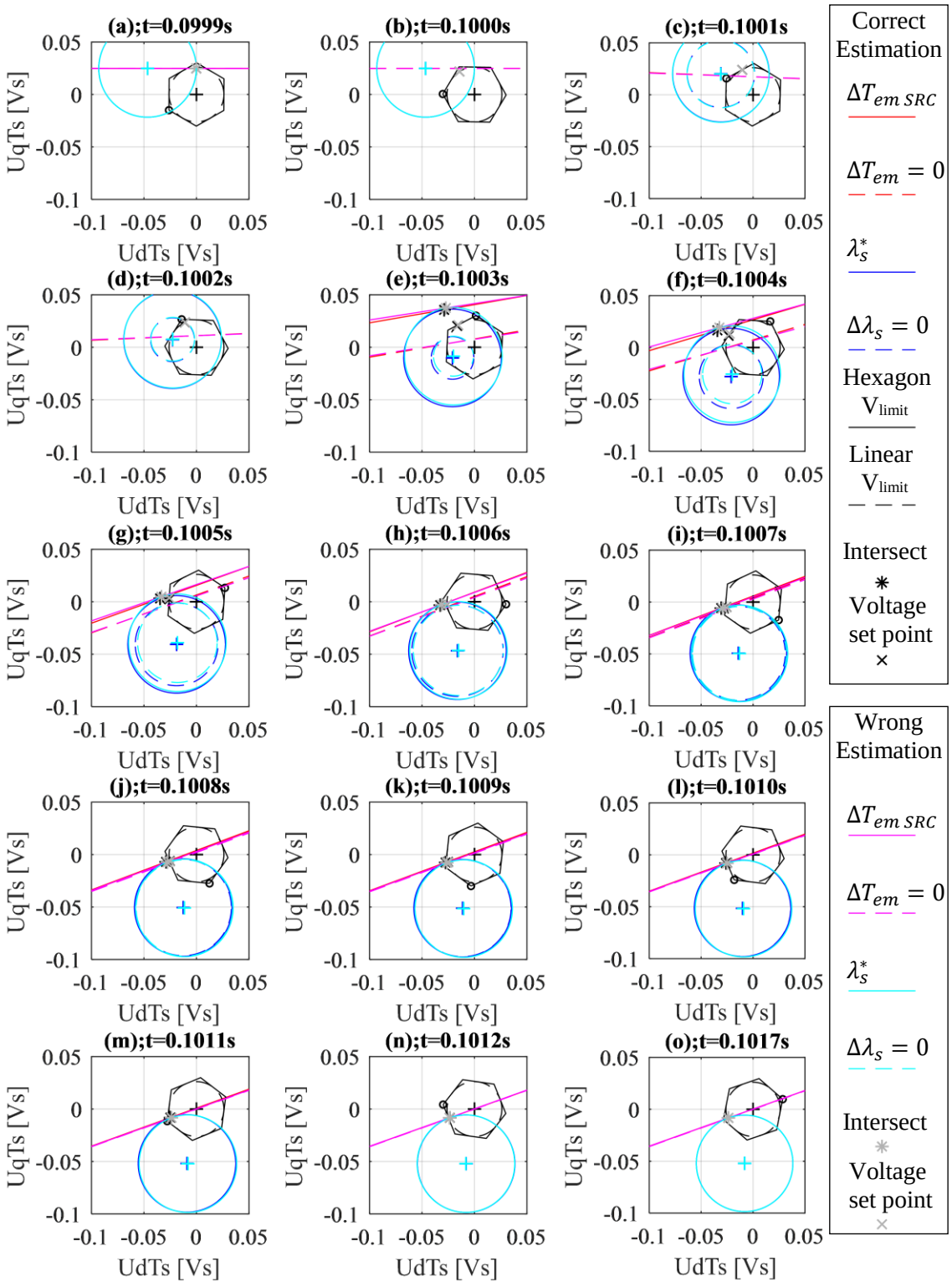

Figure 2.17: DB-DTFC algorithm graphic interpretation in the synchronous reference frame volt-second plane. Transient in the second flux weakening region from null to maximum torque. Shown for correct parameter estimation (blue and red) and detuning of L_q of -10% (cyan and magenta).

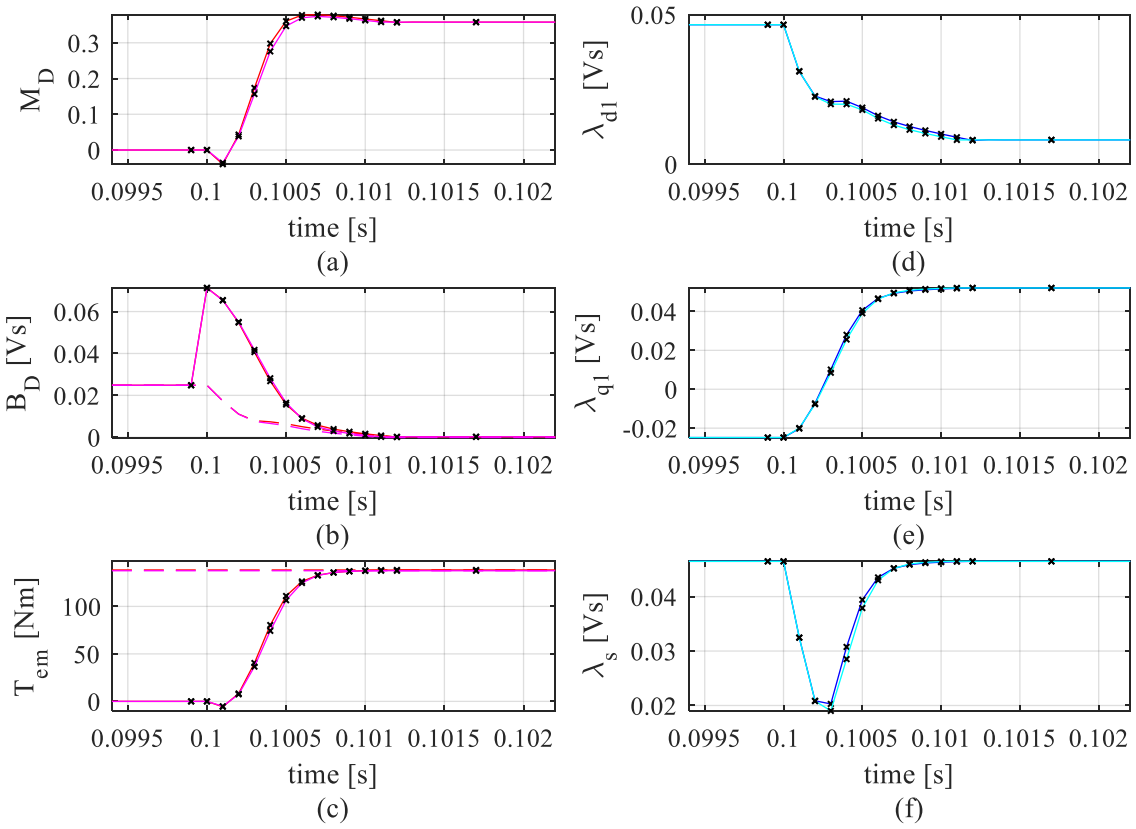

Figure 2.18: Transients in the DB-DTFC variables and response in torque and flux for a step torque command from null to maximum at t = 0.1s in the secon flux weakening region. Shown for correct parameter estimation (blue and red) and detuning of L_q of -10% (cyan and magenta).

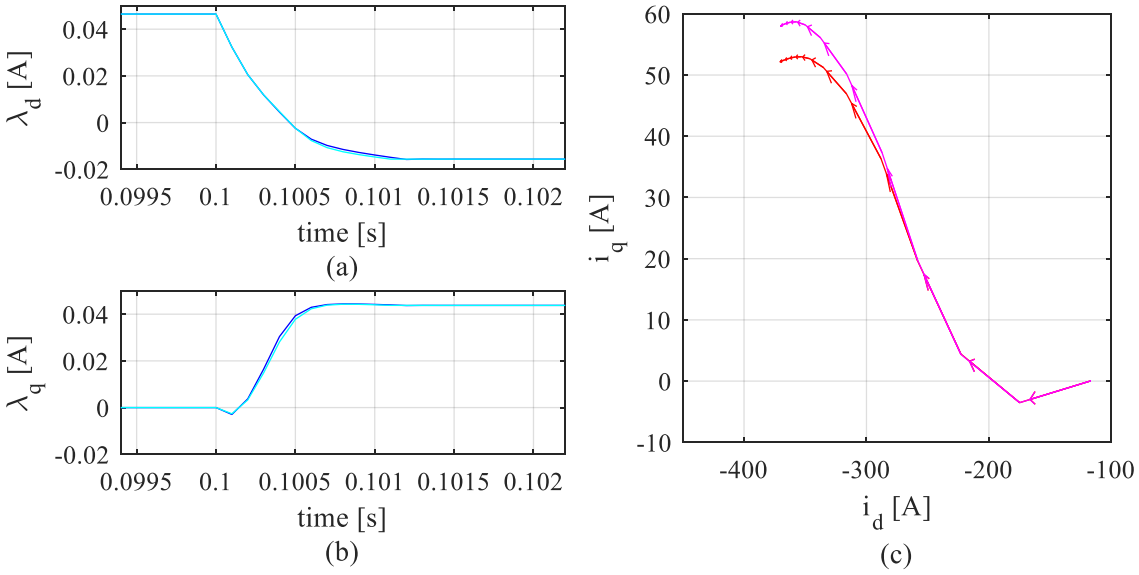

Figure 2.19: Transients in dq-flux ((a) and (b)) and current path (c) for a step torque command from null to maximum at t = 0.1s in the secon flux weakening region. Shown for correct parameter estimation (blue and red) and detuning of L_q of -10% (cyan and magenta).

2.2.6. Comparison of MTPF Operation of SRC with CVC Methods

2.2.6.1. MTPF for Current Vector Control

For comparison purposes, the operation of CVC at the maximum power is studied (the strategies for partial load operation at high speeds are not considered). Maximum torque can be attempted by CVC in the constant torque region by an MTPA strategy as seen in Section 1.2.2. When the base speed is reached, the d-axis current must be modified to stay within the voltage limit, and the q-axis current is reduced to stay at the current limit.

For maximum performance in the second flux-weakening region, the current must follow the MTPF path. This is problematic due to the risks of employing a completely feedforward technique to operate close to the voltage limit. If the flux produced is too high for the inverter limit, the torque will drop suddenly, and there could be instability problems and changes to generation mode. For this reason, hybrid flux weakening structures are preferred.

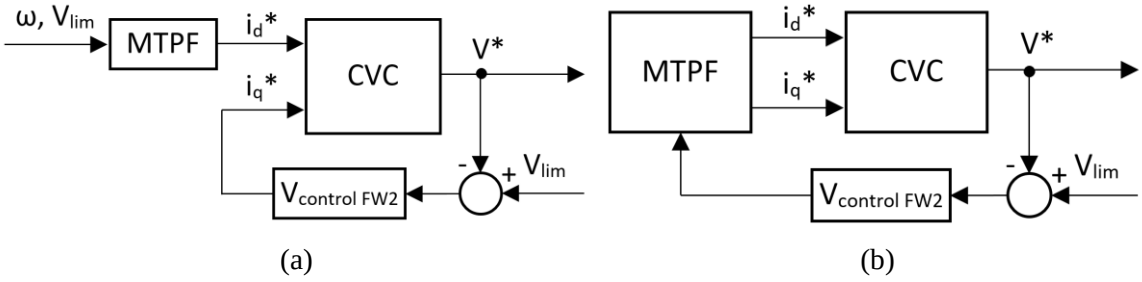

Figure 2.20: CVC hybrid flux weakening methods to attempt operation following the MTPF line in the second flux weakening region

Two options are studied to attempt this operation as illustrated in Figure 2.20. The first option (a) generates a reference for the d-axis current based on the stored MTPF curve. The q-axis current is then used to keep the operation at the voltage limit. Alternatively, the second option (b) follows the stored MTPF curve with both currents, but accesses this curve through a closed loop control that ensures the voltage limit is kept. In this case and when there are parameter estimation errors, the flux for which the stored currents were calculated to produce maximum torque is different than the one at which they are applied. Both options can maintain the operation safely at the maximum flux possible for a certain speed considering the voltage limit**.**

To evaluate the effect of errors in the different methods, several simulations were performed studying the final operating point when the machine parameters differed from the

control ones. Additionally, the real MTPF line is shown for comparison purposes. For the CVC methods, null steady state error is assumed (i.e. the comparison is done with respect to the references generated by the systems in Figure 2.20).

2.2.6.2. Effect of Parameter Estimation Errors

The following studies (Figure 2.21, Figure 2.23 and Figure 2.24) show:

- A zoomed-out view (a) of the current plane with the real MTPF curve and flux ellipses. Green is used for the case of accurate parameter estimation, blue for a parameter reduction of 10% and red for a parameter increase of 10%. Additionally, the curve that the method CVC_a (Figure 2.20) would follow is shown in cyan for a parameter reduction of 10% and in magenta for a parameter increase of 10%. Method CVC_b will always follow the control MTPF curve (thick green line), but the point in that curve will change to operate at the same flux when machine parameters change. The operating point shown for SRC is the steady state achieved in simulation for the maximum torque command.
- A zoomed-in view (b and c) of the operating points for making a clear comparison between the different algorithms. The legend indicates the torque achieved and current used by each of them. The markers are also shown in figure (a).

All the operating points compared operate at the same flux i.e. for each scenario they will all lie in the same flux ellipse. This flux ellipse will change due to the variation of real machine parameters, but the total value of the flux is kept constant.

2.2.6.2.1. Changes in Permanent Magnet Flux

The biggest effect of the permanent magnet flux in the MTPF line is in terms of displacement due to the short circuit current. When the parameters are correctly estimated, all methods achieve the same operating point, which coincides with the real MTPF operation.

In Figure 2.21 (a) it can be appreciated that the locus of references for the method CVC_a typically diverges from the original MTPF line in the opposite direction to the movement of the actual MTPF line. The exception to this happens for an increase in permanent magnet flux (magenta line) at high speeds. There is a point in which this line intersects the original MTPF line (which is also the locus of the references for the CVC_b method). For all points

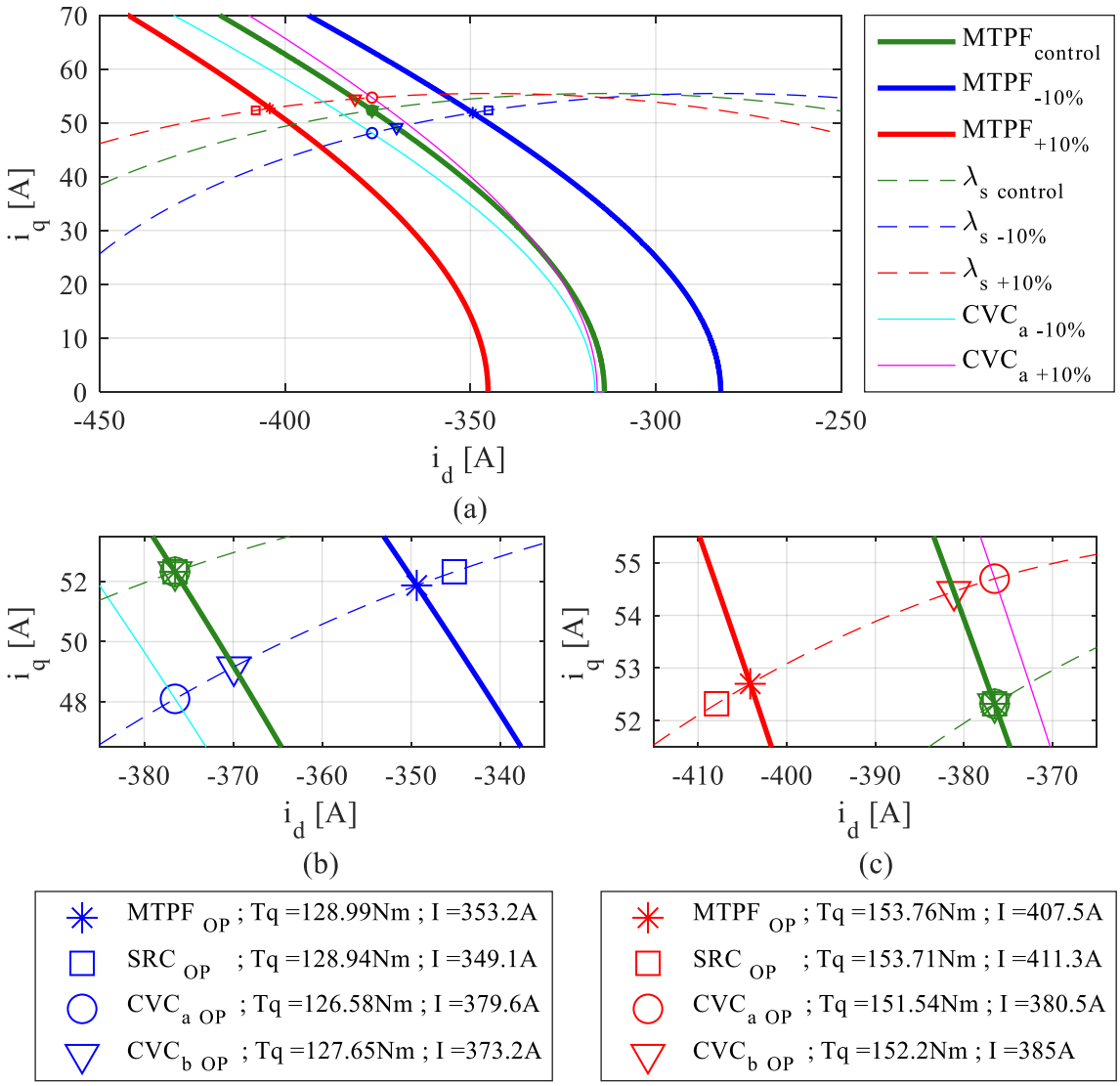

Figure 2.21: MPTF simulation scenarios for changes in λ_{pm} in the dq-current plane. Operating points, torque and current for the real MTPF point, SRC method and hybrid flux weakening strategies for CVC.

above this flux, since the CVC_b method is closer to the real MTPF line it will produce higher torque.

This is observed as well in the two examples shown. The SRC method is the closest to the real MTPF point, and produces the highest torque. For a reduction in permanent magnet flux (Figure 2.21 (b)) the torque reduction is also combined with a reduction in total current.

The CVC methods show a higher reduction in torque than the SRC, with method CVC_b being more advantageous in both scenarios shown. It is important to note that the relation between the distance to the optimum MTPF point and the reduction in torque is not linear

and worsens with distance. The distance between the two CVC methods is similar to the distance between MTPF and SRC in Figure 2.21 (c), but the former has a torque difference of 0.56 Nm while in the latter this difference is 0.05 Nm.

The scenarios for changes in permanent magnet flux are useful to gain insight into the behavior of the different methods studied, as shown in Figure 2.22. The SRC method for this case evolves as indicated in Table 2.1, the q-axis current is kept constant, and the d-axis current amplitude changes in the same direction as the permanent magnet flux. This will change for variations in other parameters.

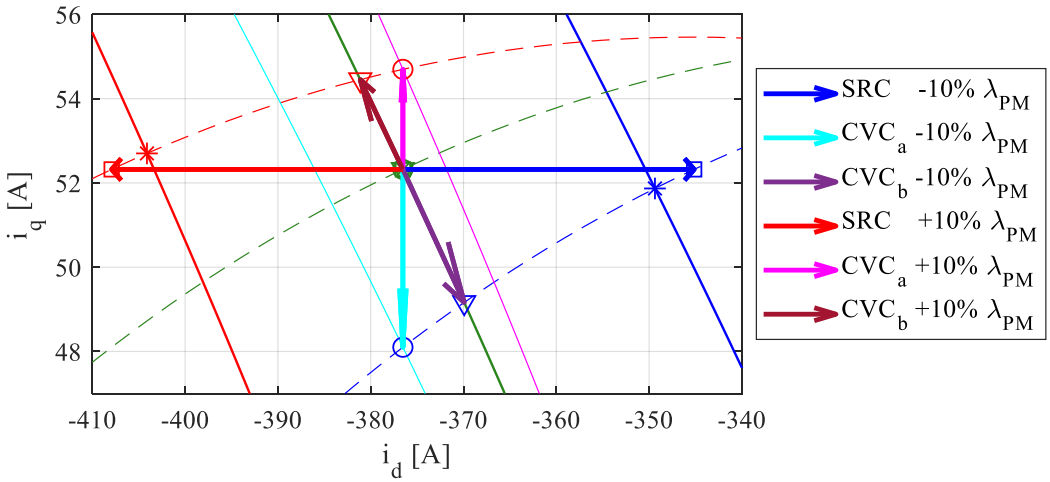

Figure 2.22: Evolution of the operating point for SRC and CVC hybrid flux weakning strategies for operation at maximum torque in the second flux weakening region for changes in λ_{pm}.

The method CVC_a always maintains the d-axis current constant and equal to the value that it would have in the original MTPF line for that value of flux (pre-calculated LUT). The q-axis current is then modified until it meets the real flux (or voltage) ellipse.

The method CVC_b is always operating in the original MTPF line and the location in that reference is not linked to the originally calculated flux as in CVC_a, but changes dynamically according to the voltage controller.

2.2.6.2.2. Changes in d-axis Inductance

The effect of d-axis inductance on the real MTPF line (Figure 2.23) is similar to that of the permanent magnet flux, but in the opposite direction. In this way, similar arguments can be made for the CVC_a method being consistently worse than the CVC_b method for most values of flux, except in this case for low flux with a reduction of d-axis inductance.

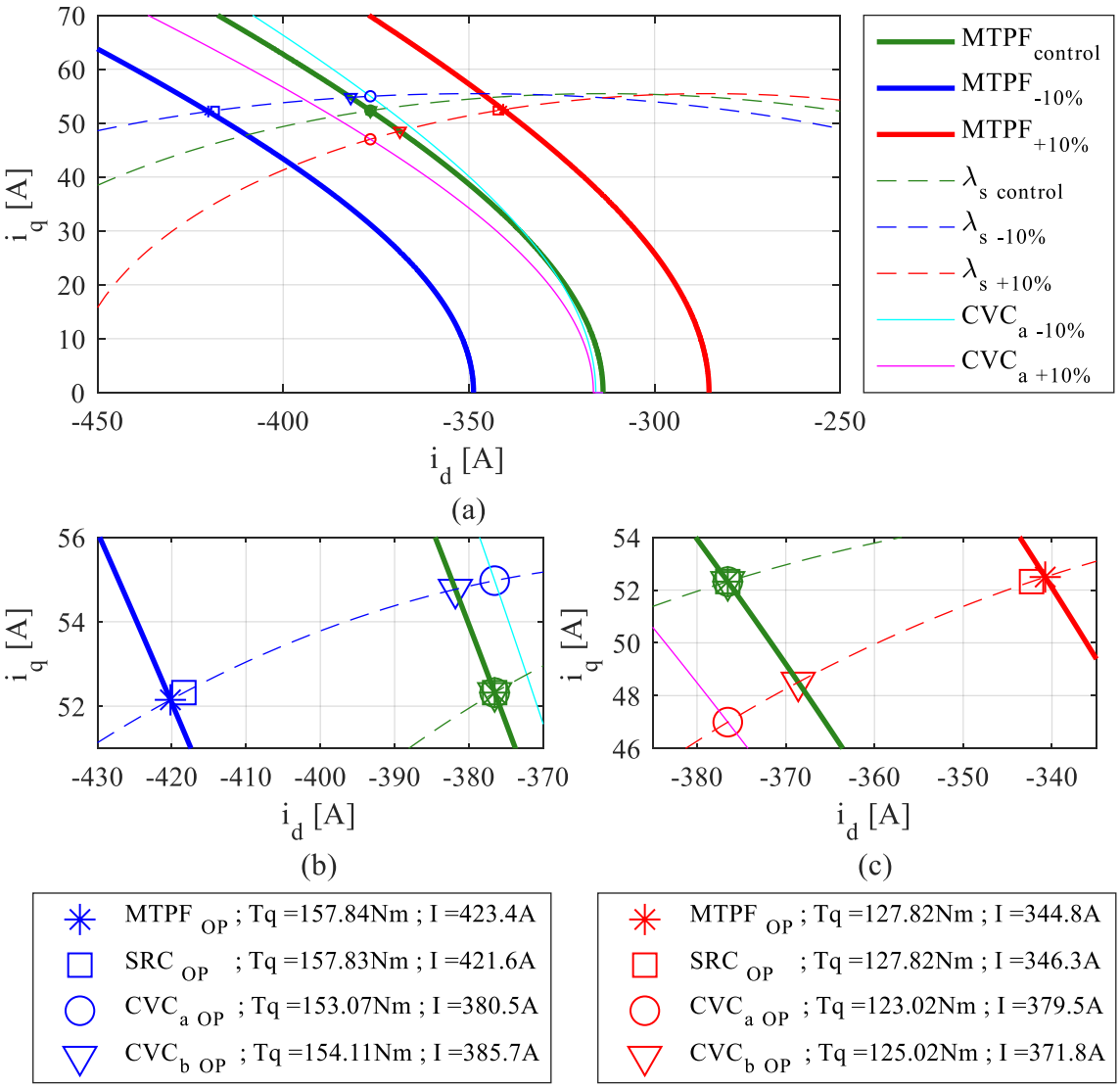

Figure 2.23: MPTF simulation scenarios for changes in L_d in the dq-current plane. Operating points, torque and current for the real MTPF point, SRC method and hybrid flux weakening strategies for CVC.

SRC shows superior performance for both scenarios, with a torque reduction of 0.006% in the case of parameter increase. On the other hand, the CVC methods show even more parameter sensitivity than the previous case.

2.2.6.2.3. Changes in q-axis Inductance

The change in q-axis inductance modifies the slope of the real MTPF line (Figure 2.24). For this case, SRC and CVC_a produce the same operating point, since both maintain the d-axis current constant.

In this case, the method CVC_b is worse than CVC_a for all operating points. The sensitivity

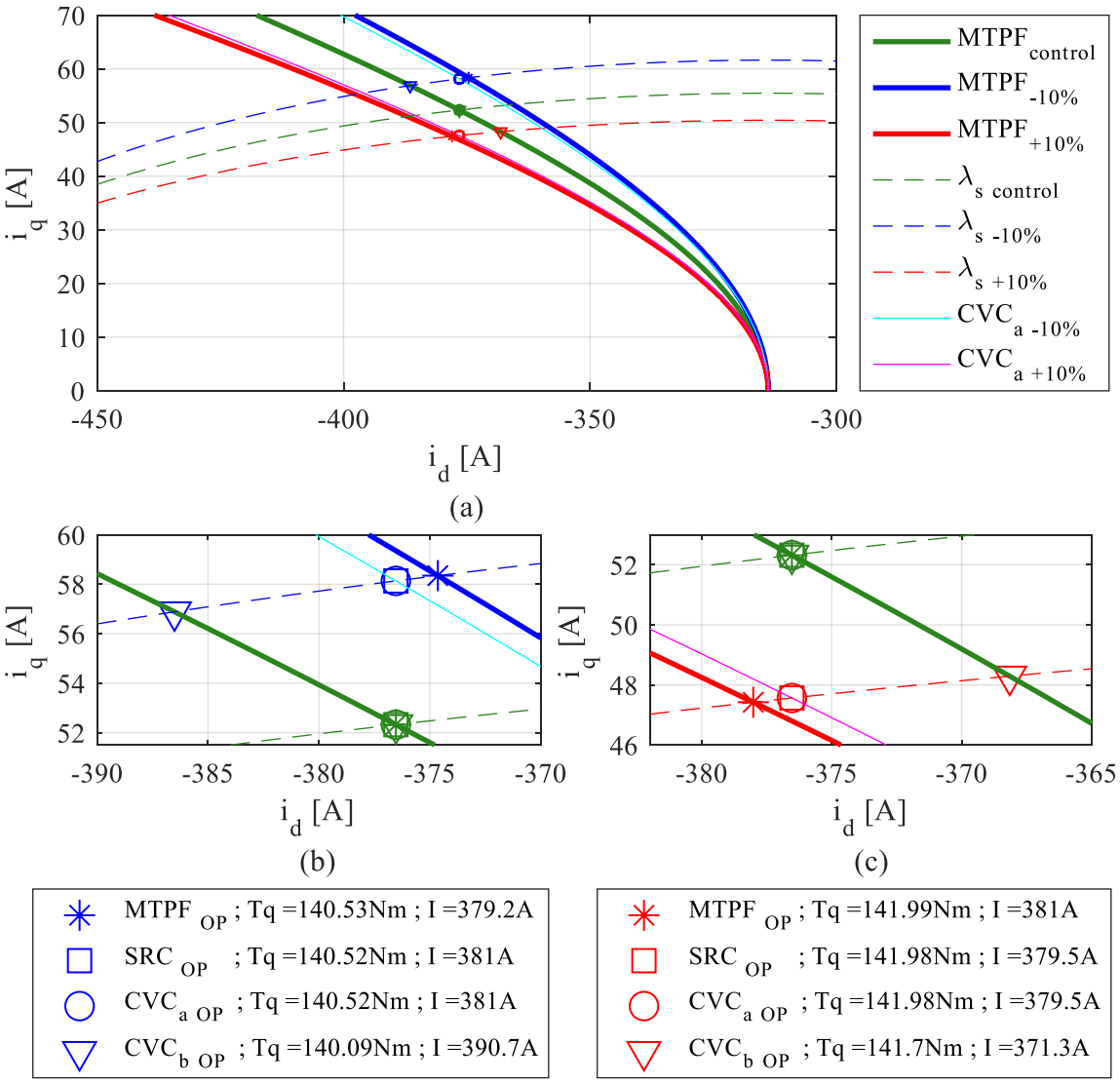

Figure 2.24: MPTF simulation scenarios for changes in L_q in the dq-current plane. Operating points, torque and current for the real MTPF point, SRC method and hybrid flux weakening strategies for CVC.

of all methods is lower for changes in q-axis inductance than to the other parameters studied, as can be observed by the difference in torque.

2.2.6.3. Performance Comparison

To evaluate the performance of the proposed methods in a more general way, several simulations were performed extracting data points analogous to the previous subsections. Two different speeds were evaluated, and parameter changes every 2.5% variation were applied. The results are displayed in Figure 2.25. A detailed view of this figure for the results of the SRC method can be seen in Figure 2.26.

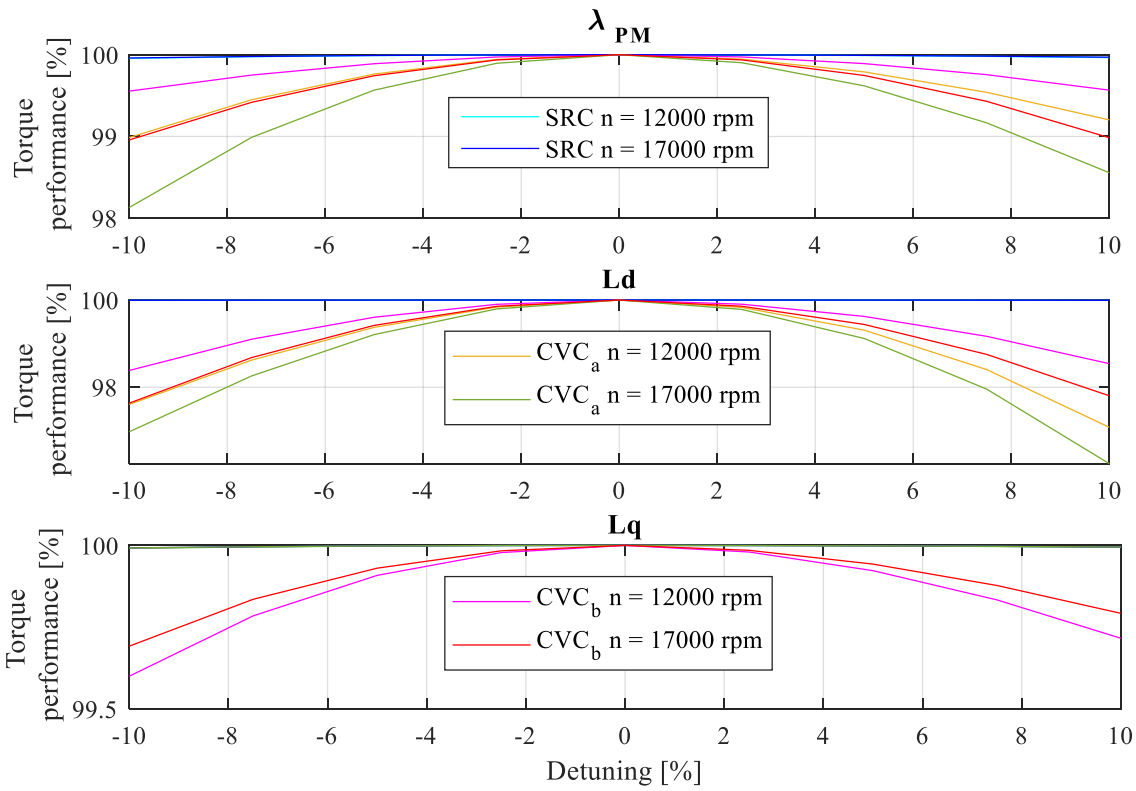

Figure 2.25: Effect of parameter estimation errors and speed on the relative torque performance with respect to the MTPF operation of the SRC method and CVC hybrid flux weakening methods.

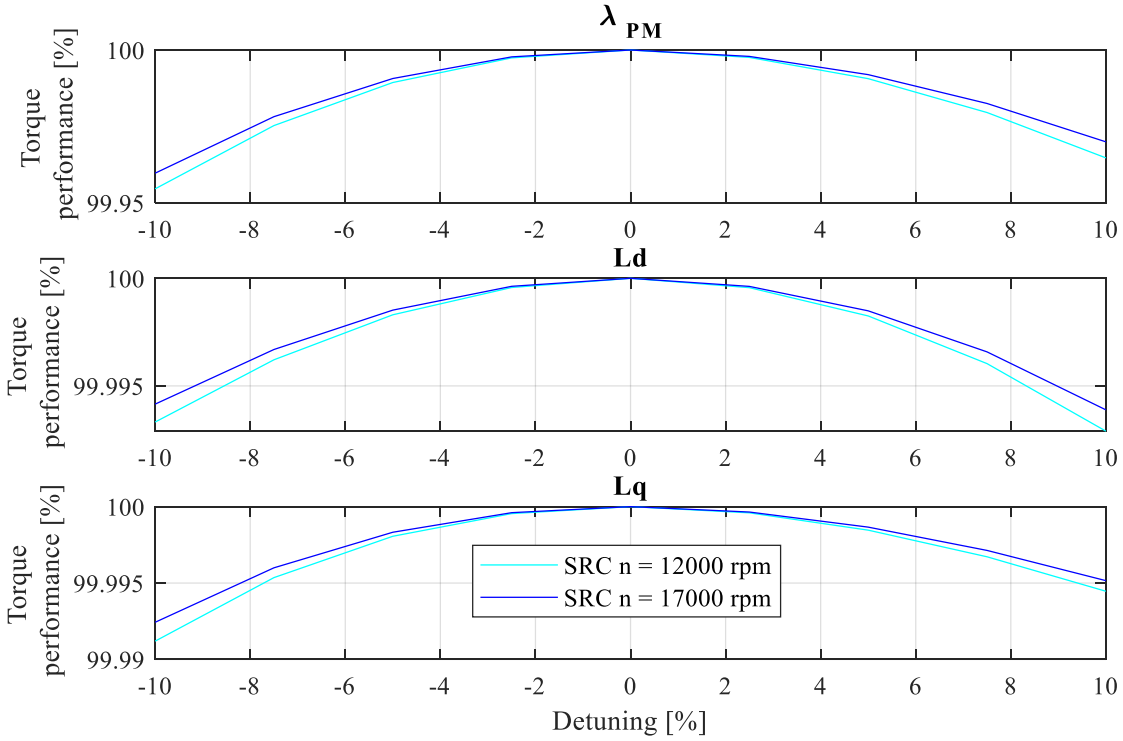

Figure 2.26: Effect of parameter estimation errors and speed on the relative torque performance with respect to the MTPF operation of the SRC method.

For all the scenarios, an asymmetry can be appreciated between increasing and decreasing the different parameters. For the detuning range shown, SRC is far superior to the CVC methods, as can be appreciated by the difference in scale between Figure 2.25 and Figure 2.26. For changes in each of the parameters, the SRC insensitivity to parameter estimation errors slightly improves with speed.

Between the CVC methods, CVC_b shows better performance at both speeds for changes in permanent magnet flux and d-axis flux, while CVC_a is better for changes in q-axis flux. As it was explained in Section 2.2.6.2.3, for this case CVC_a is equivalent to SRC.

Speed improves the performance of all systems for changes in q-axis inductance, and worsens it in the CVC methods for changes in d-axis inductance and permanent magnet flux.

2.2.7. Experimental Results

The concept of SRC as an MTPF strategy was studied during this project in [11]. As part of this study, the algorithm was implemented in two testbenches: Testbench A is the one studied in Chapter III, and Testbench B was an industrial automotive setup.

Due to the speed limitations of Testbench A, the MTPF operation was tested by reducing the flux reference for a constant torque reference at constant speed (6000 rpm) and constant DC bus (360 V). Figure 2.27 shows the results of two of these tests for different torque commands. The real MTPF line was estimated using the data from a FEA model including changing machine parameters according to the dq-current operating point. The mismatch at the short circuit current is attributed to temperature differences. The estimated MTPF line matches the path obtained experimentally by the SRC method, demonstrating experimentally that the proposed method is a valid strategy to achieve this operation.

The superior capabilities of Testbench B were used to test a control law switch from CVC to DB-DTFC for maximum torque performance at high speed (17000 rpm). The results are shown in Figure 2.28. The controller parameters were estimated for both algorithms at 75 ºC while the real rotor temperature for this test was 95 ºC. After the transition, the change in dq-current is consistent with the simulation results from Figure 2.21 and Figure 2.22. Also, the DB-DTFC makes better use of the available voltage (see modulation index subplot). As a consequence, the measured torque is increased and the total current is decreased.

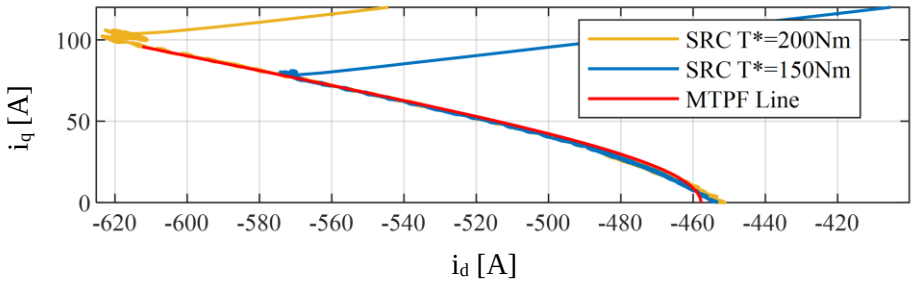

Figure 2.27: Experimental results for urrent path in the second flux weakening region applying SRC for different torque commands at constant rotor speed (6000 rpm) and a decreasing flux command [11].

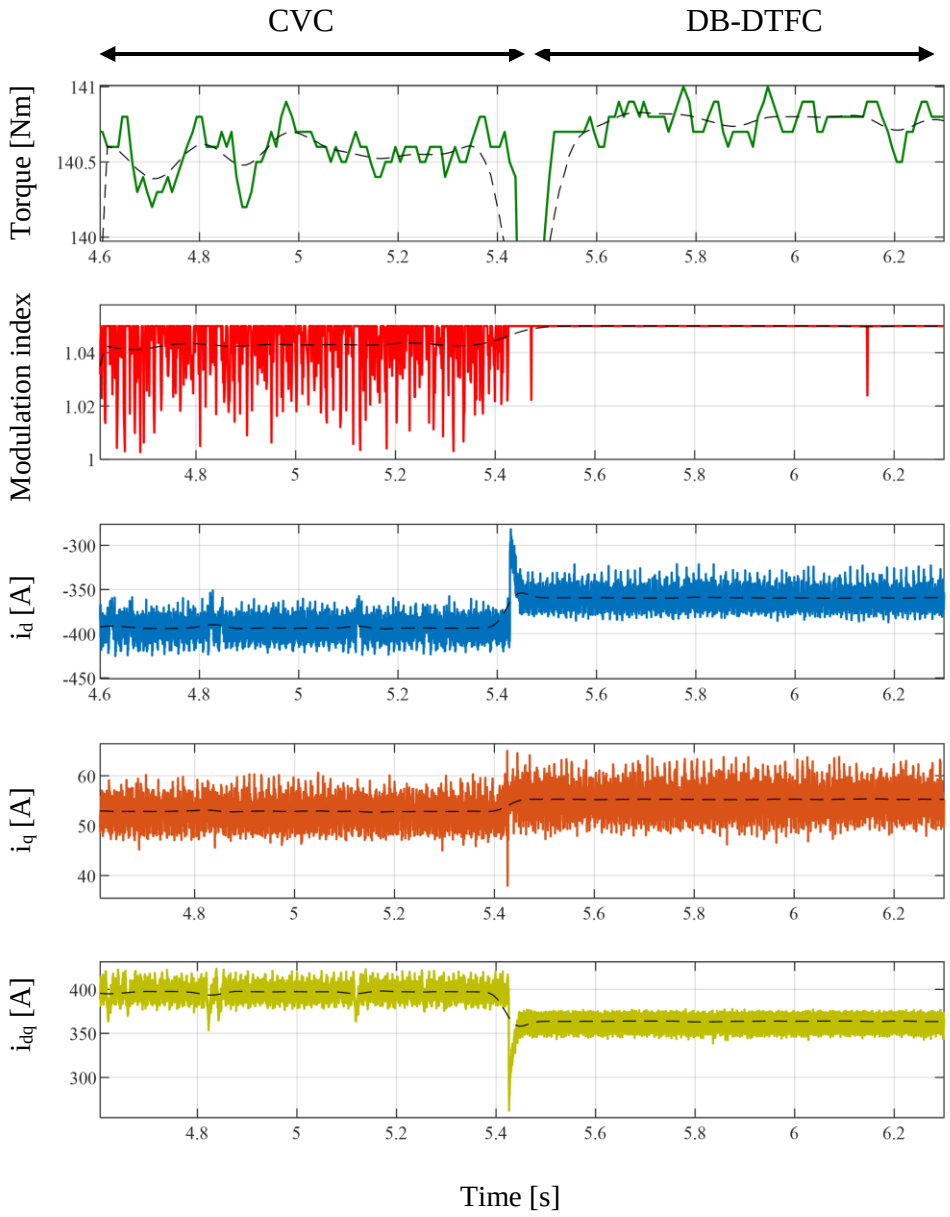

Figure 2.28: Experimental results showing the transition from CVC to closed-loop DB-DTFC in the second flux weakening region at 95 °C and constant rotor speed (17000 rpm) [11].

Finally, the limitations of the SRC as an MTPF mehtod were tested by intentionally introducing errors in the flux estimation. An angle offset is added in terms of a virtual time delay multiplied by the speed of the drive. As seen in Figure 2.29, the torque achieved decreases when the flux angle is changed (for the tested speed a delay of 16.5 µs corresponds to 5 electrical degrees). This test can also be used as a verification of flux angle estimation, as maximum torque is achieved for the correct flux angle.

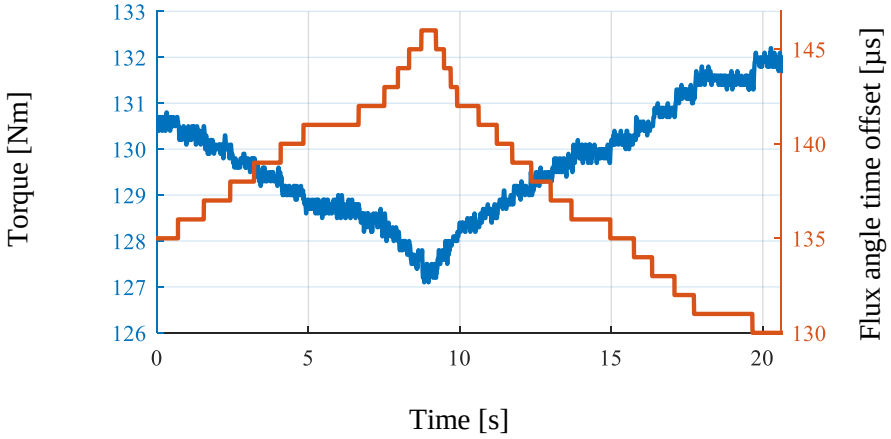

Figure 2.29: Experimental result showing the torque dependency on the flux estimation angle in the second flux weakening region for maximum torque command and rotor speed (17000 rpm) [11].

2.2.8. Proposed CVC Method and Comparison with DB-DTFC

In order for a conventional CVC method to exploit the advantages found for the SRC method, a possible scheme is shown in Figure 2.30.

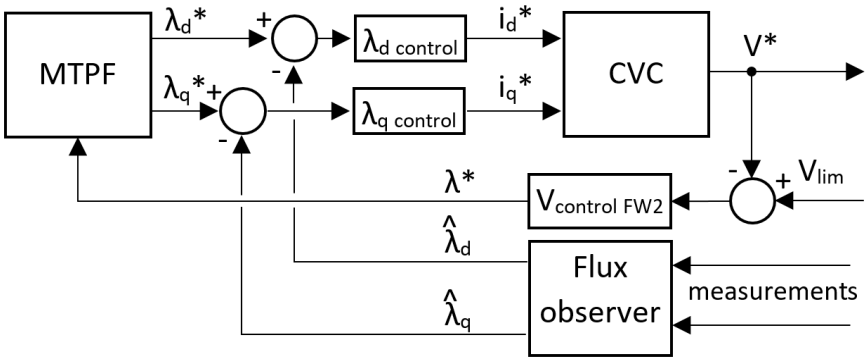

Figure 2.30: Proposed control scheme for CVC to replicate the robustness to parameter estimation errors exhibit by the SRC method.

However, the added complexity in design and computational effort needs to be considered. On the other hand, the DB-DTFC algorithm, through a combination of flux and current observers and an inverse machine model, appears to work inherently as a reference calculator and closed loop control for the dq-axis flux to match the external torque and flux

references. With very little additional computational effort, the SRC method applied to DB-DTFC successfully achieves MTPF operation for correct parameters with a single control law and exhibits extremely low sensitivity to parameter estimation errors.

2.3. Conclusions

- Several approaches were tested to generate the MTPA flux reference and their sensitivity to permanent magnet flux estimation was evaluated. A method was developed achieving low error with respect to the real MTPA flux (0.3%) for a range of 200ºC in temperature.
- The best method from the simulation tests was implemented in the testbench and was shown to reduce the current required to achieve the same torque in the MTPA region. No temperature effects were observed during this test.
- The Square Root Condition method, which emerges from the DB-DTFC equations, leads to MTPF operation under correct machine parameters and can be implemented with little additional computational effort. This has been shown analytically, in simulation and through experimental results.
- The MTPF flux line calculation in the dq-reference frame is much less sensitive to parameter estimation errors than the estimated dq-current path, especially for high speeds in which for flux the error reduces and for currents it drastically increases.
- The SRC method inherently follows an MTPF flux command calculated for the estimated parameters, exploiting the parameter insensitivity of this strategy. The analytical predictions for the transient operation of SRC in terms of flux and current were validated with simulation results.
- SRC steady state operation in terms of flux appears to be unaffected by changes in the real machine parameters. The differences can be appreciated only in partial load operations and during the transient to maximum torque in the studied cases.
- The geometries of DB-DTFC, in particular the locus for null change in torque and flux, are a useful and intuitive analysis tool to study the transient phenomena and could be applied to any controller.
- The SRC method showed better insensitivity for parameter estimation errors compared to the operation of two hybrid flux weakening schemes for CVC.

Chapter III

Implemented Algorithm in the Testbench and Data Analysis

3.1. Implemented System

At the start of this stage of the project a working DB-DTFC algorithm was already implemented in a testbench. This implementation was embedded in a complete power electronics control system analogous to those implemented in commercial vehicles, which executed ancillary tasks as signal processing, safety limitations and duty command generation from the dq-voltage command produced by the machine control algorithm.

The DB-DTFC algorithm included the stator current and flux linkage observers for IPMSM [15]. These systems successfully dealt with issues such as dead time compensation, inverter voltage drop, parameters variation, measurement sampling and current limitation in terms of torque command saturation. The implementation of the DB-DTFC was optimized, reducing the number of arithmetic functions required, and the Square-Root-Condition system (explored in Section 2.1) was included in the implementation.

The code for the final system implemented can be seen in Appendix B.1 Script B.1 [15]. The system was successful at producing deadbeat response for achievable commands (Figure 3.1), independently controlling torque and flux, and achieving finite settling step response

for initially unachievable commands in an iterative way even with parameter estimation errors (Figure 3.2).

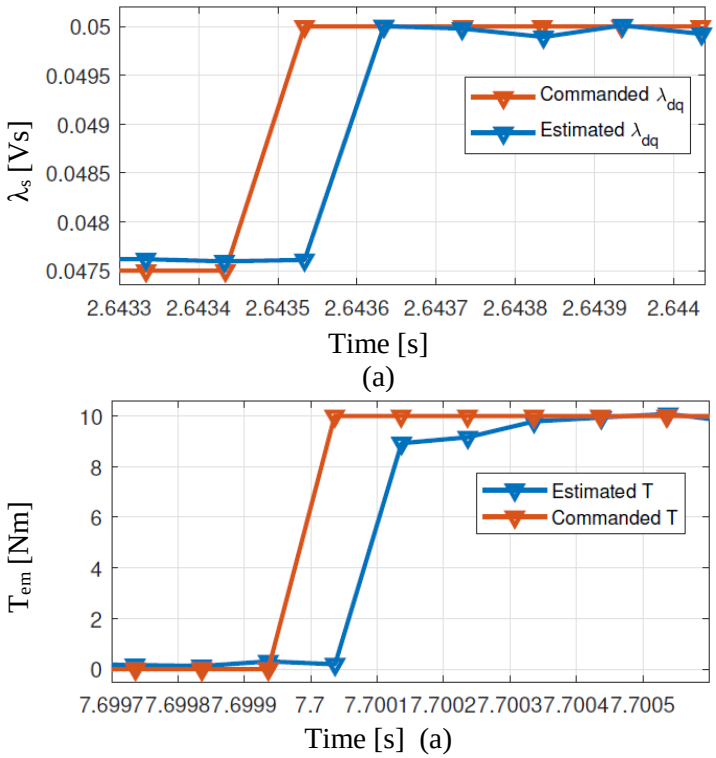

Figure 3.1: Experimental results of the deadbeat torque and flux linkage control for feasible commands and a relatively low rotor speed [15]

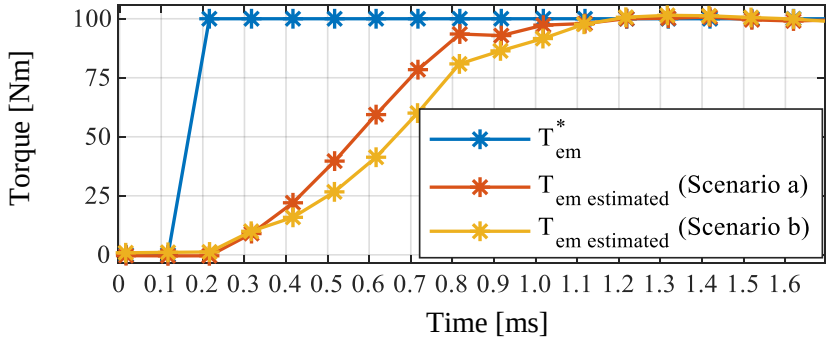

Figure 3.2: Experimental results showing the effect of detuning the permanent magnet flux on the torque response for step command in torque (100 Nm) at constant rotor speed (4000 rpm) and constant flux command (0.055 Vs) [11].

3.2. Testbench Setup and Data Analysis

The testbench employed for the implementation and testing of the DB-DTFC algorithm is described in Figure 3.3 and pictures can be found in Appendix B.2. It consists of:

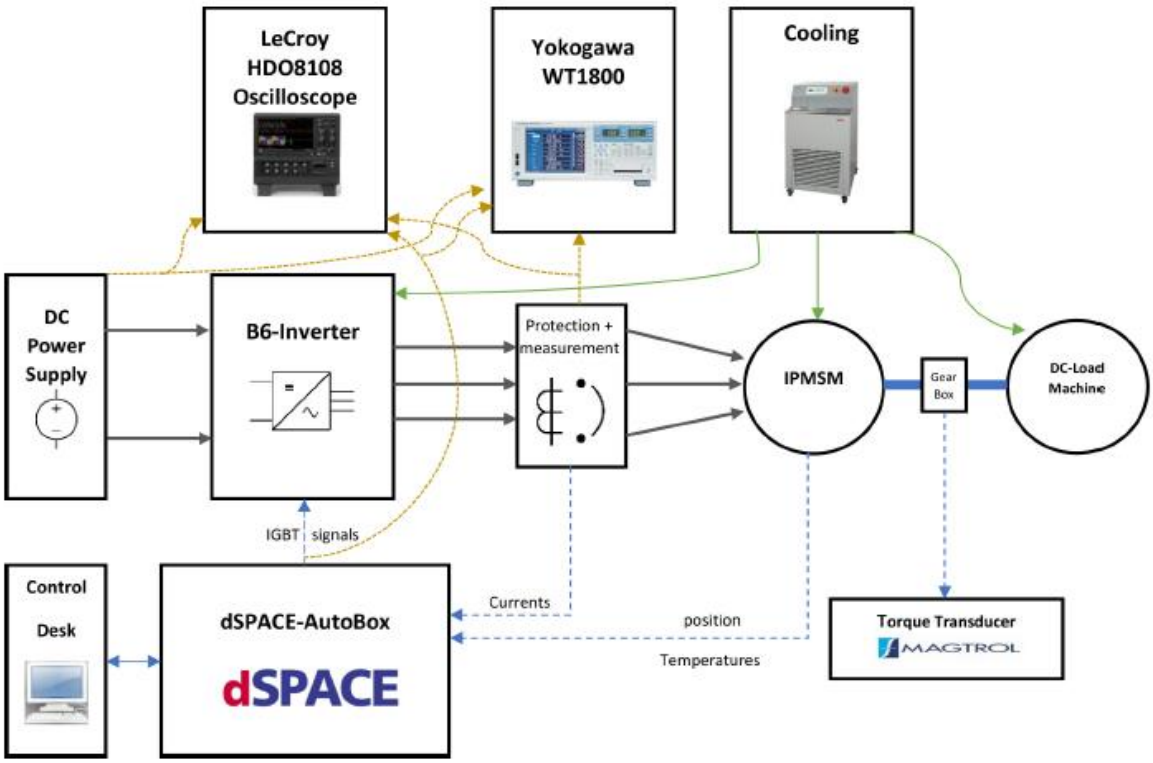

Figure 3.3: Schematic representation of the testbench employed during experimental evaluation [15].

- IPMSM machine, inverter, cooling systems, protection and measurement stage.
- DC load machine (speed controlled).
- ControlDesk application for control and monitoring of a dSPACE-AutoBox.
- GustavKlein DC power supply.
- LeCroy HDO8108 Oscilloscope: measuring the three line to line voltages, the three phase currents, DC link voltage and DC current.
- Yokogawa WT 1800 power analyser.
- Other sensors (encoder, temperature sensors, Magtrol torque transducer).

The information from the sensors and the power analyser was collected by a computer and organized through a LabView application, which allowed the recording and exportation of the data in a convenient format.

In order to process the data coming from the three data sources (dSpace stored signals, sensors measurements and oscilloscope), multiple scripts were developed. The goal of this part of the project was to create a general set of programs that could read the data, organize

it in a more usable format and perform the appropriate analysis on a flexible yet automatized way. These programs were developed also with the intention of their continuous use by other people using the test-bench. For this purpose, the algorithm followed by the scripts is explained in detail in Appendix B.3 to B.8 and are briefly described in the following section.

3.2.1. Data Analysis Scripts

The format chosen for the data was a MatLab structure, with the different categories corresponding to aspects changed between experiments (algorithm used, speed, torque or parameter settings). This format was chosen as it allowed the naming and calling of data in a meaningful way while still permitting the program to work with little input from the user.

The data analysis can be performed from a 'Main Script' which starts by providing the names for the different measurements according to the experiment to which they correspond. This is achieved by means of a table containing an identification corresponding to each measurement and by assigning specific names to the columns and rows of that table. Inside each of the specific scripts for each measurement, these tables and names will be called to form conform the names of the categories of the structure that will store the data.

There are four main types of experiments that are analyzed this way:

- Continuous tests: in which the objective is to see the evolution of the system with continuously changing parameters. In this case the data from the dSPACE and the sensors are used.
- Steady state tests: in which the objective is to analyze the characteristics of a specific operating point. In this case the three data sources can be involved.
- Transient tests: in which the objective is to evaluate the transition between two operating points. This analysis uses only the data by the dSPACE system.
- Synchronization tests: used to evaluate the correctness of the angle estimation in the system. They involve the synchronization of the dSPACE and oscilloscope data with the use of some drastic transient in one of the observable signals by both systems.

The signal processing in general follows the following order:

1. Reading data
2. Merging/synchronizing data
3. Data analysis
4. Plotting/displaying results

The original data format and information included by the exported measurements from each of the instruments is shown in Table 3.1

System	Data format	Information
dSPACE	Matlab structure (.mat)	Time: instants of data acquisition of the different timers used Data recorded: also including name, path and timer used
LabView measurements	Excel file (.xlsx)	Time and data recorded (all at same time interval, defined by the user)
Oscilloscope	Excel file (.csv)	One file per signal containing time and data values

Table 3.1: Data format and information included in the exported files form the different measurement instruments.

The reading, merging and synchronization of the data was a very challenging task that required extensive time and iteration for achieving a satisfactory result. The scripts work with a combination of user input (for example in the data window selection and the synchronization of data between sources) and automatized analysis. The result was a series of scripts that can seamlessly extract, process, store together and synchronize the valid data from the different sources. This was combined with analysis tools (such as frequency and statistical analysis) and plotting programs that took advantage of the new convenient format of the data. Despite most of these analyses not being part of the present report (since their objective was to study other parts of the project or the systems studied were discarded), they were of great importance during the developing of the project, allowing quick testing and evaluation of different algorithms and system tuning. Some of these studies are presented in the following subsections.

3.2.2. EMF Frequency Analysis

To test the capabilities of the scripts created, the back-EMF induced in the stator windings at three different speeds was measured and the data was exported using the oscilloscope. The signals are displayed in Figure 3.4 together with a superposed approximation including the first 20 harmonics, showing the Fourier analysis is accurate. The frequency spectrum can

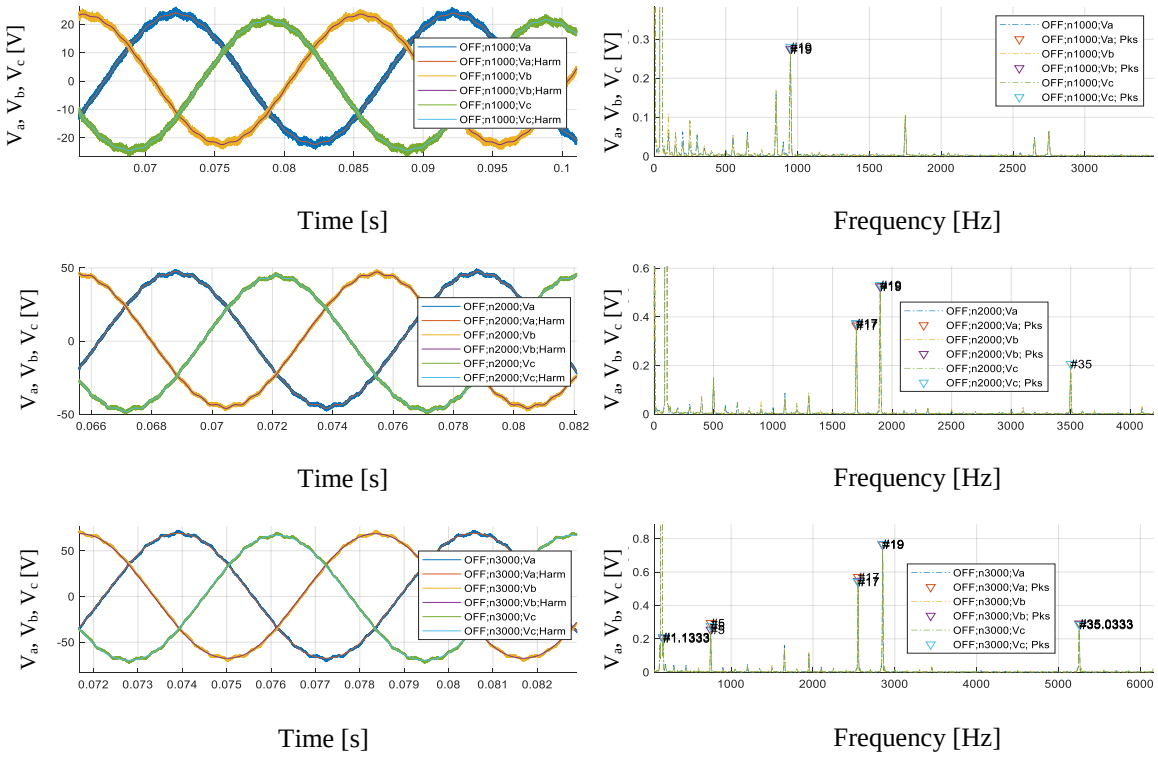

Figure 3.4: Time and frequency domain analysis of the back-EMF measurement at three different speeds (1000, 2000 and 3000 rpm).

also be seen in Figure 3.4, zoomed in to appreciate the harmonic content of the signals (a more detailed view of this analysis can be seen in Appendix C.1). The actual measurement was the line to line voltage, which was converted to phase voltages assuming a balanced system. This conversion may not be a faithful representation of the actual system (i.e. the measurement in line to line may remove some components that would be present in the actual phase voltage, and the conversion back to phase voltages cannot recreate these missing components).

Some harmonics are rejected during the search for peaks (5^{th} harmonic was not big enough to be recognized until n=3000 rpm). Some harmonics are wrongly detected (at 1.33^{th} for n = 3000 rpm), and after this analysis the harmonic detection scheme was improved. The data for the DC component and the 1^{st}, 17^{th} and 19^{th} harmonic is shown in Table 3.2. From this analysis, an imbalance can be seen between the phases, in terms of the DC offset difference and the fundamental component amplitude. Additionally, these results were used to validate the permanent magnet value estimation, which is important to avoid drawing current during null torque commands (following an incorrect flux reference).

			DC	1st Harmonic	17th Harmonic	19th Harmonic
n = 1000 rpm		Frequency [Hz]	-	50.000	850.000	950.000
	Va	Amplitude [V]	0.819	22.894	0.168	0.276
	Vb	Amplitude [V]	0.624	22.734	0.153	0.274
	Vc	Amplitude [V]	-1.443	22.851	0.172	0.281
n = 2000 rpm		Frequency [Hz]	-	100.000	1700.000	1900.000
	Va	Amplitude [V]	0.880	45.862	0.364	0.528
	Vb	Amplitude [V]	0.621	45.686	0.373	0.525
	Vc	Amplitude [V]	-1.50101	45.839	0.375	0.532
n = 3000 rpm		Frequency [Hz]	-	150.000	2550.000	2850.000
	Va	Amplitude [V]	0.819	68.803	0.570	0.765
	Vb	Amplitude [V]	0.562	68.561	0.545	0.767
	Vc	Amplitude [V]	-1.382	68.816	0.542	0.769

Table 3.2: Harmonic content of the measured back-EMF phase voltages at three different speeds

3.2.3. Voltage Command and Measured Voltage Comparison

During general tests it was observed that the voltage command and the achieved measured RMS voltage by the power analyser did not coincide. This motivated the effort to export data from the oscilloscope and evaluate if the voltage commands were being achieved as expected, both in terms of angle and amplitude.

The first test to asses this situation was performed employing CVC as the control algorithm. The reference in the q-axis current was set to 0 while the d-axis current was set to different values, and for each of them the speed was increased from 0 to 6000 rpm. If the angle estimation was correct, no torque should be measured (the only effect would be to weaken the flux in the machine).

However, as can be seen in Figure 3.5, a non-zero torque was measured throughout the speed range. Two scenarios are shown corresponding to the two torque measurements available in the LabView application, but the results are analogous. The angle error was estimated assuming that the total amplitude of the current was the command value, and the torque was due to this current being set not perfectly in the d-axis but generating a q-axis current component. According to this study, the error oscillates between -1 and 1.5 electrical

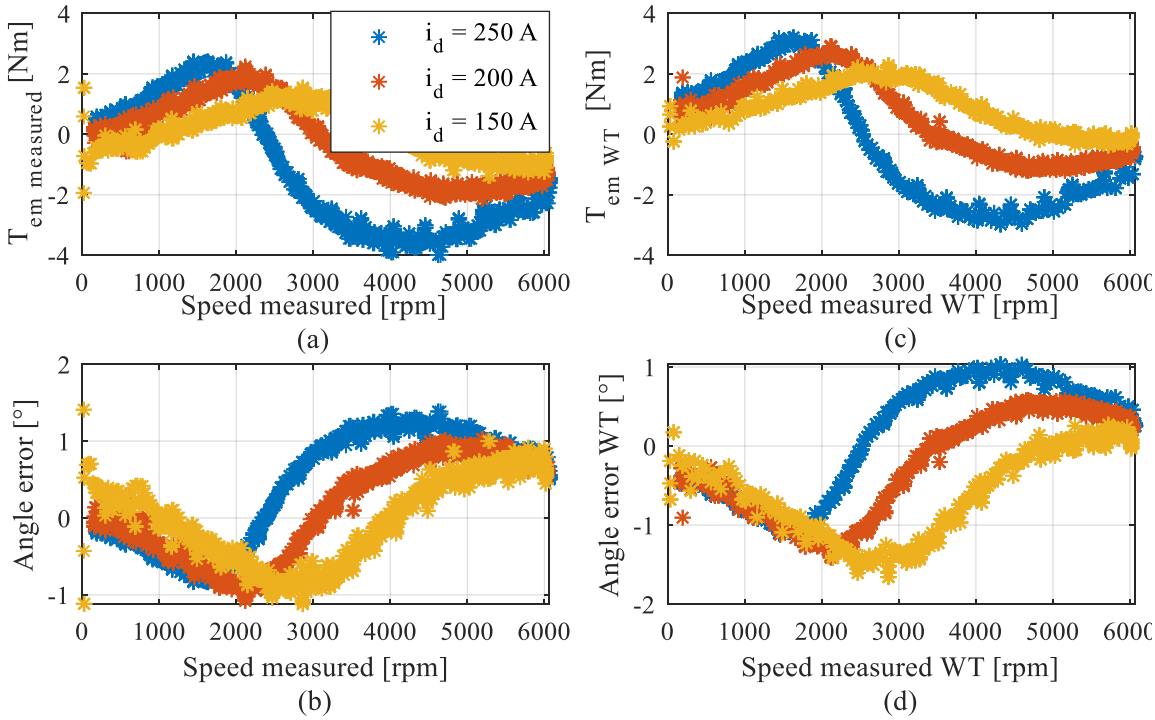

Figure 3.5: Experimental results for torque measurement and angle error estimation during CVC for i_{qs}^* = 0 A and i_{ds}^* = 150, 200 and 250 A

degrees. The pattern given by the torque is dependent on the total current (or on the flux on the machine). Some simulations where performed attempting to recreate this effect in order to determine the source of this error but this effort was not successful.

In order to evaluate this effect for DB-DTFC operation, some other tests were performed. The oscilloscope line to line voltages were stored and analysed for two different values of the DC link voltage (100 and 200 V) and a constant torque (50 Nm) for four different speeds (500, 1000, 1500 and 2000 rpm). The waveforms can be seen in Appendix C.2, and the results are summarized in Table 3.3. The total RMS (which is the value given by the power analyser) should not be used to evaluate directly if the command voltage is being achieved, due to the high harmonic content of the signal and the dependency on DC voltage.

The voltage command by the dSPACE system and the measurement by the power analyzer were also recorded during this test, in order to validate them with the frequency analysis of the oscilloscope waveforms. Some issues with the voltage probes were detected and corrected due to this analysis. The results are displayed in Figure 3.6, where the values were converted to phase voltages in order to have a consistent reference in the plot. The results show the power analyzer measurement coincides with the frequency analysis (Figure 3.6 (b), for the

	n [rpm]	Frequency [Hz]	V_1 [V_{peak}]	V_1 [V_{RMS}]	V_{total} [V_{RMS}]	THD [%]
V_{DC} = 100 V	500	25.000	22.435	15.864	39.289	211.1
	1000	50.000	42.609	30.129	53.008	129.4
	1500	75.000	64.143	45.356	64.067	88.3
	2000	100.000	85.688	60.590	73.506	58.6
V_{DC} = 200 V	500	25.000	22.175	15.680	56.284	312.0
	1000	50.000	43.098	30.475	76.061	210.5
	1500	75.000	64.194	45.392	91.644	161.9
	2000	100.000	85.475	60.440	104.971	131.1

Table 3.3: Frequency analysis of line to line voltages for a constant torque command (50 Nm) for different speeds (500, 1000, 1500 and 2000 rpm) and DC voltage values (100 and 200 V).

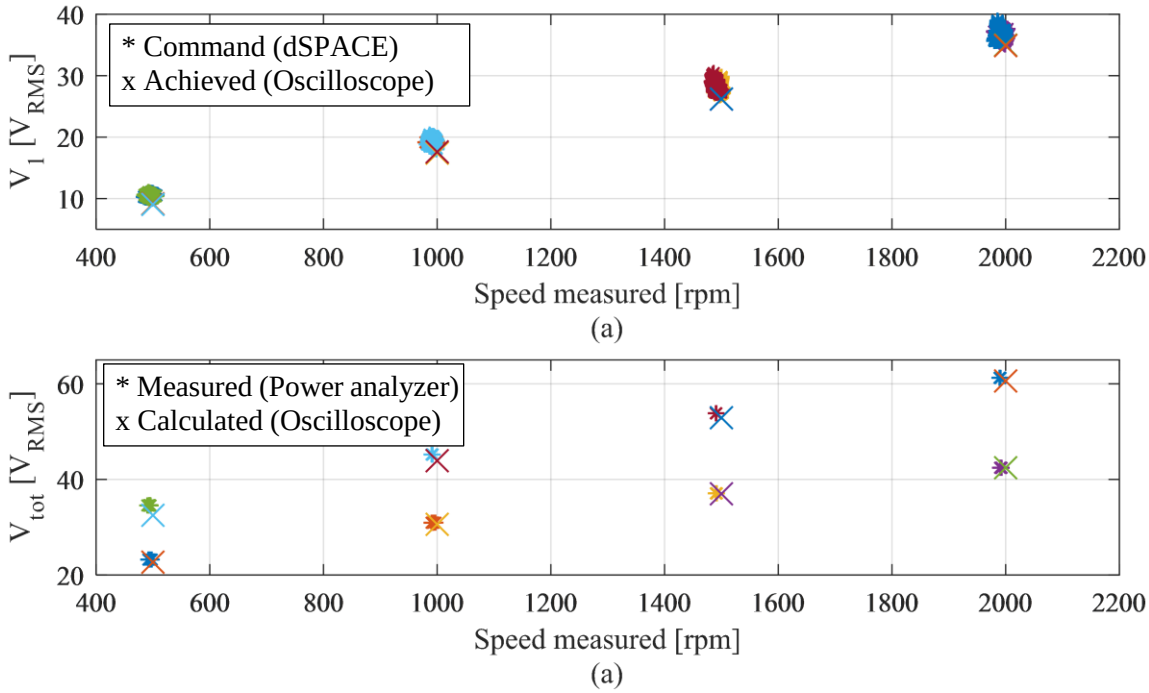

Figure 3.6: Comparisson of command and measured phase voltage given by each of the data sources (a) Fundamental RMS (b) Total RMS.

same speed there are two distinct points corresponding to the different DC bus values). Also, the fundamental voltage command is close to the achieved one (Figure 3.6 (a)), although some differences can be appreciated. This issue was investigated further.

In order to accurately evaluate the phase delay between command and achieved voltage, a shared signal between the oscilloscope and the dSPACE system was required to act as a trigger. Since such signal was not available, in order to synchronize the two measurements a

recognizable step in the current was introduced. This was done by setting the flux command to the permanent magnet flux value and recording a torque step from a high torque command to 0. The time window captured by the oscilloscope was increased to enable the capture of this step. The synchronization process can be seen in Appendix C.3, and the results are summarized in Table 3.4.

		Oscilloscope	dSPACE	Measurement - Command	
Va	Frequency [Hz]	100.001	99.773	0.228	
	V_1 [V_{peak}]	45.681	38.583	7.097	Delay [º]
	Angle [rad]	-2.555	-2.372	-0.183	10.480
Vb	Frequency [Hz]	100.001	99.773	0.228	
	V_1 [V_{peak}]	45.810	38.609	7.200	Delay [º]
	Angle [rad]	1.637	1.819	-0.182	10.433
Vc	Frequency [Hz]	100.001	99.773	0.228	
	V_1 [V_{peak}]	45.835	38.645	7.190	Delay [º]
	Angle [rad]	-0.461	-0.277	-0.184	10.563

Table 3.4: Frequency analysis of phase voltages and comparison with voltage command after synchronization.

This analysis shows a difference between voltage command and measurement both in terms of amplitude increase and phase delay. This analysis was repeated for more operating points, but the results obtained were not conclusive and for space constraints are not shown in this report. This line of research was abandoned for prioritizing other parts of the project, as are the operation at the voltage limit and in the second flux weakening region. However, this indicated that the voltage command is not very accurate in terms of phase, which is an important factor in the overmodulations strategies.

3.3. Conclusions

- The implemented DB-DTFC algorithm in the testbench is capable to achieve deadbeat operation, independently control torque and flux, and reach the desired operating point in multiple steps for initially unachievable commands.
- The data sources and exported files were studied and suitable data processing programs were developed to extract and store the available information. Other programs integrated, analysed and displayed this data in order to provide better insight into the behaviour of the machine and the measurement instruments.

- The back-EMF induced at different speeds was analysed demonstrating the capabilities of the frequency analysis and validating the permanent magnet flux estimation
- Issues with the voltage command and actual stator voltage were detected and analysed, exposing a disparity both in terms of amplitude and phase. Other tests showed from a different approach the existence of an operating point dependent rotor angle estimation error.

Chapter IV

Overmodulation for DB-DTFC

4.1. Introduction

4.1.1. Linear Operation

Making a better use of the inverter voltage is highly desirable as it extends the constant torque region and allows for higher flux in the flux weakening region, increasing the torque and power capabilities of the drive. The inverter voltage utilization is given by the modulation index. Throughout this project, the modulation index is considered as Equation 4.1

$$M = \frac{V_{s1}}{V_{dc}/\sqrt{6}} \tag{4.1}$$

in which V_{s1} is the stator voltage fundamental amplitude in RMS units. In this convention, if the modulation index is lower or equal to 1, the operation is in the linear region. Graphically, this means the voltage vector is inside the circle inscribed in the hexagon limit (Figure 4.1 [19]).

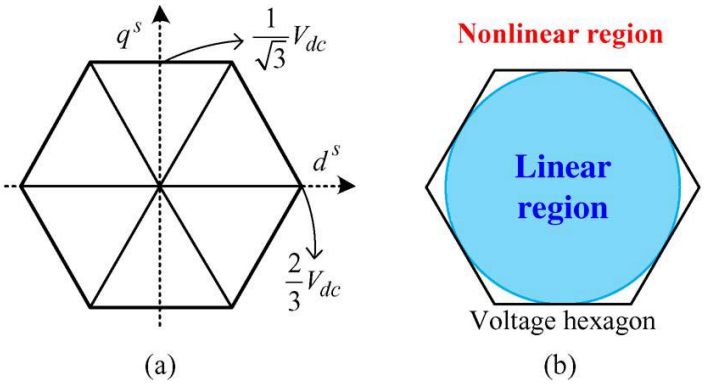

Figure 4.1: Voltage limit in the stator reference frame (peak convention) [18]

Higher modulation indexes can be achieved applying overmodulation techniques. These methods use the sections not covered by the linear region (extra area inside the hexagon, hexagon sides and corners) to increase the fundamental value of the applied voltage. In this effort, they inject low frequency harmonics that disturb the operation and generate noise and ripple in the controlled and uncontrolled variables.

The maximum modulation index, corresponding to six step operation, will be M = 1.103. During the six-step operation, the phase voltages provided by the inverter are square waves and there is no pulse width modulation. This minimizes switching losses and maximizes the value of the fundamental voltages, but produces significant harmonics

4.1.2. Overmodulation Methods

Generating a suitable reference for obtaining the desired behavior in the controlled variables is challenging outside the linear region, as the degrees of freedom are reduced due to requirement to stay within the physical limitations. Moreover, these methods add a nonlinear component to the reference generation, as the modulation index does not depend linearly on the command voltage amplitude as seen in Figure 4.2 [19]. In this figure the modulation index is calculated with respect to the six-step fundamental amplitude ($M = V_{s1}/\left(\sqrt{2} * \frac{2}{\pi} V_{dc}\right)$), and so the nonlinear region starts from M = 0.907.

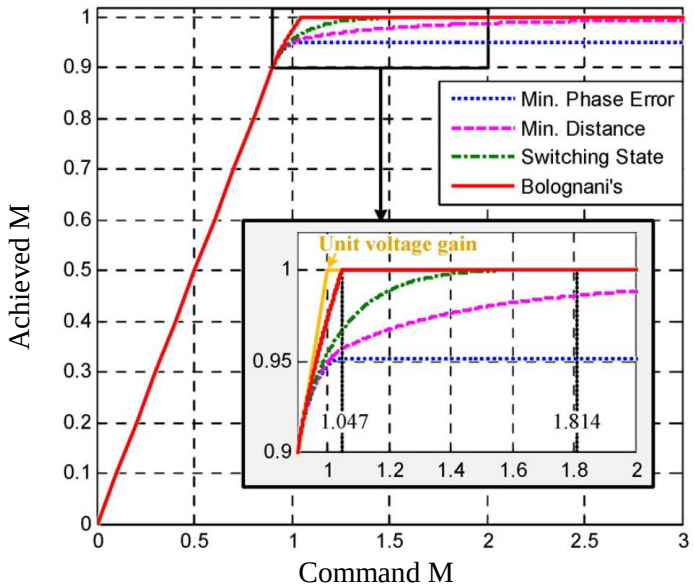

Figure 4.2: Command vs achieve modulation index for clasic overmodulation techniques [18].

It is important to note that some of these methods are not capable to achieve six step operation, as can be observed for the minimum phase error method in Figure 4.2.

4.1.3. Voltage Selection

DB-DTFC inherently offers an intuitive and graphical approach to the voltage selection. Because of this, the consideration of the voltage limits and its effect on the control based on the algorithm principles is possible, and specific strategies to achieve overmodulation and six-step operation can be developed. In this project, an analogous switching table to DTC was generated from the DB-DTFC geometries, as is explained in Section 4.3.

4.2. Reference Adaptation Methods

4.2.1. Amplitude Conservation and Phase Conservation Methods

Two methods were initially considered for implementation in the system (described in Figure 4.3):

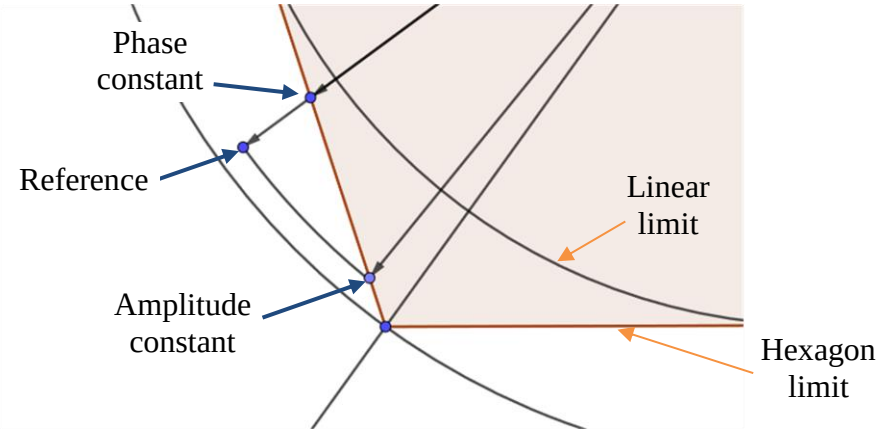

Figure 4.3: Amplitude constant and phase constatn overmodulation techniques diagram.

- Minimum amplitude error (constant amplitude): if the reference lies outside the hexagon limit, the closest voltage vector with equal amplitude will be chosen. In the case of the amplitude being bigger than the corner voltage, the closest corner will be chosen.
- Minimum phase error (constant phase): the amplitude of the command is trimmed to the voltage hexagon, and the phase is unmodified.

Due to the transformation between a circumference limit to an hexagonal limit, the fundamental harmonic achieved in the final waveform is lower than the command one, and this relation depends on the overmodulation strategy (Figure 4.2). This relation for both overmodulation strategies was evaluated as a function of the modulation index using frequency analysis of multiple waveforms obtained in simulation. The results were stored, and a reference adaptation stage was implemented with LUTs to compensate for this issue. The simulation results for an open loop application of these methods is shown in Figure 4.4 in the stationary reference frame. Both methods require accurate estimation of rotor angle to properly estimate the voltage limit (hexagon position) at each time.

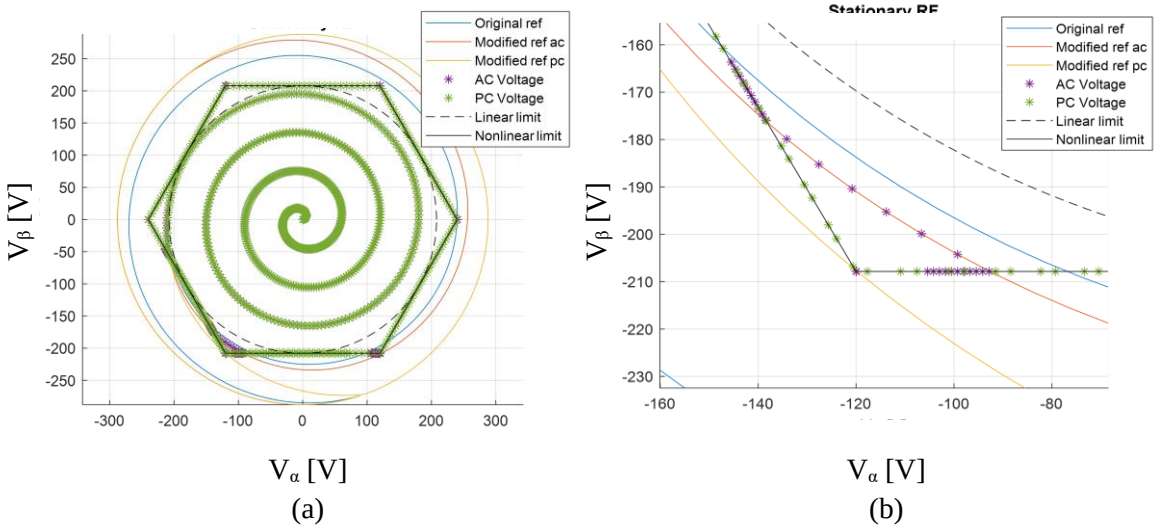

Figure 4.4: Reference adaptation and voltage command given by the amplitude conservation (AC) and phase conservation (PC) overmodulation methods in open loop simulation. (a) Zoomed out view (b) Zoomed in view.

4.2.2. Angle Removal Method

When implemented in simulation in closed loop, the amplitude conservation method proved uncapable of achieving a stable operation during overmodulation. This was attributed to the ripple and noise in the controlled variables combined by the high angle modification sensitivity of the method (a small change in reference amplitude produces a big change in the modified reference angle). Therefore, the phase conservation method was chosen to be implemented for experimental testing.

However, the phase conservation method is uncapable of achieving six-step operation. To overcome this issue, a new overmodulation technique was designed to be applied from the

point in which the phase conservation method only uses the hexagon side (M* = 1.05), and therefore cannot increase the fundamental amplitude any longer.

The objective of this method was to create a range of "forbidden angles" starting from the center of the hexagon side. This way, according to the modulation index, the allowed sections of the hexagon side would be progressively smaller, ending with just the corners when the modulation index reached the upper limit. The implemented algorithm is shown in Figure 4.5 and has the following steps:

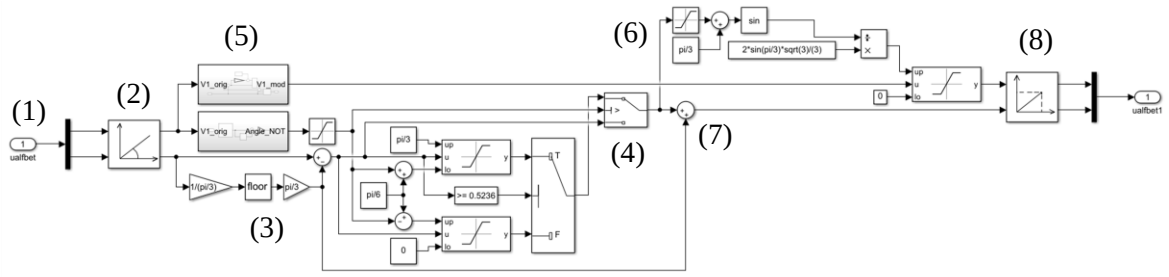

(a)

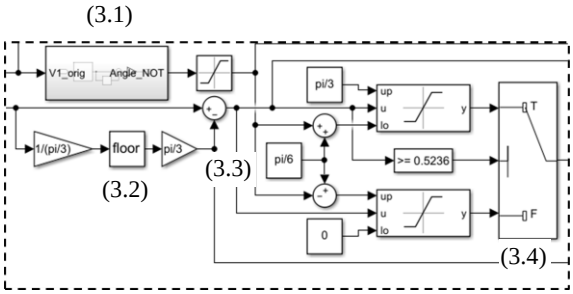

(b) – Detailed view of (3)

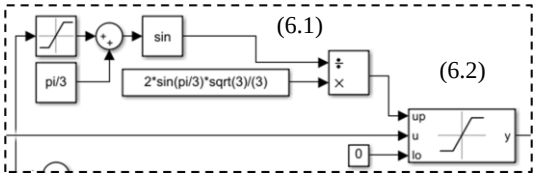

(c) – Detailed view of (6)

Figure 4.5: Reference adaptation scheme combining phase conservation method with angle removal method. (a) Complete scheme (b) Detail for angle removal method (c) detail for amplitude saturation.

(1) The normalized reference (Equation 4.2) from the controller is received in the dq-reference frame

$$u_{\alpha\beta} = \frac{V_{\alpha\beta}\sqrt{3}}{V_{dc}} \tag{4.2}$$

(2) Transformation to polar coordinates

(3) Angle removal method

(3.1) The "forbidden angle" value is obtained through a LUT based on the command voltage amplitude. This value is saturated to ensure it stays between 0 and π/6 rad.

(3.2) The voltage angle is shifted so that it stays between 0 and π/3 rad. The removed angle will be an integer times π/3 and will be added back to the modified angle in (7)

(3.3) The forbidden angle is added and subtracted to π/6 to create the forbidden angle region in the middle of the hexagon side. The shifted voltage angle from (3.2) is then saturated using this limit

(3.4) According to the shifted angle from (3.2) relative position to the middle of the hexagon, the upper or lower saturated angle is chosen (i.e. if the shifted angle is above π/6, the angle chosen will be the shifted angle saturated between π/6 plus the forbidden angle and π/3)

(4) If the forbidden angle was different from 0 (i.e. the angle removal method is supposed to be active), the modified angle from (3.4) is chosen, else the chosen angle will be the shifted angle form (3.2)

(5) The modified amplitude is obtained through a LUT based on the command voltage amplitude (as done in Figure 4.4)

(6) Amplitude saturation to the hexagon side

(6.1) Using the selected angle from (4), the hexagon side amplitude is calculated as Equation 4.3 [20], matching the normalization method employed before (1)

$$|u_{s\,max}| = \frac{2\sqrt{3}}{3}\frac{\sin\left(\frac{\pi}{3}\right)}{\sin\left(\frac{\pi}{3}+\gamma\right)} \tag{4.3}$$

where γ is the angle from (4)

(6.2) The voltage amplitude selected is the smallest between the adapted amplitude from (5) and the hexagon limit from (6.1)

(7) The angle shift from (3.2) is undone

(8) The cartesian vector is reconstructed from the selected voltage amplitude and phase.

In open loop, the results from applying this method to an increasing voltage reference are shown in Figure 4.6

4.2.3. Duty Saturation Method

A different method that can achieve overmodulation was already implemented in the testbench and is discussed here for comparison purposes. The original algorithm followed the following steps (this includes functions not exclusive to overmodulation, as reference frame transformation and other modulation techniques):

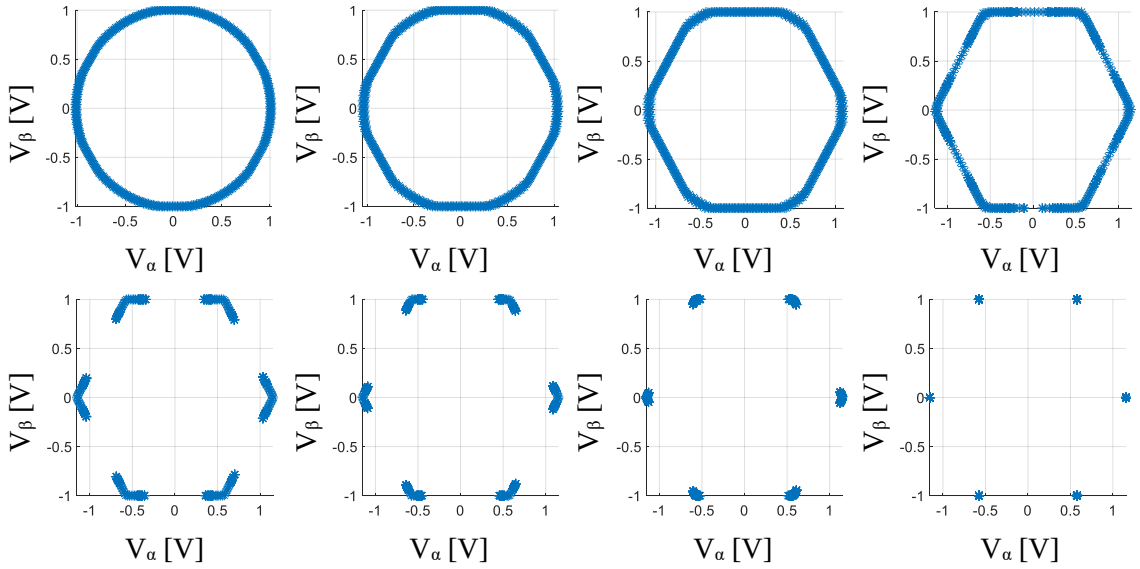

Figure 4.6: Adapted voltage reference by the combined method for increasing voltage command in open loop simulation.

(1) Obtention of dq-voltage references from the control algorithm

(2) Normalization according to Equation 4.4

$$u_{dq} = \frac{V_{dq}\sqrt{6}}{V_{dc}} \tag{4.4}$$

(3) Conversion to the stationary (αβ) reference frame

(3.1) Calculation of the normalized amplitude

(3.2) Calculation of the amplitude modification factor (by means of a LUT (analogously to Section 4.2.1)

(4) Conversion to abc-reference frame

(5) Triplen harmonic injection

(6) Multiplication by the amplitude modification factor

(7) Calculation of duty cycles according to Equation 4.5 and saturation between 0 and 1

$$d_{a\ unsat} = (u_a + 1)/2 \tag{4.5}$$

where u_a is the normalized voltage command for phase a after modification.

(8) Modulation strategy: depending on different adjustable values the duty signals are modified to produce references that achieve:

(8.1) Discontinuous PWM: alternative clamping to 0 or 1 of the closest phase to either of those values

(8.2) Clamping of the uppermost phase to 1

(8.2) Clamping of the lowermost phase to 0

(8.2) GDPWM

(9) Deadtime compensation

(10) Duty signal saturation between 0 and 1

The effect of steps (6) and (7) can achieve overmodulation when the duty command is modified to be below 0 or above 1. The effect of the saturation will then be to clamp the duty signal to 0 or 1 respectively, and if this happens in all the phases simultaneously the operation is maintained at one of the hexagon corners. This method will not skip specific parts of the hexagon but will go through the hexagon side faster the bigger is the voltage command, clamping the operation at the hexagon corner the rest of the time. This is illustrated in Figure 4.7.

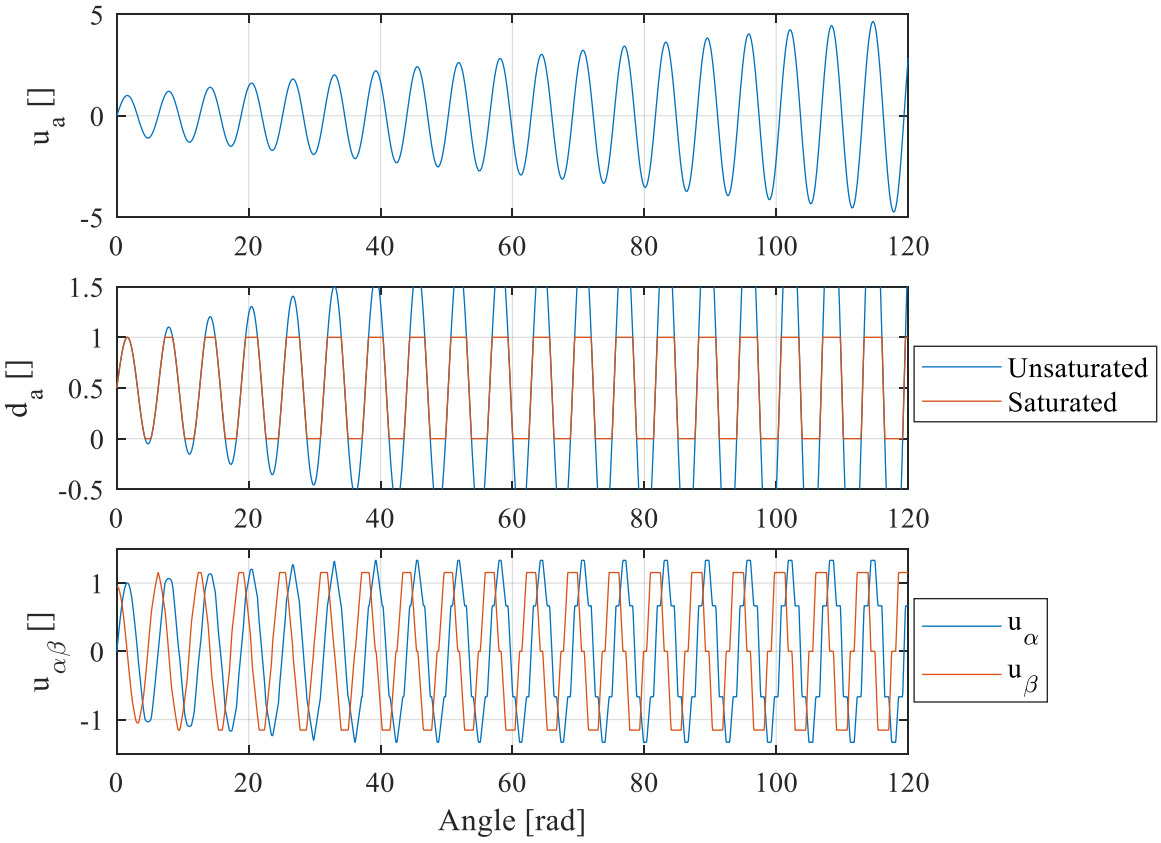

Figure 4.7: Originally implemented overmodulation strategy based on duty signal adaptation and saturation.

The transition between null and maximum duty is made faster by the increase of the amplitude command, and it can be appreciated in the αβ-voltages how the operation transition

from linear (sinusoidal, first period), through the hexagon limit (angles from 20 to 40 rad) to six-step (last periods). The operation never truly reaches the six-step operation, as this would require a completely vertical transition between null and maximum duty (infinite voltage command), but it gets close enough that it is virtually indistinguishable.

An open loop simulation including this technique and the combined method proposed in Section 4.2.2 was executed to compare the action of the two reference adaptation stages, and the results are shown in Figure 4.8. For a high modulation index command as the one in the figure, the original method will be clamped (horizontal lines) at the hexagon vertexes (purple line is superposed to six-step line) during some time, transitioning linearly between them. On the other hand, the proposed method will be clamped at another point close to the vertex, and transitioning between these points either instantaneously (vertical lines) or following the hexagon limit (green line is superposed to hexagon line).

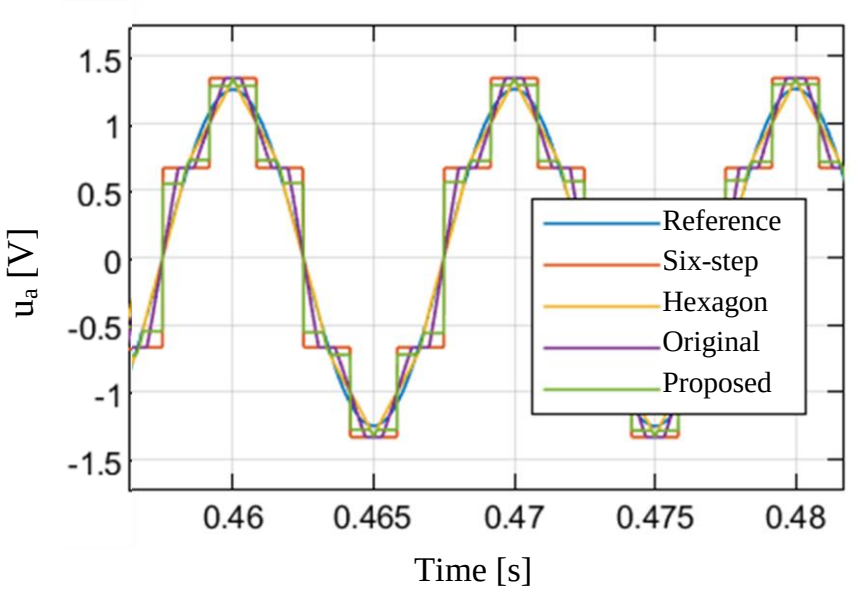

Figure 4.8: Comparisson of duty saturaition (original) overmodulation method with the proposed method in terms of normalized phase voltage achieved in open loop simulation.

This indicates that the proposed method combining the phase conservation with the angle removal method may be a very disruptive method, despite being originally designed to produce a voltage as close as possible to the original reference. A frequency analysis was performed to determine the harmonic injection for each of these methods. The results are shown in Figure 4.9. The new method produces the fundamental voltage slightly more accurately than the original one (see 1st harmonic plot) especially in the neighborhood of M=1.05. However, the new method consistently produces more harmonics than the original.

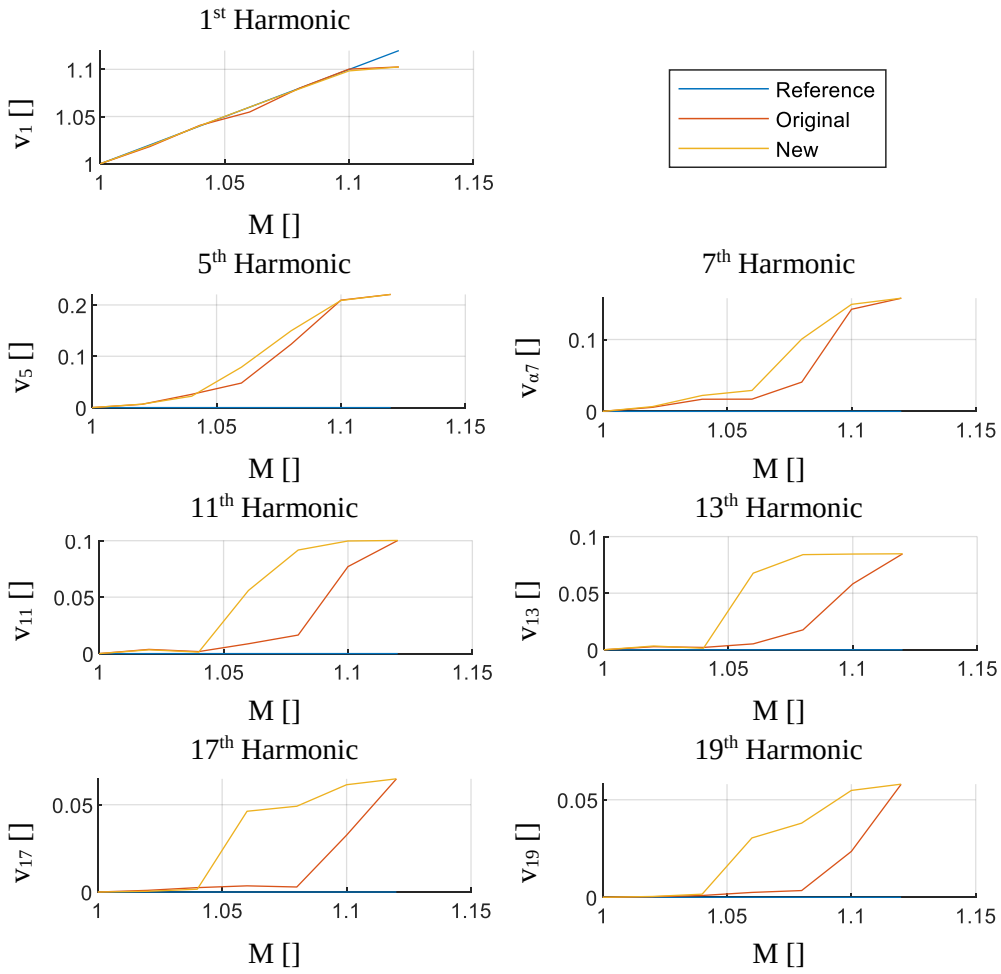

Figure 4.9: Harmonic content comparisson between the originally implemented overmodulation method and the proposed method in open loop simulation.

It is also noteworthy how the duty saturation method can produce a fundamental component very close to six-step (when M = 1.1) with lower harmonic content in the harmonics higher than 7th. This is consistent with the notion that this method does not totally achieve six-step unless the command amplitude is very high. The experimental results for the implementation of these and other overmodulation strategies is studied in Section 4.4.

4.3. Voltage Selection in DTC and DB-DTFC

The DTC algorithm was studied as an alternative method to achieve overmodulation and six-step operation (by implementing a transition from DB-DTFC) and to modify the DB-DTFC algorithm so that an analogous voltage selection method could be employed for maximum inverter utilization.

4.3.1. DTC Algorithm

In Section 1.3.2 the basic principles of DTC were described. However, the assumptions for the general implementation are not always valid. For IPMSMs where there is significant saliency, the torque equation can be written in terms of the flux linkages as Equation 4.6 [8]

$$T_{em} = \frac{3P\lambda_s}{4L_dL_q}\left(2\lambda_{pm}L_q \sin\delta + \lambda_s(L_d - L_q)\sin 2\delta\right) \tag{4.6}$$

where δ is the flux angle in the dq-reference frame. The saliency allows the second term to make the change in torque evolve in a different direction to the change in flux angle, depending on the values of the parameters involved. This is shown in Figure 4.10 [9].

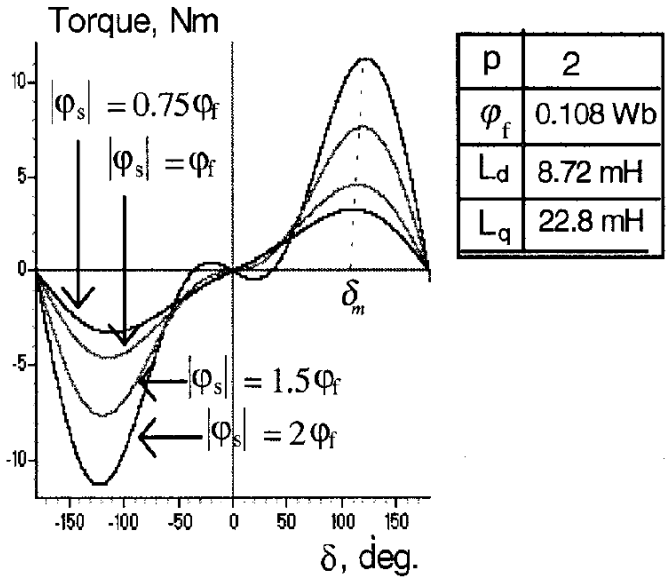

Figure 4.10: Torque dependancy on flux angle for various stator flux values [9]

The derivative of torque with respect to flux angle is negative for two instances:

- Near zero flux angle when the flux amplitude is higher than the limit in Equation 4.7 [9]

$$\lambda_s < \frac{L_q}{L_q - L_d}\lambda_{pm} = a \tag{4.7}$$

Attempting to solve this problem by establishing this flux limit would limit the torque and power capabilities of the drive, and therefore in the implemented system this condition is ignored. The torque change will initially evolve opposite to the command, but this will be corrected in time when the flux angle is high enough.

- For all flux amplitudes when the flux angle goes beyond the MTPF point (δ_m), which can be expressed as Equation 4.8

$$\delta_m = \cos^{-1}\left\{\frac{a/\lambda_s - \sqrt{(a/\lambda_s)^2 + 8}}{4}\right\} \tag{4.8}$$

The implementation of DTC should ensure that this limit is accounted for, or the algorithm would become unstable after the maximum torque flux angle (a command in positive change in torque would produce increasingly more negative change in torque).

Taking these issues into account, the control action can be modified to stay in the region with positive slope in the torque-flux angle curve. The torque change can then be easily controlled by the change in flux angle. The stator voltage equation in the stationary reference frame can be expressed as Equation 4.9.

$$\lambda_{\alpha\beta} = \int \left(V_{\alpha\beta} - R_s i_{\alpha\beta}\right) dt \tag{4.9}$$

By neglecting the stator resistance, the change in flux can be estimated as the applied voltage. In addition, Equation 4.6 and Figure 4.10 show that the electromagnetic torque can be controlled by controlling the amplitude and angle of the flux. Under these conditions, the switching table presented in Section 1.3.2 is valid.

4.3.1.1. Flux Limit Interpretation

The concepts of DTC are useful in the understanding of the flux limit of the machine with increasing speed and the need for flux weakening. Considering a counter-clockwise rotation of the rotor and stator flux in the αβ-stationary reference frame, and under the assumption of negligible stator resistance Eq. 4.9 can be rewritten as Equation 4.10

$$d\lambda_{\alpha\beta} = V_{\alpha\beta} dt \tag{4.10}$$

In order to maintain a certain operating point, the angle between rotor and stator flux must be kept constant i.e. the stator flux and rotor rotational speeds must fulfill Equation 4.11

$$\left(\frac{d\delta}{dt}\right)_{max} \geq \omega_r \tag{4.11}$$

Considering Eq. 4.11, the maximum change in flux in the stator reference frame can be approximated by a circle centered at the end of the flux vector and with radius equal to the maximum available voltage, as illustrated by Figure 4.11.

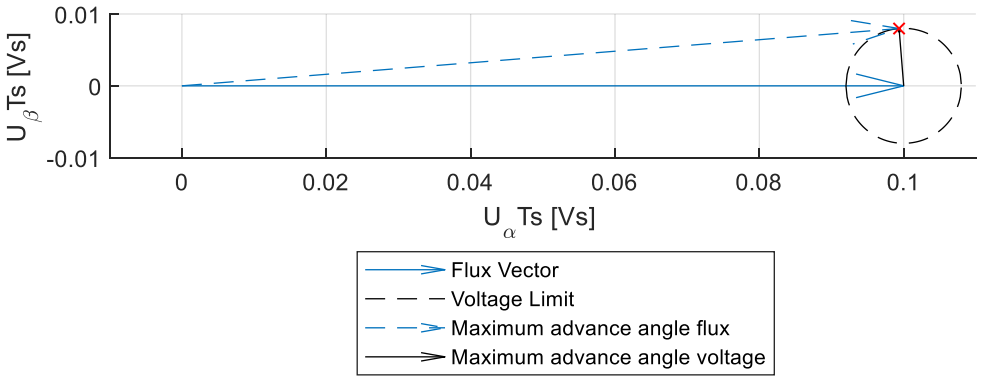

Figure 4.11: Maximum change in flux angle in the stator reference frame for one sampling period.

The maximum-advance-angle voltage is perpendicular to the maximum-advance-angle flux, and so the figure can be described by Equation 4.12. Moreover, for a sufficiently small angle, this expression can approximate the angle itself. Considering the differential and substituting Eq. 4.11, the limit for the flux can be found as Equation 4.13

$$(\Delta\delta)_{max} \approx \tan(\Delta\delta)_{max} = \frac{V_{lim}\Delta t}{\lambda_s} \tag{4.12}$$

$$\frac{V_{lim}}{\lambda_s} \approx \left(\frac{d\delta}{dt}\right)_{max} \geq \omega_r \tag{4.13}$$

Therefore, the flux is limited by the voltage in terms of the maximum advance angle that can be achieved in order to maintain the stator flux at a constant lead or lag from the stator. The voltage limit can then be interpreted according to the modulation strategy considered. However, if the hexagon limit or six step operation is used it must be considered that the voltage limit for maximum advance angle changes according to the flux position.

4.3.2. DTC Implementation

The simulation was implemented in the discrete domain with sample time T_s = 10 µs. The switching frequency of the inverter in the testbench is 10 kHz, meaning this sampling time is one order of magnitude smaller than the expected by the testbench. Moreover, DTC provides no fixed switching frequency. Therefore, the simulation is an approximation assuming that the resolution provided by a small sample time is enough to choose the voltage vectors as the DTC controller would.

However, this increases the bandwidth of the controller in simulation beyond the physical capabilities of the inverter. The solutions achieved in this simulation would need to be tested

again with a smaller sampling time, but the initial purpose of this was to gain a better understanding of the behavior of the DTC algorithm.

The machine model was implemented in the dq-reference frame, assuming perfect initial alignment between rotor and the abc-reference frame. No flux or current observers were implemented, assuming perfect estimation of flux amplitude and angle, currents and torque.

The DTC algorithm implementation is shown in Figure 4.12 and includes:

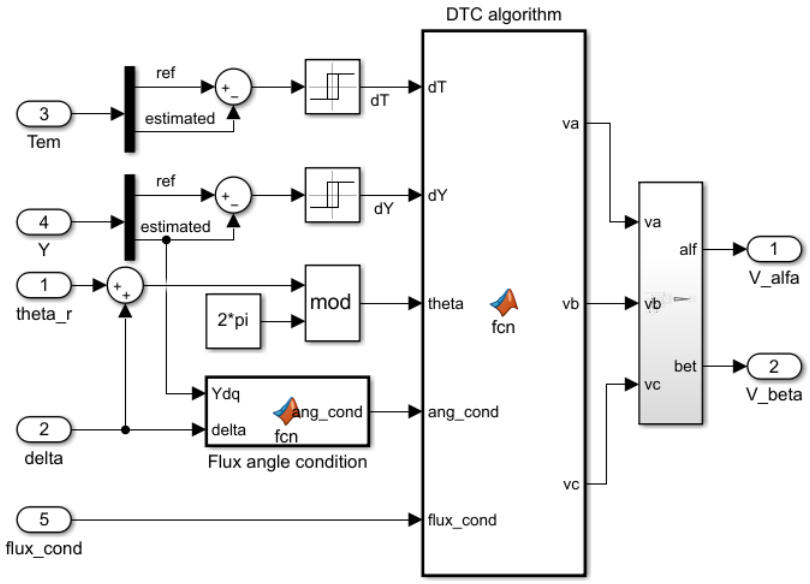

Figure 4.12: DTC implementation in simulation.

- Switching table as given by Table 1.1
- Hysteresis comparators for torque and flux control
- Flux angle (δ) condition: modification of the torque condition for accessing the switching table depending on the flux magnitude and angle. The evaluation of the sign of the differential of toque with respect to the flux angle as Equation 4.14

$$\left(\frac{dT_{em}}{d\delta}\right)_{sign} = sign\left(\lambda_{pm} L_q \cos\delta + \lambda_s (L_d - L_q)\cos 2\delta\right) \tag{4.14}$$

  - If $\left(\frac{dT_{em}}{d\delta}\right)_{sign}$ is positive no action is taken
  - If $\left(\frac{dT_{em}}{d\delta}\right)_{sign}$ is negative:
    - If $\delta > \frac{\pi}{2}$: the operation is beyond the MTPF point, and the "torque command" is set to reduce the torque to return to the positive slope region,

        - If $\delta < \frac{\pi}{2}$: The operation must be near $\delta = 0$, with a high flux magnitude producing negative slope. The "torque condition" is set to increase the torque to operate in the positive slope region.
- Six-step operation: if the flux margin in the hysteresis comparator is too narrow, the operation cannot transition into six-step. To allow this, once the flux weakening is limiting the flux amplitude reference (*flux_cond = 1*), the upper limit is increased, and the lower limit is set to the reference flux. Moreover, instead of the hysteresis comparison, the flux and command is modified to choose the "preferred" voltages to achieve six-step. The flux limits are used to correct this operation when the flux is too high or too low (operation close to the middle of the hexagon and the vertexes). Instead of a hysteresis, the flux is 'nudged' in the appropriate direction only while it is outside the imposed limits. The implementation of this algorithm is done before accessing the switching table in the "DTC algorithm" block from Figure 4.12 shown in Appendix D Script D.1.

Several tests were performed in simulation to assess the behavior of the system. The response is analyzed in Figure 4.13, Figure 4.14 and Figure 4.15 in terms of the controlled variables transient as well as the torque and flux conditions (1 when the command is to increase), the Space Vector Modulation (SVM) voltage selection (according to Figure 1.7) and the flux vector position in the stationary reference frame.

4.3.2.1. Torque and Flux Transient Response

From standstill, a torque and flux step command were applied (600 Nm and 0.09 Vs respectively) while the speed increased from 0 to 500 rpm. The lower-right plot in Figure 4.13 shows the reference flux amplitude (continuous line), the hysteresis band (discontinuous line), the DTC algorithm sections boundaries (dash-dotted line) and the SVM vectors (black arrows). The algorithm is successful at achieving the torque command in a small time (1.2 ms), but the torque ripple is much higher than the desired hysteresis band (5 Nm). This is because the effect of flux amplitude in the airgap torque value is higher than the effect of flux angle. The flux reference is achieved even faster than the torque (0.4 ms), and the ripple is successfully kept within the desired band (0.002 Vs). This indicates that the DTC can achieve

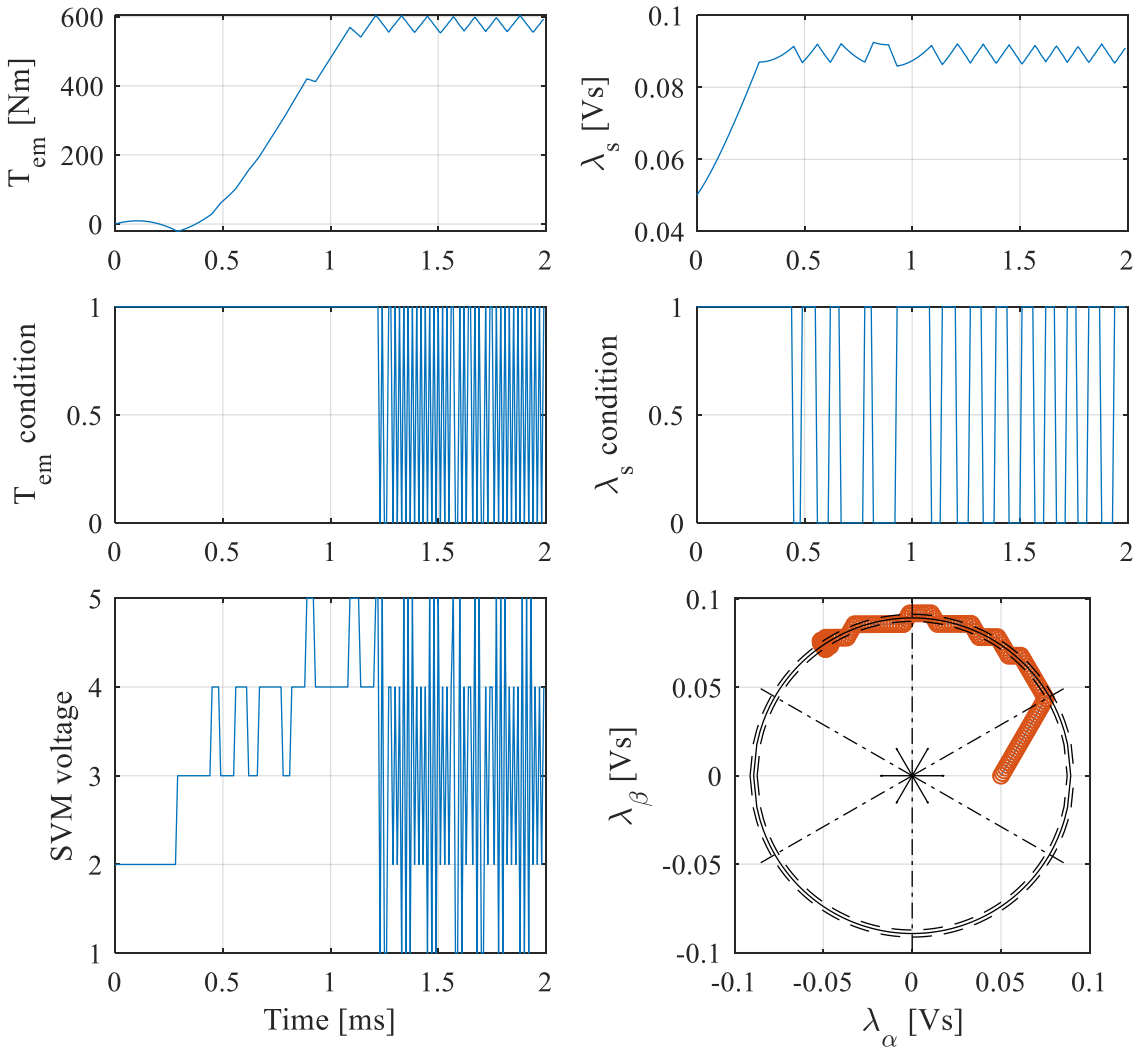

Figure 4.13: Simulation DTC transient response response to a step in torque (600 Nm) and flux (0.09 Vs) at low speed.

a very accurate control of the flux, and the torque control is inherently not prioritized by the algorithm.

4.3.2.2. Steady State Response

Figure 4.14 shows the response during a constant torque and flux command at 5000 rpm. It is seen again how the torque control is not very successful in dealing with flux amplitude changes (the torque does not always increase when the torque condition is 1), while the flux control maintains the value within the hysteresis band.

4.3.2.3. Six-Step Operation

The operation during high speed (17000 rpm) is shown in Figure 4.15. The points in which the torque condition is 0 are not a consequence of the hysteresis controller, but the flux angle

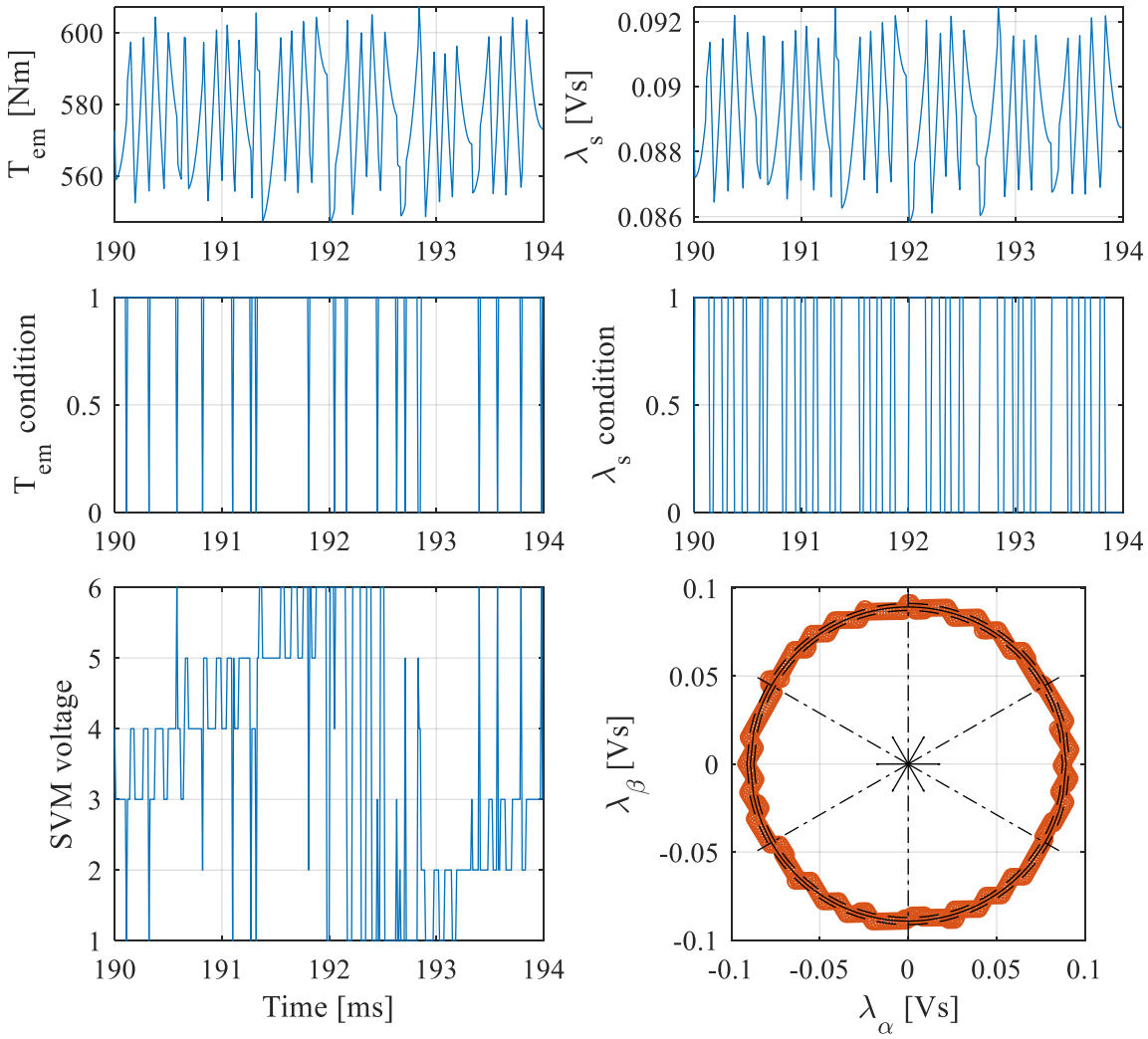

Figure 4.14: Simulation DTC steady state response at 4000 rpm for a constant torque (600 Nm) and flux (0.09 Vs) command.

condition system (see Section 4.3.2). The same is true for some instances in the stator flux condition and the six-step operation code. The operation is close to six-step but does not completely accomplish this, since some corrections are required to maintain the desired operation.

When compared to DB-DTFC operation for the same references, the DTC algorithm is able to achieve more torque. However, this is only due to the flux weakening reference generation using the linear limit, and the proposed DTC algorithm increasing this reference to achieve six-step. For higher flux references (within a margin), DB-DTFC can achieve higher torque with much lower ripple.

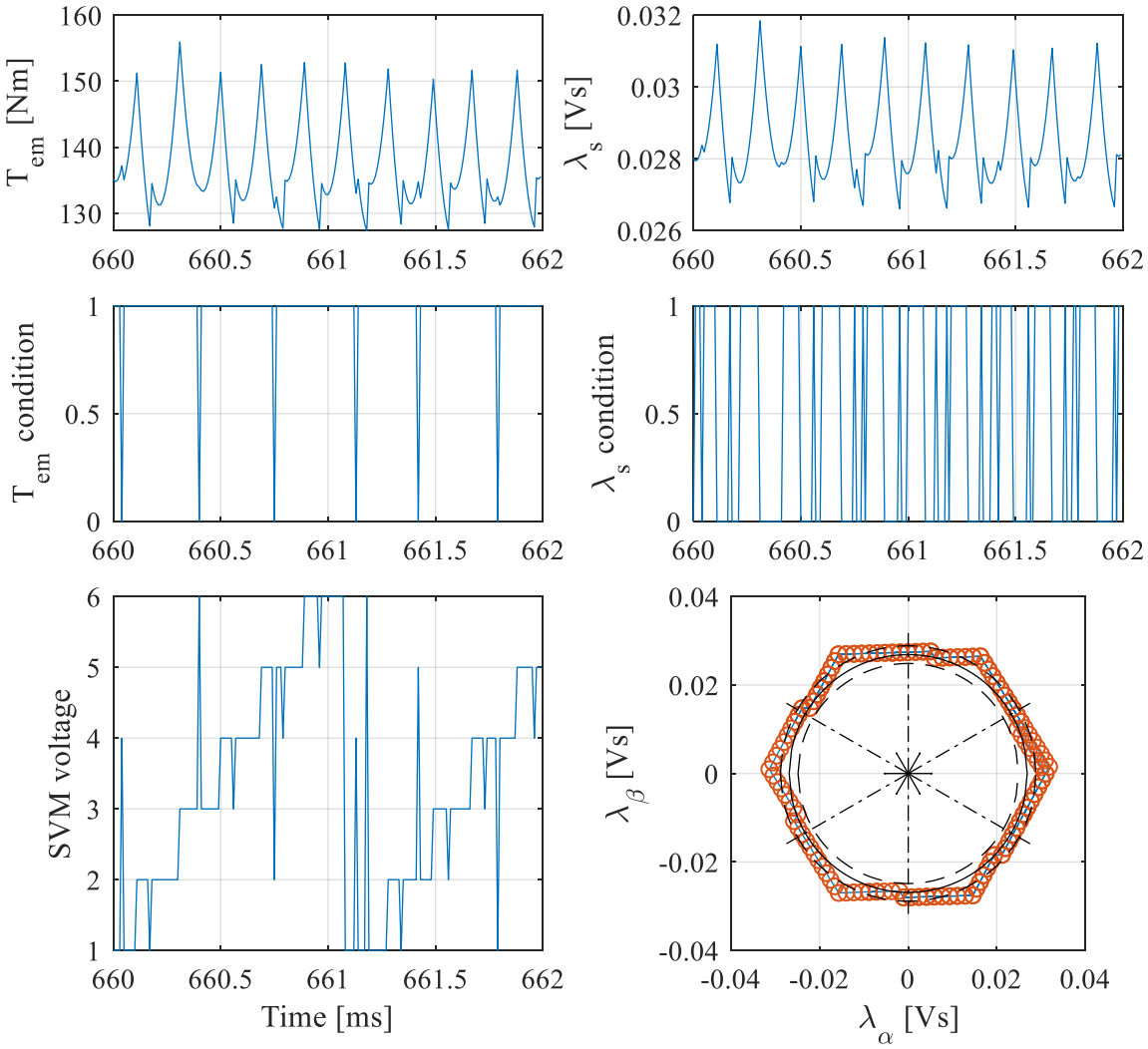

Figure 4.15: DTC steady state response in simulation at 17000 rpm for maximum torque command and flux weakening limited flux command.

In addition, the voltage references produced by each algorithm in open loop while the other was active were very different, making a transition between the two control strategies very challenging. These reasons and the inherent benefits of having a single control law motivated the design of a voltage selection algorithm emerging form the DB-DTFC algorithm, applying the ideas from DTC.

4.3.3. DB-DTFC Switching Table Algorithm

In [17] and [13] the notion of the DB-DTFC steady state geometries for null change in torque and flux was introduced. These geometries (for IM) divide the achievable voltage commands (voltage hexagon) if 4 regions according to Figure 4.16 [13].

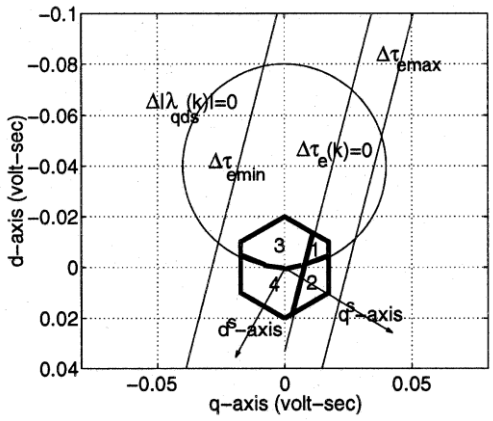

Figure 4.16: Graphical representation of DB-DTFC operating regions in terms of the null change in torque and flux geometries for steady state in an IM [13].

1. Increase torque, decrease flux
2. Increase torque, increase flux
3. Decrease torque, decrease flux
4. Decrease torque, increase flux

This paper proposed that alternate overmodulation could be used to select the most appropriate corner based on these conditions, arguing this would be equivalent to using standard DTC. This section explores this idea for its application to IPMSMs. The evaluation of each of the hexagon corners is done according to the criteria explained in the following subsections (graphically represented in Figure 4.17).

4.3.3.1. Comparison with the Null Differential Torque Line

The DB-DTFC algorithm produces a locus in the shape of a straight line for all the points in the dq-volt-seconds reference frame that would achieve a certain torque increment. Given that the slope of the null differential torque line is not dependent on the torque reference, and only on the operating point, by setting the torque reference to zero this provides a way of splitting the plane into two regions: above the line those commands that would increase torque and below those that would decrease it (Figure 4.17(a)).

It is then possible to evaluate the sign of the torque increment produced by each point in the plane based on the comparison of their projection in the q-axis following the differential torque line slope with the q-axis intercept of the null change in torque line (B'). This is done for the vertexes of the volt-second hexagon limit as shown in Equations 4.15 and 4.16

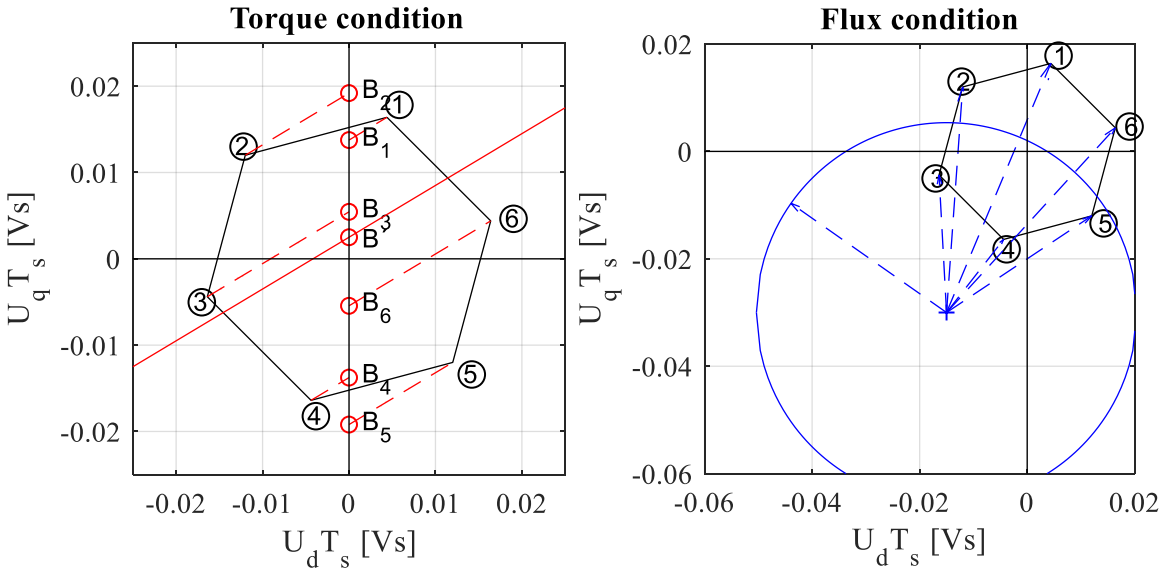

(a) (b)

Figure 4.17: Graphical representation of torque and flux conditions of six-step voltages based on DB-DTFC equations regions for an IPMSM. The geometries reptresented correspond to the null change in torque line (solid red (a)) and the null change in flux circle (solid blue (b)).

$$B_k = U_q Ts_k - U_d Ts_k M \tag{4.15}$$

$$\Delta T > 0 \; if \; and \; only \; if \; B_k > B' \tag{4.16}$$

4.3.3.1.1. Comparison with the Null Change in Flux Circle

The DB-DTFC algorithm produces a locus in the shape of a circle for all the points in the dq volt-seconds reference frame that would achieve a certain flux. Given that the center of the flux circle is not dependent in the flux reference, this provides a way of splitting the plane into two regions, inside the circle with radius equal to the current value of the flux are points that would reduce it, and outside the circle are points that would increase it (Figure 4.17(b)).

It is then possible to evaluate the sign of the flux increment produced by each point in the plane based on the comparison of their distance to the flux circle center with the value of the current flux in the machine. This is done for the vertexes of the volt-second hexagon limit as shown in Equations 4.17 and 4.18

$$l_k = \sqrt{(U_d Ts_k + \lambda_{d1})^2 + \left(U_q Ts_k + \lambda_{q1}\right)^2} \tag{4.17}$$

$$\Delta\lambda > 0 \; if \; and \; only \; if \; l_k > \lambda_s \tag{4.18}$$

4.3.4. DB-DTFC Switching Table Implementation

The proposed algorithm was implemented with the DB-DTFC algorithm as Appendix D Script D.2, and tested in simulation in open loop simultaneously with DTC. The objective

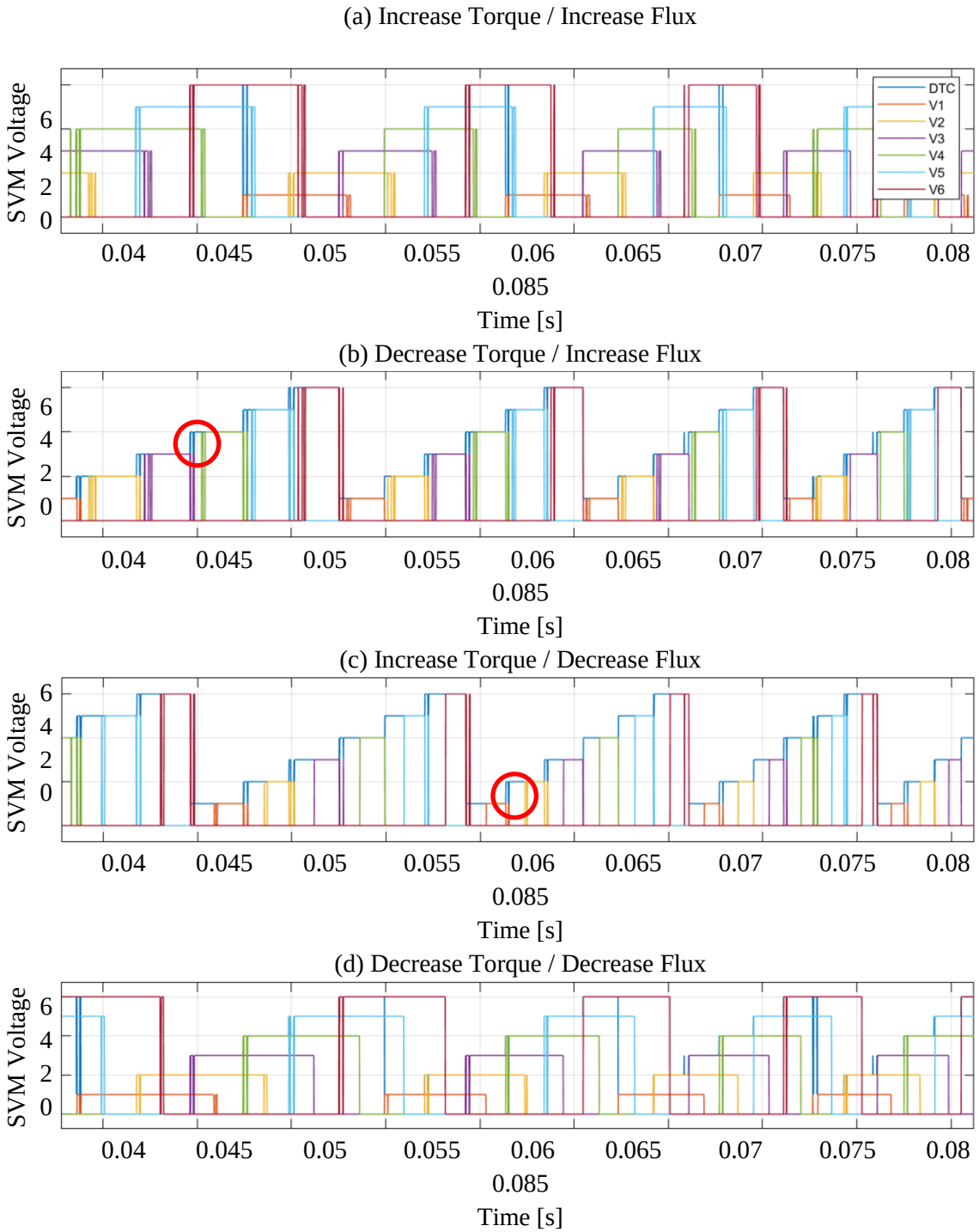

Figure 4.18: Open loop simulation comparison of the six-step voltage selection for the desired change in torque and flux by DTC and DB-DTFC switching table.

was to evaluate the voltage choice available to each algorithm to achieve each of the torque and flux configurations at each point in time. The results are shown in Figure 4.18.

The voltage choice for DTC is shown in Figure 4.18 as a single line in each of the plots in dark blue. The 'switching table' from the new algorithm is shown with each voltage vector independently. If the corner *k* of the voltage hexagon would achieve the desired response, its line has a value of *k*, if not it has a null value.

In a preliminary observation of the response, it can be said that both algorithms are at most times in agreement, which is signified by the overlapping of the new algorithm voltage choice on top of the DTC line (i.e. the new algorithm is validated for some operations). This is always the case in the configurations that increase or decrease at the same time both torque and flux (Figure 4.18 (a) and (d)). Moreover, in these cases it is rarely the case (for the time shown) that there is only one available option of voltage to achieve the desired response).

However, while at some instances the options are completely defined and some configurations have multiple voltage possibilities that achieve it, at other times the new algorithm cannot find a voltage that would produce the desired output. This can be detected by those points in time in which the DTC voltage option is not overlapped by a line from the new algorithm. Two of these instances were highlighted with red circles in Figure 4.18. This happens in the configurations that increase one of the variables while decreasing the other (Figure 4.18 (b) and (c)). This effect was studied for one of the problematic instants in and is shown in Figure 4.19.

In the figure, the geometries for null change in torque and flux, the hexagonal voltage limit and a scaled stator voltage vector are displayed for reference. Each six-step voltage is marked according to the effect on torque and flux change that the algorithms expect (small markers for the new algorithm and big for DTC).

For this case, the two algorithms differ on the effect of choosing vertex 5. While DTC would choose it as an option to increase torque, the new algorithm shows it would decrease it. This indicates that the new algorithm is more comprehensive that the DTC table, including other phenomena that reveal the real evolution of the system, or that the extra information provided by the new algorithm is not reliable. The first option is more likely, as this effect

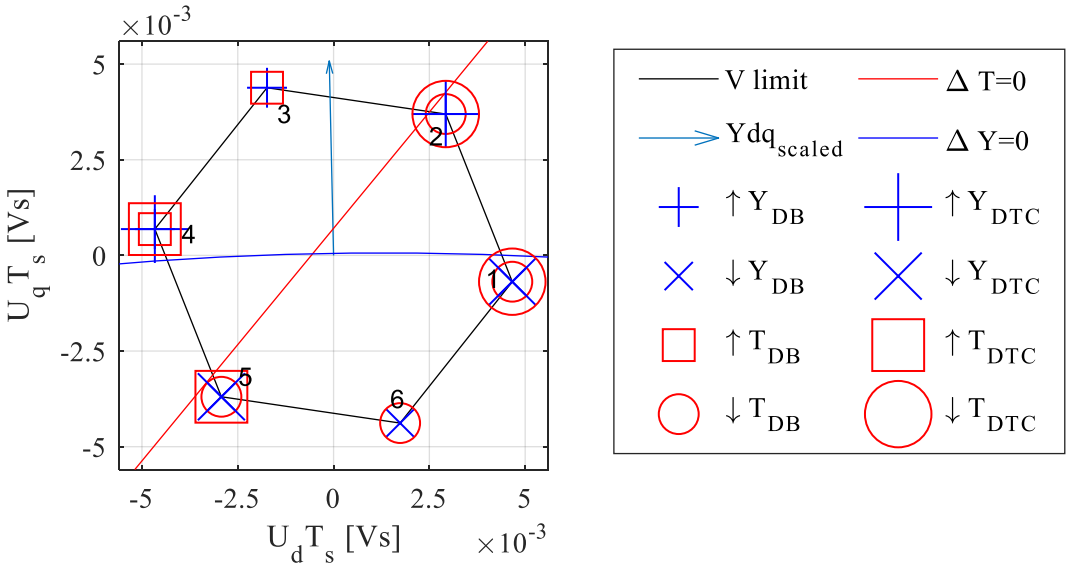

Figure 4.19: Comparison of the ffect of each six-step voltage on the flux and torque change accoridng DTC and DB-DTFC switching table in the dq-volt-second plane.

was already observed in the DTC implementation (increasing torque while decreasing flux is challenging for DTC).

Another interpretation of the figure is that the classic DTC could be thought of as a special case of the new algorithm for which:

- The line for null torque change passes through the origin and is parallel to the flux vector (for DTC the torque condition is based on the advance or delay of the flux vector).
- The circle for null change in flux is a line passing through the origin and perpendicular to the flux vector, with the center of the 'infinite circle' in the opposite direction to the flux vector.

It should also be noted that if the desired output is to decrease flux and increase torque, the new algorithm cannot produce an appropriate voltage. This phenomenon is worsened when operating at high speeds (particularly in the second flux-weakening region). In this region, the flux circle and differential torque line tend to be tangent, and they cut the hexagon very close to each other, leaving only the possibility of increasing or decreasing both flux and torque at the same time. Therefore, an algorithm prioritizing which of these alternatives should be chosen must be developed. On the other hand, for those conditions that offer

multiple possibilities to achieve the desired change, an algorithm that chooses between the options must be generated as well. This was implemented according to Figure 4.20.

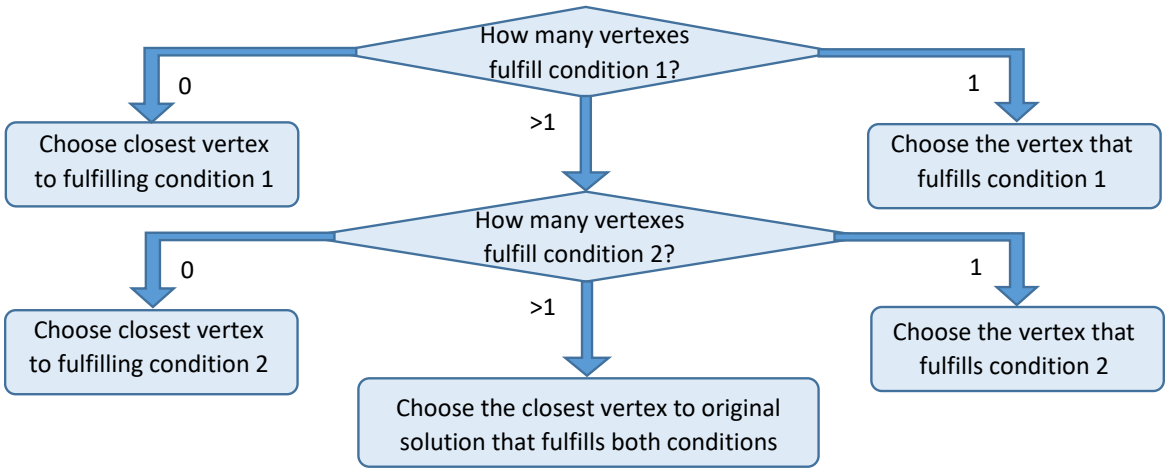

Figure 4.20: Voltage selection algorithm according to the conditions defined by the DB-DTFC swtiching table.

4.3.4.1. Torque Transient at Low Speed.

The algorithm was only found to be stable if the torque condition was prioritized. A simulation was performed at low speed (500 rpm) and a transient to an achievable steady state torque (400 Nm) and flux (0.08 Vs). The torque and flux transient in Figure 4.21 and some instances of the voltage selection process are displayed in Figure 4.21.

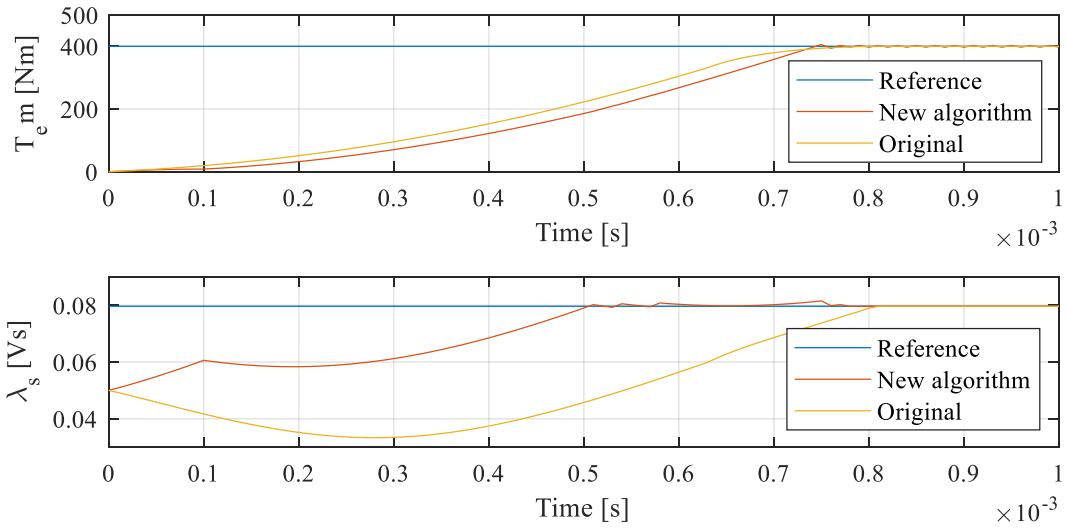

Figure 4.21: Simulation results for torque (400 Nm) and flux (0.08 Vs) transient at low speed (500 rpm) applying the DB-DTFC six-step voltage selection algorithm and original DB-DTFC.

The condition prioritizing algorithm is crucial during some operating points. For example, at t = 15ms (Figure 4.21 (b)) there is no voltage that can achieve the desired increase in both torque and flux, and voltage 3 is chosen prioritizing the torque change.

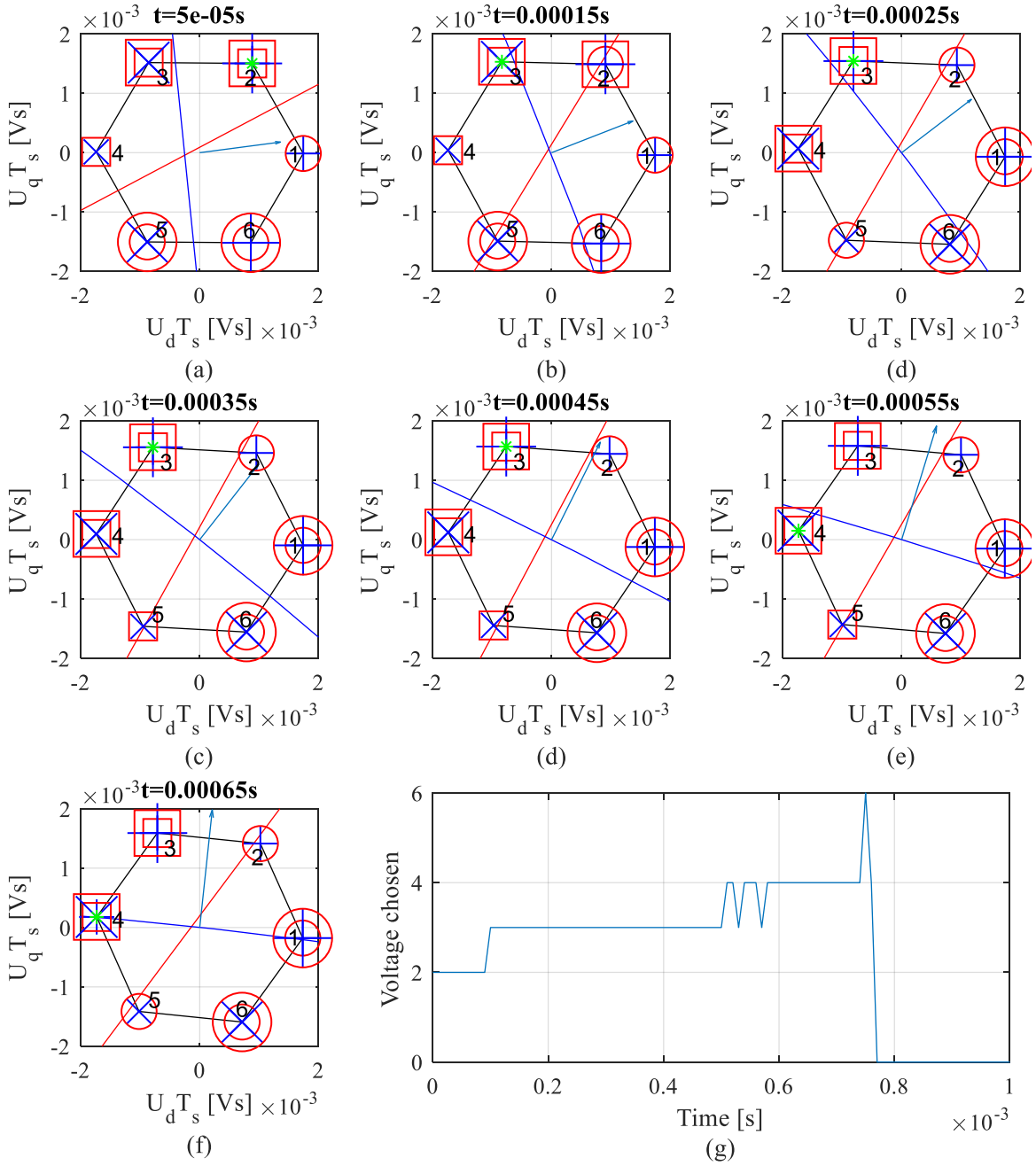

Figure 4.22: Voltage selection in the dq-volt-second plane for torque (400 Nm) and flux (0.08 Vs) transient at low speed (500 rpm) applying the DB-DTFC six-step voltage selection algorithm prioritizing the torque condition

The voltage selection process is noisy at times (Figure 4.21 (g) around 0.55ms) due to the flux reaching the reference, and after the steady state is achieved, the new algorithm exhibits an oscillatory behavior that is not observed in the original algorithm. Despite having prioritized the torque condition over the flux, the only benefits observed are in the flux transient which can achieve the reference 40% faster than the original algorithm.

4.3.4.2. Torque Capabilities Over the Speed Range

This algorithm was unsuccessful to achieve high performance operation with increasing speed, and the torque dropped when the flux weakening region starts. For testing during the whole speed range, the voltage selection was modified to select the closest vertex to the original reference if it lied outside the voltage hexagon. The results of comparing this method to the phase conservation method in simulation are shown in Figure 4.23. Multiple simulations were performed increasing the flux limit as Equation 4.19

$$\lambda^{ref}{}_{max} = \frac{M_{max} V_{dc}}{\omega_r \sqrt{6}} \tag{4.19}$$

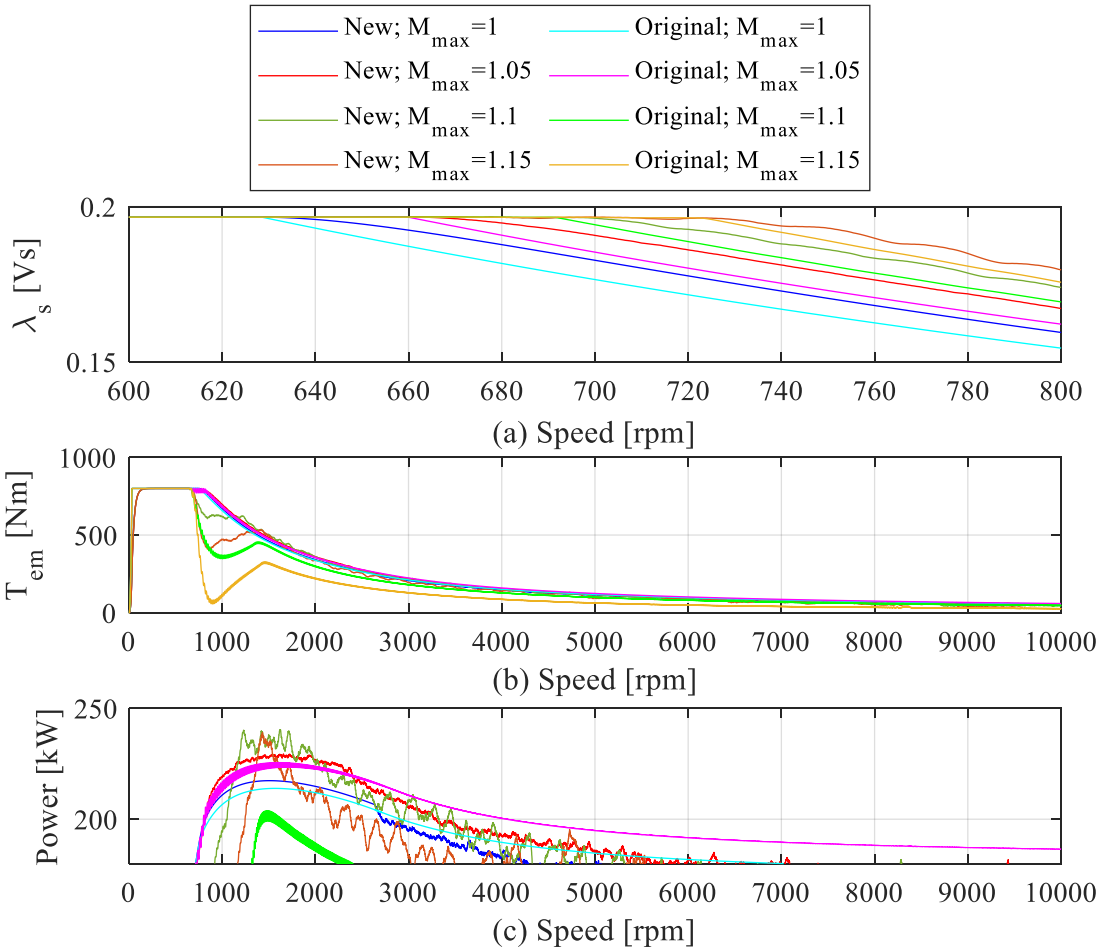

Figure 4.23: Simulation results for flux, torque and power maximum performance applying the DB-DTFC six-step voltage selection algorithm and original DB-DTFC.

The importance of the flux weakening algorithm is observed around base speed in the torque performance. When the flux limit is set above the achievable value by the algorithm, the torque drops during a certain speed range. This sudden loss of torque capabilities is

recovered when the machine rotates faster, but the torque performance remains below the maximum achievable (see yellow line in Figure 4.23(b)). The maximum power is achieved by the new algorithm with a maximum modulation index of 1.1 and 1.05 (Figure 4.23(c)). The new algorithm achieves higher flux than the original one, but this does not translate into higher torque (for the cases in which both algorithms use the same limit). The maximum performance at higher speed is achieved by the old algorithm with a maximum modulation index of 1.05 (magenta line in Figure 4.23(c)).

4.4. Experimental Results

Most of the following tests were performed by commanding the maximum torque (with the external current limit acting). The DC bus voltage was 200 V and the maximum allowed current 200 A (rms). All overmodulation techniques were tested, with a gain on the flux reference of 0.95 over the maximum achievable modulation index as expressed in Equation 4.20

$$\lambda^{ref}{}_{max} = k_{margin} M_{max} \frac{V_{dc}}{\omega_e \sqrt{6}} \tag{4.20}$$

The maximum modulation index was chosen according to Table 4.1.

	Amplitude modification for Phase conservation	Angle skipping algorithm	Six-step selection condition	Maximum Modulation index saturation	Legend indicator
Original overmodulation	-	-	-	1	OrigM100
	-	-	-	1.05	OrigM105
	-	-	-	1.15	OrigM115
Hexagonal Limit	0 – Not	0 - Not	-	1.2	HexaM0A0
	1 - Yes	0 - Not	-		HexaM1A0
	1 - Yes	1 - Yes	-		HexaM1A1
DB-DTFC six-step voltage selection	0 - Not	0 – Not	0 – Original solution		SixStepM0C0
	0 - Not		1 – Torque priority		SixStepM0C1
	1 - Yes		0 – Original solution		SixStepM1C0
DTC	-	-	-		DTC

Table 4.1: Algorithms and characteristics tested experimentally.

The “Original overmodulation” algorithms achieve overmodulation by an adaptation of the duty signals as seen in 4.2.3. The ‘M’ value in the legend indicator of these algorithms refers to the maximum modulation index allowed. The “Hexagonal limit” algorithms saturate the voltage reference to the estimated hexagonal limit based on measured dc bus voltage and rotor angle information with the phase conservation method (Section 4.2.1). In addition to this, an amplitude adaptation (M) and angle adaptation (A) where implemented and activated as indicated by the experiment name (1 for active, 0 for deactivated). The angle adaptation method was described in Section 4.2.2. The “DB-DTFC six-step voltage selection” algorithms where described in Section 4.3.3. The six-step selection condition is only applied if the reference lies outside the voltage hexagon and is done in two ways: a value of 0 corresponds to the choice of the hexagon corner closest to the original solution and a value of 1 corresponds to the prioritization of the torque condition. As with the previous algorithms, “M0” or “M1” in the legend indicator corresponds to the de/activation of the amplitude adaptation for the phase conservation.

4.4.1. Response Throughout the Speed Range

The performance of the algorithms for a maximum torque command and speed increasing from 500 to 6000 rpm is displayed in Figure 4.24. The low speed response of the systems is identical except for the DTC algorithms (seen in black) which produces lower torque (although higher flux) and fail to go above base speed. The fact that the flux achieved is higher may be critical to the eventual failure of this algorithm, as it was observed in simulation and experiments that all these algorithms inherently prioritize following the flux reference to the torque reference.

A similar less critical failure is seen in some of the algorithms saturating the voltage reference to the estimated hexagonal limit (‘seen in green) when base speed is reached. The high flux reference set prevents the system from achieving the maximum torque, although this effect reduces with increasing speed and above 5000 rpm this effect is overcome. This same effect was observed in simulation and reinforces the need for a more accurate and dynamic flux weakening limit generation based on the voltage limit.

A more detailed view around base speed is useful to compare the rest of the algorithms and is shown in terms of power and flux in Figure 4.24 (b) and (c). In the flux response it can

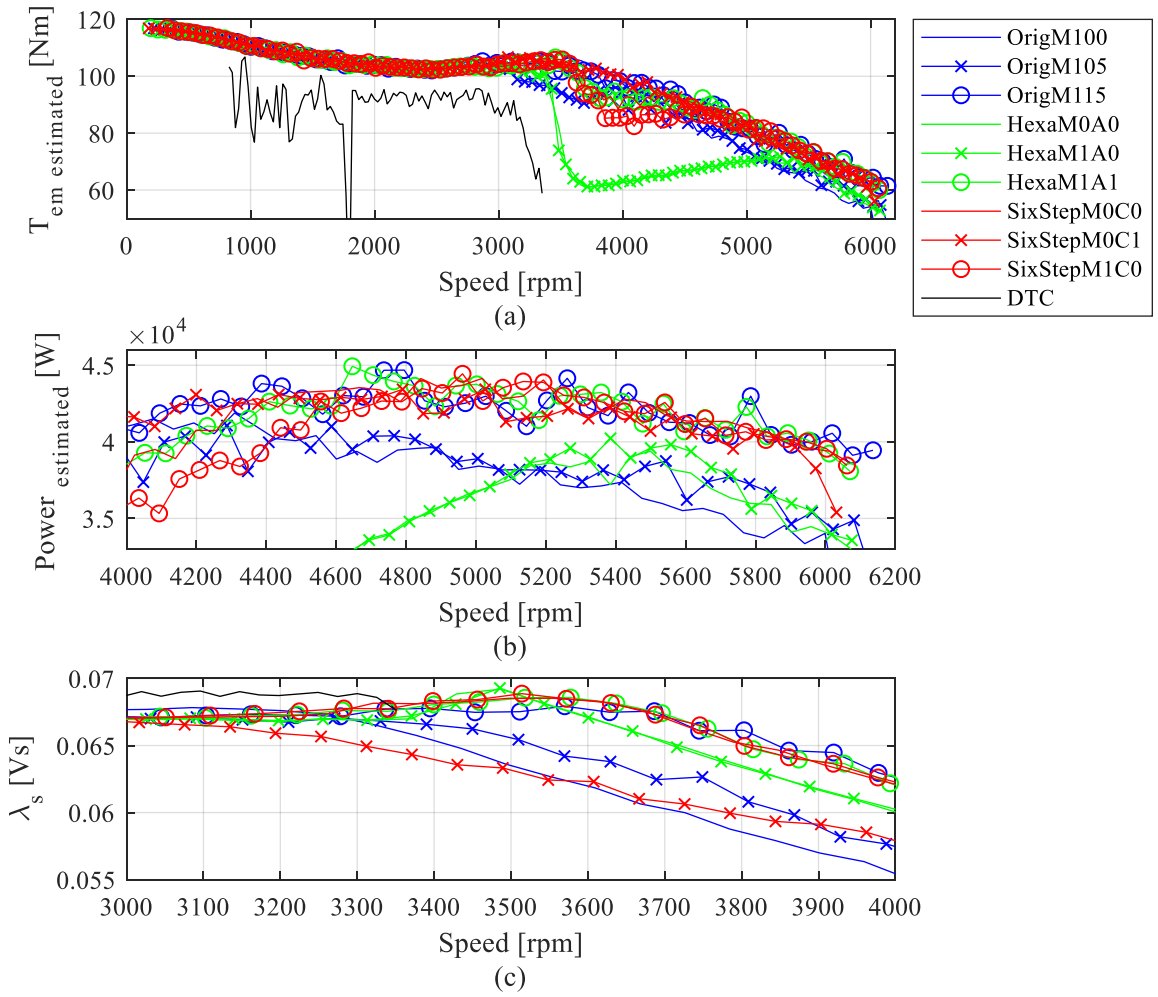

Figure 4.24: Experimental results for torque, power and flux performance for the overmodulation strategies implemented for maximum torque command from 500 to 6000 rpm.

be seen how the flux achieved by the voltage selection and hexagon limit algorithms is very high (due to the modulation index limit set in Table 4.1). This indicates, as mentioned before, that the flux reference is prioritized inherently by the DB-DTFC algorithm.

A similar response as with the hexagon saturated algorithms is observed to a lower degree in the 'OrigM105', 'HexaM1A1', 'SixstepM0C0' and 'SixstepM1C0', in which the torque is reduced around base speed. In this range (3000 to 4000 rpm), the biggest torque production corresponds to the original algorithm with the maximum modulation index saturation. However, the maximum power point is achieved later, between 4500 and 5000 rpm (Figure 4.24 (c)), and in this range the new algorithms are as capable as that strategy, and superior to the linear limit one (with up to 13% increase in power). The algorithm "SixstepM0C1"

produced a good response in this test but exhibited some instability during some other experiments, so it was neglected for some of the following investigations.

The test was repeated for the best options and a bigger speed range, and the results are shown in Figure 4.25. The algorithm that performs the best during the whole speed range is the duty saturation algorithm allowing maximum overmodulation ("OrigM115"), followed by the angle skipping algorithm ("HexaM1A1") and the voltage selection algorithm ("SixStepM0C0"). These two algorithms produce the same response, which is consistent with their operation principles.

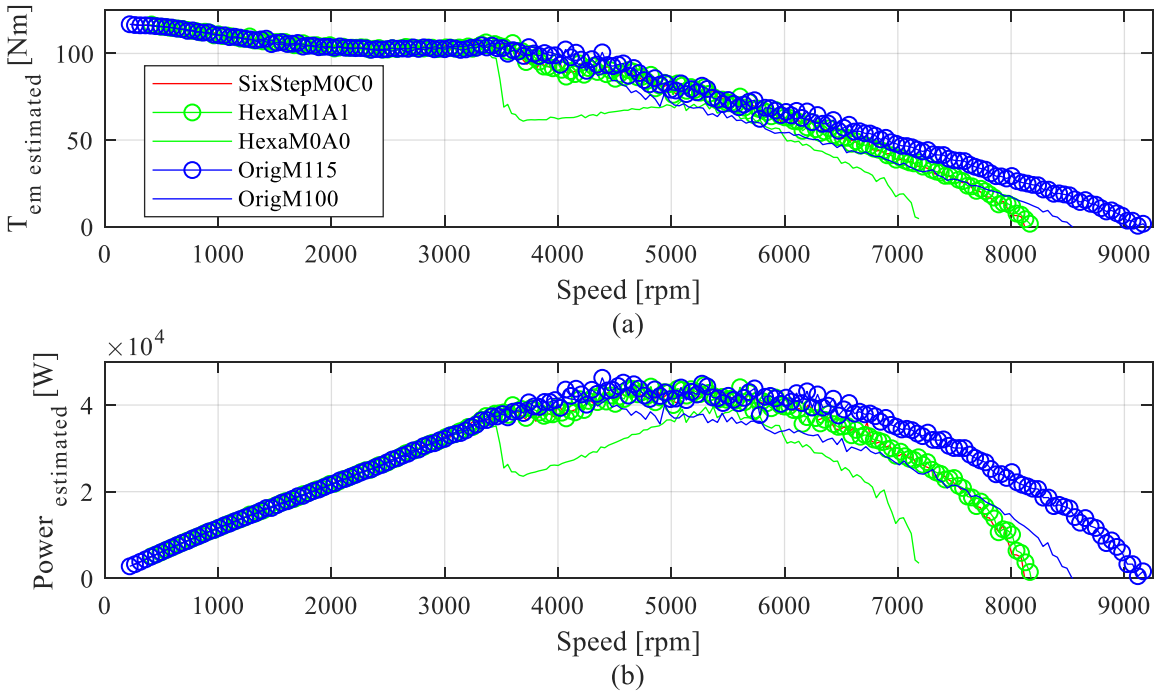

Figure 4.25: Experimental results for extended speed range torque and power performance of most succesful overmodulation strategies implemented

4.4.2. Testing of the Effect of Flux Reference Limit

An incorrect flux weakening limit for the flux weakening operation degrades the torque performance around base speed. To test the operation of the implemented strategies and avoid this issue, a test was performed by varying the maximum voltage for the flux limit calculation as Equation 4.21

$$\lambda^{ref}{}_{max} = \frac{V_{max}}{\omega_e} \tag{4.21}$$

The results are shown in Figure 4.26. The torque degradation for a voltage limit bigger than the achievable one can be observed in some of the experiments (most notable in "OrigM100" and "HexaM0A0" for Vmax = 85 and 90 V, which are the strategies that can achieve the lowest modulation index). The best performance was found with the duty saturation method.

More tests with varying the k_{max} value from Equation 4.21 were performed achieving similar results and can be seen in Appendix D, in addition to other representations of the results in Figure 4.26 for easier assessment.

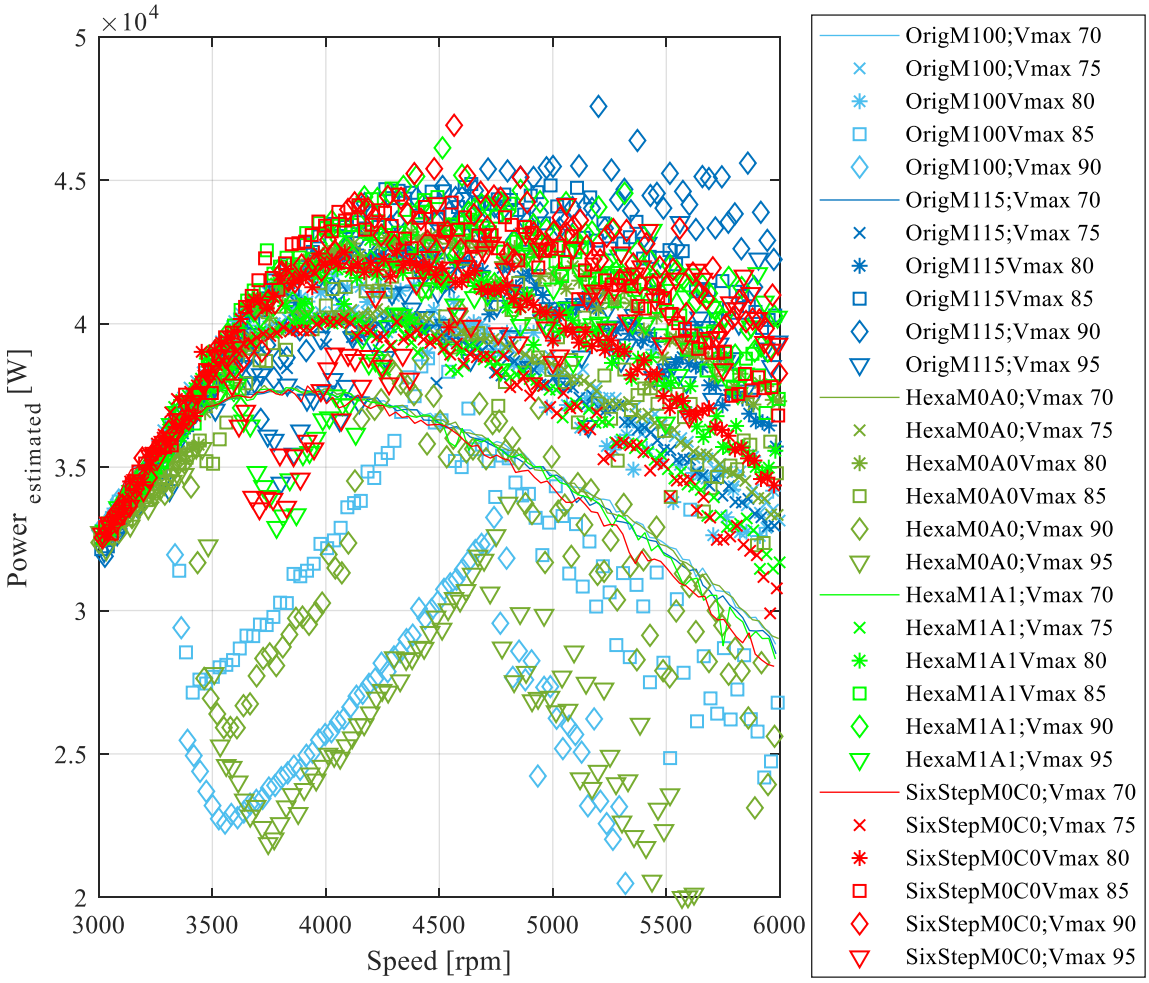

Figure 4.26: Experimental results for overmodulation strategies around the maximum power operation for different maximum voltage consideration in the flux weakening limit.

The conclusion from these tests was that the duty saturation method ("OrigM115") provides the best use of the inverter voltage, achieving high values of flux without compromising the torque performance. A screenshot of the oscilloscope waveforms during

the maximum power operation with this configuration can be seen in Figure 4.27. The current waveform shape as well as the almost complete lack of switching demonstrates the operation is very close to six-step, although this condition is not fully achieved. However, the DC voltage control became ineffective towards the end of the project and this issue could not be solved in time to generate better results. The DC voltage presented low frequency high amplitude components that affected the operation of the algorithms implemented.

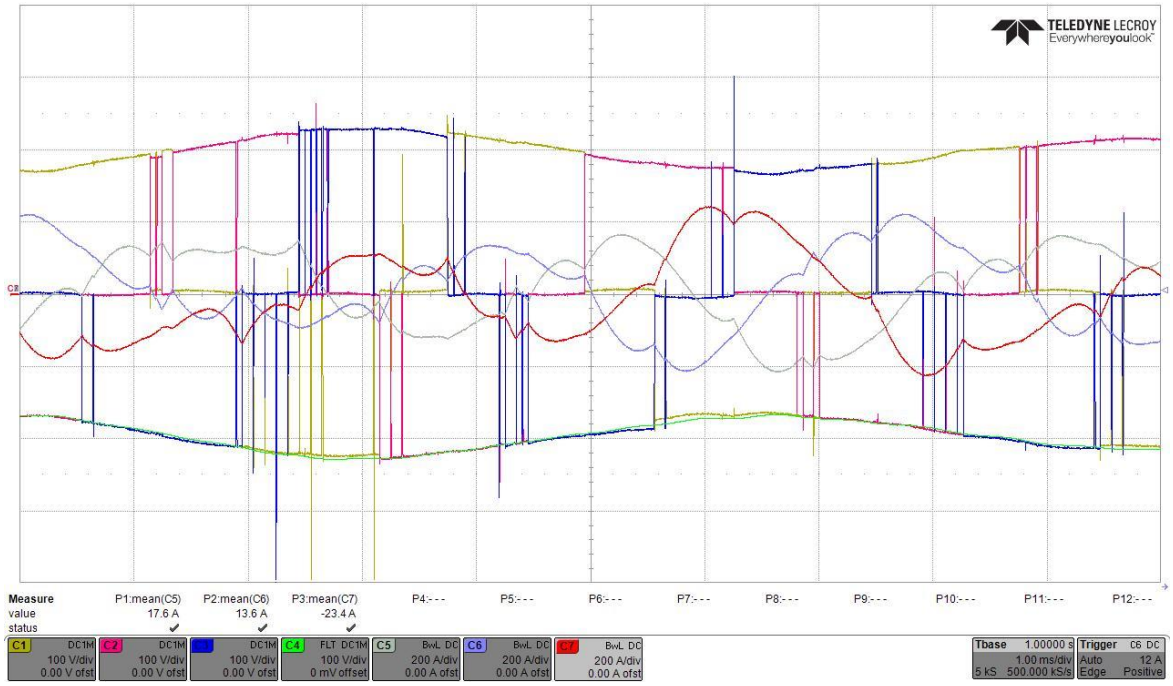

Figure 4.27: Oscilloscope waveforms achieved with the duty saturation method during six-step operation.

The voltage selection method as well as the hexagon saturation methods (phase conservation and angle removal) achieved similar waveforms, but the degradation of the torque performance was not solved by the end of this project. A critical requirement of these methods is accurate angle estimation, and the tests presented in Chapter III suggest this was a source of problems in the testbench used. Moreover, the flux reference should be adapted to bring about the six-step operation.

4.4.3. Testing of Dynamic Flux Weakening Limit Adaptation

Some attempts were made to design new algorithms that would improve the operation. The most successful of these was a dynamic adaptation of the flux weakening limit. The limit would ensure the linear operation for torque references below maximum even in the flux

weakening region. Without this kind of strategy, above base speed the flux command is very high and the operation would transition into overmodulation even if the machine is operating for partial loads. This ensures that the overmodulation strategies only act to accelerate transients and increase the torque and power performance of the drive when both the torque and flux references are limited by the current and voltage constraints respectively. A test showing the effects of this scheme for partial load operation can be seen in Figure 4.28. The scheme is successful in preventing the torque degradation to some degree, and completely removes it in the duty saturation algorithm for high maximum modulation index operation.

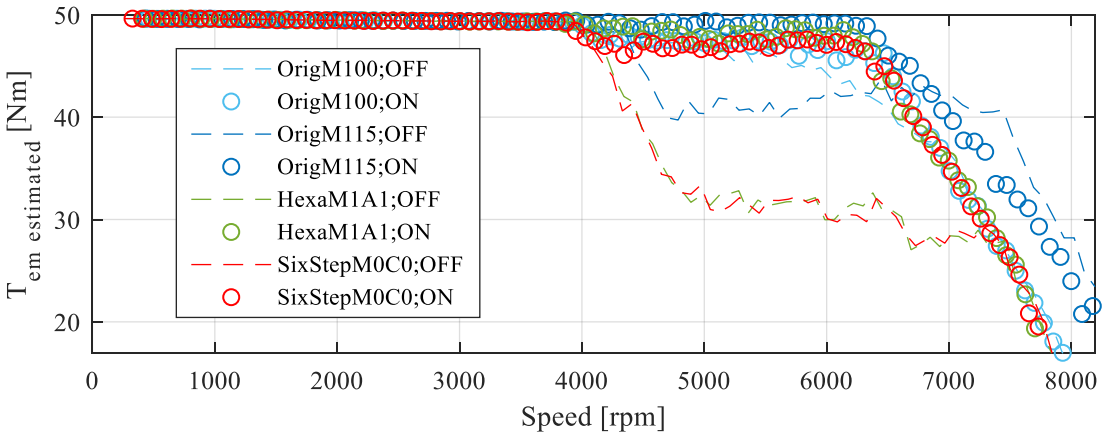

Figure 4.28: Experimental results for the application of a dynamic flux weakening limit adaptation for partial load operation (50 Nm) throughout the speed range.

4.5. Conclusions

- Common reference adaptation methods (amplitude conservation and phase conservation) were studied and implemented in simulation. The amplitude conservation method was found to be unsuitable for achieving a good response during overmodulation with DB-DTFC.
- An angle removal method was implemented in simulation to allow the transition between the phase conservation method to modulation indexes higher than 1.05 and eventually achieve six-step operation.
- The method originally implemented in the testbench was studied for comparison purposes, demonstrating it can achieve six-step operation in with less angle estimation sensitivity since the voltage hexagon position in the dq-reference frame is not required. The harmonic content according to the command modulation index

was studied showing lower harmonic injection for the original algorithm than the proposed method combining phase conservation with angle removal.

- A DTC algorithm was implemented in simulation accounting for the issues emerging from the use of the flux angle to control torque change. The flux command was also modified to allow the transition into six-step operation in the flux weakening region.
- The simulation results from the DTC implementation showed that the control of the torque independently to the flux amplitude is challenging, and the algorithm inherently prioritizes flux control both in transient and steady state operation.
- The implemented DTC algorithm was successful at achieving an operation close to six-step in simulation, but the challenges of a transition from DB-DTFC combined with the benefits of employing a single control law and the better response of DB-DTFC motivated the development of a new voltage selection algorithm.
- An algorithm was developed evaluating the change in torque and flux produced by each of the six-step voltages based on the information provided by the null change in torque line and the null change in torque circle form DB-DTFC. This algorithm was compared to the DTC voltage selection, concluding that DTC neglects important machine phenomena and does not produce the desired control output in some occasions.
- A voltage selection prioritization algorithm was developed based on the new switching table. Its operation was found to be successful at achieving overmodulation for high steps in torque and flux command at low speeds, but unable to maintain six-step operation in the flux weakening region. This algorithm was found to only improve flux response despite the voltage selection prioritized torque.
- The comparison of the torque performance of the phase conservation method with the new selecting the closest vertex to the reference showed that the new algorithm could achieve higher flux and maximum power, but the torque response was degraded at high speeds.

- The experimental results show that among the implemented strategies, the best method to achieve overmodulation with DB-DTFC was the duty saturation method, exhibiting an increase maximum power output (13%) and performance throughout the speed range.
- Accurate angle estimation is critical for good performance of the new algorithms implemented, and further improvement of these systems should include the generation of a non-constant flux reference generation for six-step operation.

Chapter V

Conclusions and Proposed Future Work

This thesis discussed the implementation of DB-DTFC in a testbench, studying the behaviour and potential problems with the provided setup, the application of overmodulation techniques to the DB-DTFC algorithm and the optimization of its operation in the MTPA and MTPF regions, demonstrating in the last one superior capabilities to CVC strategies. During this project, multiple insights were gained into the behaviour, capabilities and limitations of the studied algorithm, as well as promising future lines of research that could improve it.

5.1. Conclusions from the MTPA and MTPF Operation

- MTPA flux reference generation with reduced computational effort and parameter estimation error sensitivity was attempted. Several options were studied, and a promising algorithm was introduced which showed very little sensitivity to errors in permanent magnet flux estimation. That method was implemented experimentally, and it demonstrated better current utilization than the original strategy.
- The concept of SRC applied to DB-DTFC was studied as a MTPF strategy, demonstrating its capabilities analytically for perfect and incorrect parameter estimation errors. The conclusions from this process were confirmed with simulation results also providing insight into the machine transient behavior in the

second flux weakening region. Moreover, experimental results shown similar behavior and validated these results.

- The performance of SRC against parameter estimation errors was compared with two hybrid flux weakening strategies for CVC demonstrating much greater capabilities,

5.1.1. Future Work

- The geometries form DB-DTFC for the current limit should be considered to provide an MTPA flux reference generation algorithm without the need for precalculated approximations. Analogous concepts to the ones used during the study of SRC.
- The claim that the SRC steady state operation will remain unaffected by changes in real machine parameters in terms of flux operating point should be corroborated at more speeds and with experimental results.
- Other studies can be produced evaluating the limits of the SRC as an MTPF strategy, and more experimental results should validate the behaviour observed in this report.

5.2. Conclusions from the Testbench Implementation

- A set of programs was developed that successfully acquires, integrates, analyses and displays data from all the measurement and monitoring sources available in the testbench. This tool was used during the project to quickly asses the behaviour and tuning of the control parameters, as well as to validate the parameter estimation and to reveal potential problems with the testbench.
- An angle and amplitude mismatch between the command and measured voltage was detected by two independent tests.

5.2.1. Future work

- More detailed studies can be performed in the testbench to optimize the control parameters tuning as well as the performance of new features introduced.

- The programs developed can be used to conduct a more thorough investigation of the angle error, in order to identify the source of the problem and improve the control system to deal with these issues in future applications

5.3. Conclusions from the Overmodulation Strategies

- Multiple overmodulation strategies were studied and implemented both in simulation and experimentally, including reference adaptation techniques used in other control methods and the application of DTC concepts to create a new voltage selection algorithm for DB-DTFC six-step operation.
- DB-DTFC can operate in the linear voltage limit and overmodulation region through the phase conservation method with no degradation to the performance and no ancillary systems to the control (as anti-windup strategies). The limitations of this strategy motivated the move towards six-step operation to provide maximum utilization of the inverter voltage.
- The overmodulation techniques considered, with the exception of the duty saturation method, require accurate estimation of the voltage hexagon limit position in the dq-reference frame, and this is thought to be one of the main reasons they degraded the performance of the drive on some operating points. Moreover, they were implemented as a last step before sending the voltage command to the inverter, without providing reference adaptation schemes to account for the disruption of the original command voltage.
- The voltage selection algorithm proposed requires other ancillary systems to produce maximum performance operation. It was concluded that this is mainly due to the attempt to follow a constant flux reference during overmodulation instead of the command flux changing according to the voltage hexagon limit location.
- Quasi-six-step operation was achieved experimentally with the duty saturation method, improving the speed range, torque and power performance of the drive.

5.3.1. Future Work

- To achieve a good performance during six-step operation with DB-DTFC a non-constant reference adaptation should be generated, as the algorithm inherently prioritizes the flux response over the torque.
- While the dq-current plane provides an intuitive understanding of the steady state operation of the machine, the analysis of transient phenomena is better observed in the dq-volt-seconds plane. The analysis and improvement of DB-DTFC should include the geometries described in this thesis, and others (steady state current ellipse, transient current ellipse, maximum flux circle) as they provide intuitive insights into the machine behavior.
- The transient of the machine at low speeds could be improved through the consideration of the maximum flux circle (given by the flux weakening limit) or other geometries, and the voltage limit. The flux reference in DB-DTFC serves as a degree of freedom to control the operation of the machine, but it is possible that during transients this is degrading the capabilities of the drive.

References

[1] Z. Q. Zhu and D.Howe, «Electrical Machines and Drives for Electric, Hybrid, and Fuel Cell Vehicles,» *Proceedings of the IEEE,* vol. 95, nº 4, pp. 746-765, April 2007.

[2] Y. Guan, Z. Q. Zhu, I. A. A. Afinowi, J. C. Mipo and P. Farah, «Comparison between induction machine and interior permanent magnet machine for electric vehicle application,» *17th International Conference on Electrical Machines and Systems (ICEMS),* pp. 144-150, 2014.

[3] I. Bolvashenkov, J. Kammermann and H. Herzog, «Methodology for selecting electric traction motors and its application to vehicle propulsion systems,» *2016 International Symposium on Power Electronics, Electrical Drives, Automation and Motion (SPEEDAM),* pp. 1214-1219, 2016.

[4] G. Pellegrino, A. Vagati, P. Guglielmi and B. Boazzo, «Performance Comparison Between Surface-Mounted and Interior PM Motor Drives for Electric Vehicle Application,» *IEEE Transactions on Industrial Electronics,* vol. 59, nº 2, pp. 803-811, Feb. 2012.

[5] S.-K. Sul, Control of Electric Machine Drive Systems, "Basic Structure and Modeling of Electric Machines and Power Converters" and "Reference Frame Transformation and Transient State Analysis of ThreePhase AC Machines": IEEE, 2011.

[6] T. M. Jahns, G. B. Kliman, and T. W. Neumann, «Interior permanent magnet synchronous motors for adjustable-speed drives,» *IEEE Transactions on Industry Applications,* Vols. %1 de %2IA-22, nº 4, p. 738–747, Jul.-Aug. 1986.

[7] J. S. Lee, C. Choi, J. Seok and R. D. Lorenz, «Deadbeat-Direct Torque and Flux Control of Interior Permanent Magnet Synchronous Machines With Discrete Time Stator

Current and Stator Flux Linkage Observer,» *IEEE Transactions on Industry Applications,* vol. 47, nº 4, pp. 1749-1758, July-Aug. 2011.

[8] L. Zhong, M. F. Rahman, W. Y. Hu and K. W. Lim, «Analysis of direct torque control in permanent magnet synchronous motor drives,» *IEEE Transactions on Power Electronics,* vol. 12, nº 3, pp. 528-536, May 1997.

[9] M. F. Rahman, L. Zhong and Khiang Wee Lim, «A direct torque-controlled interior permanent magnet synchronous motor drive incorporating field weakening,» *IEEE Transactions on Industry Applications,* vol. 34, nº 6, pp. 1246-1253, Nov.-Dec. 1998.

[10] B. H. Kenny, «Deadbeat direct torque control of induction machines using self-sensing at low and zero speeds,» Ph.D. dissertation, Univ. Wisconsin, Madison, WI, 2001.

[11] H. E. Khatib, M. Peña, B. Grothmann, E. G. Gedlu and M. Saur, «Applying the Square-Root-Condition combined with DB-DTFC as a Flux Observer-Based Maximum Torque per Flux Strategy,» *2019 IEEE 10th International Symposium on Sensorless Control for Electrical Drives (SLED),* 2019.

[12] E. G. Gedlu, «Deadbeat Direct Torque and Flux Control (DB-DTFC) for Automotive Traction Machines Operating at Voltage and Current Limit,» Master Thesis for Erasmus Mundus Master Course in Sustainable Transportation and Electrical Power Systems, Universidad de Oviedo, September 2018.

[13] B. H. Kenny and R. D. Lorenz, «Stator- and rotor-flux-based deadbeat direct torque control of induction machines,» *IEEE Transactions on Industry Applications,* vol. 39, nº 4, pp. 1093-1101, July-Aug. 2003.

[14] SeHwan Kim and Jul-Ki Seok, «Discrete-time physical limits-based enhanced finite-settling-step direct torque and flux control for IPMSM drives,» *Energy Conversion Congress and Exposition (ECCE),* pp. 1794-1800, 2013.

[15] H. E. Khatib, «Flux Observer-Based Deadbeat Direct Torque and Flux Control for Interior Permanent Magnet Synchronous Machine in Automotive Traction Applications,» Master's Thesis executed at the Chair of Electrical Drive Systems and Power Electronics, Technische Universität München, April 2019.

[16] Wang, Yukai, et al., «Implementation issues and performance evaluation of deadbeatdirect torque and flux control drives,» *2015 IEEE International Electric Machines Drives Conference (IEMDC)*, 2015.

[17] B. H. Kenny and R. D. Lorenz, «Stator and rotor flux based deadbeat direct torque control of induction machines,» *2001 IEEE Industry Applications Conference, 36th IAS Annual Meeting*, vol. 1, pp. 133-139, 2001.

[18] Quang, Nguyen Phung, and Jörg-Andreas Dittrich, Vector control of three-phase AC machines Vol. 2., Berlin: Heidelberg: Springer, 2008.

[19] Y. Kwon, S. Kim and S. Sul, «Six-Step Operation of PMSM With Instantaneous Current Control,» *IEEE Transactions on Industry Applications*, vol. 50, nº 4, pp. 2614-2625, July-Aug. 2014.

[20] Giovanni Griva, Thomas G. Habetler, Francesco Profumo and Michele Pastorelli, «Performance Evaluation of a Direct Torque Controlled Drive in the Continuous PWM-Square Wave Transition Region,» *IEEE Transactions on Power Electronics*, vol. 10, nº 4, pp. 464-471, July 1995.

Appendix A: Analytical Demonstration of the Equivalence Between MTPF and SRC applied to DB-DTFC

1. General equation for DB-DTFC differential torque line

$$V_{qs}(k)T_s = V_{ds}(k)T_s M_D + B_D$$

2. General equation for DB-DTFC flux circle

$$\lambda_s^{*2} = (V_{ds}(k)T_s + \lambda_{ds1})^2 + \left(V_{qs}(k)T_s + \lambda_{qs1}\right)^2$$

$$\lambda_{ds1} = -R_s i_{ds}(k)T_s + \omega_r(k)T_s\lambda_{qs}(k) + \lambda_{ds}(k)$$

$$\lambda_{qs1} = -R_s i_{qs}(k)T_s - \omega_r(k)T_s\lambda_{ds}(k) + \lambda_{qs}(k)$$

3. Voltage solution combining (1) and (2)

$$a(V_{ds}(k)T_s)^2 + bV_{ds}(k)T_s + c = 0$$

$$a = 1 + {M_D}^2$$

$$b = 2(M_D\left(B_D + \lambda_{qs1}\right) + \lambda_{ds1})$$

$$c = \left(B_D + \lambda_{qs1}\right)^2 + {\lambda_{ds1}}^2 - \lambda_s^{*2}$$

$$V_{ds}(k)T_s = \frac{-b \pm \sqrt{b^2 - 4ac}}{2a}$$

4. Square-root-condition applied to the equation above

$$b^2 - 4ac \geq 0 \Rightarrow$$

$$\Rightarrow 4\left(M_D\left(B_D + \lambda_{qs1}\right) + \lambda_{ds1}\right)^2 - 4\left(1 + {M_D}^2\right)\left(\left(B_D + \lambda_{qs1}\right)^2 + {\lambda_{ds1}}^2 - \lambda_s^{*2}\right) \geq 0 \Rightarrow$$

$$\Rightarrow {M_D}^2\left(B_D+\lambda_{qs1}\right)^2+2M_D\left(B_D+\lambda_{qs1}\right)\lambda_{ds1}+{\lambda_{ds1}}^2$$

$$-{M_D}^2\left(\left(B_D+\lambda_{qs1}\right)^2+{\lambda_{ds1}}^2-\lambda_s^{*2}\right)$$

$$-\left(B_D+\lambda_{qs1}\right)^2-{\lambda_{ds1}}^2+\lambda_s^{*2}\geq 0\Rightarrow$$

$$\Rightarrow 2M_D\left(B_D+\lambda_{qs1}\right)\lambda_{ds1}-{M_D}^2\left({\lambda_{ds1}}^2-\lambda_s^{*2}\right)-\left(B_D+\lambda_{qs1}\right)^2+\lambda_s^{*2}\Rightarrow$$

$$\Rightarrow -\left(\left(B_D+\lambda_{qs1}\right)-M_D\lambda_{ds1}\right)^2+{M_D}^2\lambda_s^{*2}+\lambda_s^{*2}\geq 0\Rightarrow$$

$$\boxed{\Rightarrow \left(\left(B_D+\lambda_{qs1}\right)-M_D\lambda_{ds1}\right)^2\leq \lambda_s^{*2}(1+{M_D}^2)}$$

5. Rewriting of the DB-DTFC differential torque line terms for steady state

$$\boxed{M_D=\frac{-\left(L_d-L_q\right)\lambda_{qs}(k)}{\left(L_d-L_q\right)\lambda_{ds}(k)+L_q\lambda_{pm}}}$$

$$\boxed{B_D=\cancel{B_{D\,\Delta T_{em}}}+B_{D\,\omega}+B_{D\,R_s}}$$

$$B_{D\,\omega}=\frac{L_dL_q}{\left(L_d-L_q\right)\lambda_{ds}(k)+L_q\lambda_{pm}}$$

$$\left[\frac{-\omega_r(k)T_s}{L_dL_q}\left(\left(L_q-L_d\right)\left(\lambda_{ds}(k)^2-\lambda_{qs}(k)^2\right)-L_q\lambda_{pm}\lambda_{ds}(k)\right)\right]=$$

$$=\frac{\omega_r(k)T_s}{\left(L_d-L_q\right)\lambda_{ds}(k)+L_q\lambda_{pm}}\left(\lambda_{ds}(k)\left(\lambda_{ds}(k)\left(L_d-L_q\right)+L_q\lambda_{pm}\right)-\lambda_{qs}(k)^2\left(L_d-L_q\right)\right)$$

$$=$$

$$=\omega_r(k)T_s\left(\lambda_{ds}(k)-\lambda_{qs}(k)\frac{\left(L_d-L_q\right)\lambda_{qs}(k)}{\left(L_d-L_q\right)\lambda_{ds}(k)+L_q\lambda_{pm}}\right)\Rightarrow$$

$$\boxed{\Rightarrow B_{D\,\omega}=\omega_r(k)T_s\left(\lambda_{ds}(k)+M_D\lambda_{qs}(k)\right)}$$

$$B_{D\,R_s}=\frac{L_dL_q}{\left(L_d-L_q\right)\lambda_{ds}(k)+L_q\lambda_{pm}}*\left[-\frac{R_sT_s\lambda_{qs}(k)}{{L_d}^2{L_q}^2}\left(\left({L_q}^2-{L_d}^2\right)\lambda_{ds}(k)-{L_q}^2\lambda_{pm}\right)\right]=$$

$$= \frac{R_s T_s \lambda_{qs}(k) \Big/ L_d L_q}{(L_d - L_q)\lambda_{ds}(k) + L_q \lambda_{pm}} \Big(({L_d}^2 - {L_q}^2)\lambda_{ds}(k) + {L_q}^2 \lambda_{pm} \Big) =$$

$$= \frac{R_s T_s \lambda_{qs}(k) \Big/ L_d L_q}{(L_d - L_q)\lambda_{ds}(k) + L_q \lambda_{pm}} \Big((L_d + L_q)(L_d - L_q)\lambda_{ds}(k) + {L_q}^2 \lambda_{pm} \Big) =$$

$$= \frac{R_s T_s \lambda_{qs}(k) \Big/ L_d L_q}{(L_d - L_q)\lambda_{ds}(k) + L_q \lambda_{pm}} \Big(L_d (L_d - L_q)\lambda_{ds}(k) + L_q \Big((L_d - L_q)\lambda_{ds}(k) + L_q \lambda_{pm} \Big) \Big) =$$

$$= \frac{R_s T_s \lambda_{qs}(k)}{L_d L_q} \left(\frac{L_d (L_d - L_q)\lambda_{ds}(k)}{(L_d - L_q)\lambda_{ds}(k) + L_q \lambda_{pm}} + L_q \right) =$$

$$= \frac{R_s T_s}{L_d L_q} \left(\frac{L_d \lambda_{ds}(k)(L_d - L_q)\lambda_{qs}(k)}{(L_d - L_q)\lambda_{ds}(k) + L_q \lambda_{pm}} + L_q \lambda_{qs}(k) \right) \Rightarrow$$

$$\boxed{\Rightarrow B_{D\,R_s} = \frac{R_s T_s}{L_d L_q} \Big(L_q \lambda_{qs}(k) - M_D L_d \lambda_{ds}(k) \Big)}$$

6. Substitution of B_D for steady state on the SRC equation from (4)

$$\Big((B_D + \lambda_{qs1}) - M_D \lambda_{ds1} \Big)^2 \leq {\lambda_s^*}^2 (1 + {M_D}^2)$$

$$B_{D\,\omega} + B_{D\,R_s} + \lambda_{qs1} - M_D \lambda_{ds1} =$$

$$= \omega_r(k) T_s \big(\lambda_{ds} + M_D \lambda_{qs} \big) + \frac{R_s T_s}{L_d L_q} \Big(L_q \lambda_{qs}(k) - M_D L_d \lambda_{ds}(k) \Big) - R_s i_{qs}(k) T_s$$
$$- \omega_r(k) T_s \lambda_{ds}(k) + \lambda_{qs}(k) + M_D R_s i_{ds}(k) T_s - M_D \omega_r(k) T_s \lambda_{qs}(k)$$
$$- M_D \lambda_{ds}(k) = F_\omega + F_{R_s} + F_0$$

$$F_0 = \lambda_{qs}(k) - M_D \lambda_{ds}(k)$$

$$F_\omega = \omega_r(k) T_s \big(\lambda_{ds} + M_D \lambda_{qs} \big) - \omega_r(k) T_s \lambda_{ds}(k) - M_D \omega_r(k) T_s \lambda_{qs}(k) \Rightarrow F_\omega = 0$$

$$F_{R_s} = \frac{R_s T_s}{L_d L_q} \Big(L_q \lambda_{qs}(k) - M_D L_d \lambda_{ds}(k) \Big) - R_s i_{qs}(k) T_s + M_D R_s i_{ds}(k) T_s =$$

$$= \frac{R_s T_s}{L_d L_q}\left(L_q\lambda_{qs}(k) - M_D L_d \lambda_{ds}(k) - \frac{L_d L_q \lambda_{qs}(k)}{L_q} + \frac{L_d L_q M_D\left(\lambda_{ds}(k) - \lambda_{pm}\right)}{L_d}\right) \Rightarrow$$

$$\Rightarrow F_{R_s}\left(\frac{R_s T_s}{L_d L_q}\right)^{-1} = L_q\lambda_{qs}(k) - M_D L_d\lambda_{ds}(k) - L_d\lambda_{qs}(k) + L_q M_D\lambda_{ds}(k) - L_q M_D\lambda_{pm} =$$

$$= \lambda_{qs}(k)\left(L_q - L_d\right) + M_D\lambda_{ds}(k)\left(L_q - L_d\right) - L_q M_D\lambda_{pm} =$$

$$= \left(L_q - L_d\right)\left(\lambda_{qs}(k) + M_D\lambda_{ds}(k) + \frac{L_{qs} M_D\lambda_{pm}}{\left(L_d - L_q\right)}\right) \Rightarrow$$

$$\Rightarrow F_{R_s}\left(\frac{R_s T_s}{L_d L_q}\left(L_q - L_d\right)\right)^{-1} = \lambda_{qs}(k) + M_D\lambda_{ds}(k) + \frac{L_q M_D\lambda_{pm}}{\left(L_d - L_q\right)} =$$

$$= \lambda_{qs}(k) + M_D\left(\lambda_{ds}(k) + \frac{L_q\lambda_{pm}}{\left(L_d - L_q\right)}\right) =$$

$$= \lambda_{qs}(k) - \frac{\left(L_d - L_q\right)\lambda_{qs}(k)}{\left(L_d - L_q\right)\lambda_{ds}(k) + L_q\lambda_{pm}}\left(\lambda_{ds}(k) + \frac{L_q\lambda_{pm}}{\left(L_d - L_q\right)}\right) =$$

$$= \lambda_{qs}(k)\left(1 - \frac{\left(L_d - L_q\right)}{\left(L_d - L_q\right)\lambda_{ds}(k) + L_q\lambda_{pm}}\left(\lambda_{ds}(k) + \frac{L_q\lambda_{pm}}{\left(L_d - L_q\right)}\right)\right) =$$

$$= \lambda_{qs}(k)(1 - 1) = 0 \Rightarrow$$

$$\Rightarrow F_{R_s} = 0$$

$$\boxed{\Rightarrow \left(\lambda_{qs} - M_D\lambda_{ds}\right)^2 \leq \lambda_s^{*2}\left(1 + {M_D}^2\right)}$$

7. Substitution of M_D for steady state on the SRC equation from (6)

$$\left(\lambda_{qs} + \lambda_{ds}\frac{\left(L_d - L_q\right)\lambda_{qs}}{\left(L_d - L_q\right)\lambda_{ds} + L_q\lambda_{pm}}\right)^2 \leq \lambda_s^{*2}\left(1 + \frac{\left(L_d - L_q\right)^2{\lambda_{qs}}^2}{\left(\left(L_d - L_q\right)\lambda_{ds} + L_q\lambda_{pm}\right)^2}\right) \Rightarrow$$

$$\Rightarrow {\lambda_{qs}}^2\left(\left(L_d - L_q\right)\lambda_{ds} + L_q\lambda_{pm} + \lambda_{ds}\left(L_d - L_q\right)\right)^2$$

$$\leq \lambda_s^{*2}\left(\left((L_d - L_q)\lambda_{ds} + L_q\lambda_{pm}\right)^2 + \left(L_d - L_q\right)^2{\lambda_{qs}}^2\right) \Rightarrow$$

$$\Rightarrow \left(\lambda_s^{*2} - {\lambda_{ds}}^2\right)\left(2\left(L_d - L_q\right)\lambda_{ds} + L_q\lambda_{pm}\right)^2 \leq$$

$$\leq \lambda_s^{*2}\left(\left(L_d - L_q\right)^2{\lambda_{ds}}^2 + 2\left(L_d - L_q\right)L_q\lambda_{pm}\lambda_{ds} + {L_q}^2{\lambda_{pm}}^2 + \left(L_d - L_q\right)^2{\lambda_{qs}}^2\right) \Rightarrow$$

$$\Rightarrow \left(\lambda_s^{*2} - {\lambda_{ds}}^2\right)\left(4\left(L_d - L_q\right)^2{\lambda_{ds}}^2 + 4\left(L_d - L_q\right)L_q\lambda_{pm}\lambda_{ds} + {L_q}^2{\lambda_{pm}}^2\right) \leq$$

$$\leq \lambda_s^{*2}\left(\left(L_d - L_q\right)^2\left({\lambda_{ds}}^2 + {\lambda_{qs}}^2\right) + 2\left(L_d - L_q\right)L_q\lambda_{pm}\lambda_{ds} + {L_q}^2{\lambda_{pm}}^2\right) \Rightarrow$$

$$\Rightarrow \lambda_s^{*2}\left(4\left(L_d - L_q\right)^2{\lambda_{ds}}^2 + 4\left(L_d - L_q\right)L_q\lambda_{pm}\lambda_{ds} + {L_q}^2{\lambda_{pm}}^2\right)$$

$$-{\lambda_{ds}}^2\left(4\left(L_d - L_q\right)^2{\lambda_{ds}}^2 + 4\left(L_d - L_q\right)L_q\lambda_{pm}\lambda_{ds} + {L_q}^2{\lambda_{pm}}^2\right)$$

$$-\lambda_s^{*2}\left(\left(L_d - L_q\right)^2\lambda_s^{*2} + 2\left(L_d - L_q\right)L_q\lambda_{pm}\lambda_{ds} + {L_q}^2{\lambda_{pm}}^2\right) \leq 0 \Rightarrow$$

$$\Rightarrow \lambda_s^{*2}\left(4\left(L_d - L_q\right)^2{\lambda_{ds}}^2 + 2\left(L_d - L_q\right)L_q\lambda_{pm}\lambda_{ds} - \left(L_d - L_q\right)^2\lambda_s^{*2}\right)$$

$$-{\lambda_{ds}}^2\left(4\left(L_d - L_q\right)^2{\lambda_{ds}}^2 + 4\left(L_d - L_q\right)L_q\lambda_{pm}\lambda_{ds} + {L_q}^2{\lambda_{pm}}^2\right) \leq 0 \Rightarrow$$

$$\Rightarrow 4\left(L_d - L_q\right)^2{\lambda_{ds}}^4 + 4\left(L_d - L_q\right)L_q\lambda_{pm}{\lambda_{ds}}^3 + \left({L_q}^2{\lambda_{pm}}^2 - 4\lambda_s^{*2}\left(L_d - L_q\right)^2\right){\lambda_{ds}}^2$$
$$- 2\lambda_s^{*2}\left(L_d - L_q\right)L_q\lambda_{pm}\lambda_{ds} + \lambda_s^{*4}\left(L_d - L_q\right)^2 \geq 0$$

8. Identification of the terms of the inequality obtained in (7) with those of a squared quadratic equation

$$A{\lambda_{ds}}^4 + B{\lambda_{ds}}^3 + C{\lambda_{ds}}^2 + D\lambda_{ds} + E \geq 0$$

$$\left(a{\lambda_{ds}}^2 + b\lambda_{ds} + c\right)^2 \geq 0 \Rightarrow$$

$$\Rightarrow a^2{\lambda_{ds}}^4 + 2ab{\lambda_{ds}}^3 + (b^2 + 2ac){\lambda_{ds}}^2 + 2bc\lambda_{ds} + c^2\lambda_{ds} \geq 0$$

$$a^2 = A = 4\left(L_d - L_q\right)^2 \qquad \Rightarrow \qquad a = \sqrt{A} = 2\left(L_d - L_q\right)$$

$$2ab = B = 4\left(L_d - L_q\right)L_{qs}\lambda_{pm} \quad \Longrightarrow \quad b = \frac{B}{2a} = L_q\lambda_{pm}$$

$$b^2 + 2ac = C = {L_q}^2{\lambda_{pm}}^2 - 4\lambda_s^{*2}\left(L_d - L_q\right)^2 \quad \Longrightarrow \quad c = \frac{C - b^2}{2a} = -\lambda_s^{*2}\left(L_d - L_q\right)$$

9. Checking the of the rest of the terms

$$D = -2\lambda_s^{*2}\left(L_d - L_q\right)L_q\lambda_{pm}\lambda_{ds} = 2\left(L_q\lambda_{pm}\right)\left(-\lambda_s^{*2}\left(L_d - L_q\right)\right) = 2bc$$

$$E = \lambda_s^{*4}\left(L_d - L_q\right)^2 = \left(-\lambda_s^{*2}\left(L_d - L_q\right)\right)^2 = c^2$$

10. Substitution of the terms found in (8) in the quadratic equation

$$a{\lambda_{ds}}^2 + b\lambda_{ds} + c \geq 0$$

$$\boxed{2\left(L_d - L_q\right){\lambda_{ds}}^2 + L_q\lambda_{pm}\lambda_{ds} - \lambda_s^{*2}\left(L_d - L_q\right) \geq 0}$$

Appendix B: Data Analysis Scripts

7.1. MatLab code for DB-DTFC Implementation

```
% Calculation of M and B
M=[(Lq-Ld)*Yq]/[(Ld-Lq)*Yd+Lq*Ypm];
b1=(4*Ld*Lq/3/P)*dT;
b2=w*Ts*[(Yd^2-Yq^2)*(Ld-Lq)+(Ypm*Yd*Lq)];
b3=[(R*Yq*Ts)/(Ld*Lq)]*[Yd*(Ld^2-Lq^2)+Ypm*Lq^2];
B=[1/((Ld-Lq)*Yd+Lq*Ypm)]*[b1+b2+b3];

% Square Root Condition
Bmin=-Y*sqrt(1+M^2)+M*Yd1-Yq1;
Bmax=Y*sqrt(1+M^2)+M*Yd1-Yq1;
K0=min(Bmax,B);
K=max(Bmin,K0);

% Decoupling
Yq1=Yq-R*iq*Ts-w*Yd*Ts;
Yd1=Yd-R*id*Ts+w*Yq*Ts;

% calculation of Ud and Uq
a=[M^2+1]*Ts^2;
b=2*Ts*[Yd1+M*Yq1+M*K];
c=Yd1^2+Yq1^2+K^2+2*Yq1*K-Y^2;
delta=(b^2)-(4*a*c);
Ud=real(-b+sqrt(complex(b^2-4*a*c)))/real(2*a);
Uq=[M*Ud*Ts+K]/Ts;
```

Script B.1: MatLab code for DB-DTFC implementation including SRC algorithm [15].

7.2. Testbench Setup Pictures

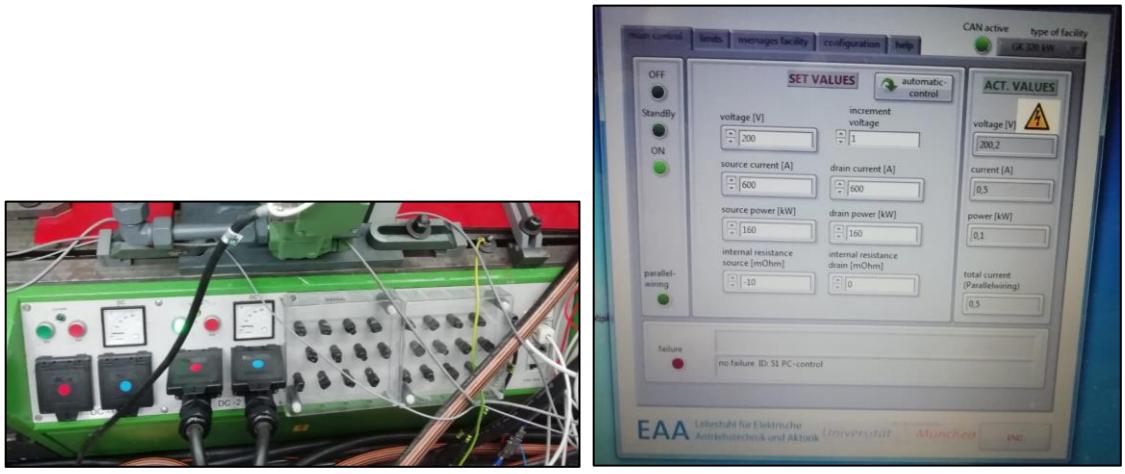

Figure B.1: GustavKlein DC power supply and DC bus cotrol.

Figure B.2: DC load machine and controller.

Figure B.3: Gearbox.

Figure B.4: Signal processing and measureemnt adaptation rig.

Figure B.5: Inverter and Protection stage with circuit breakers

Figure B.6: Cooling systems

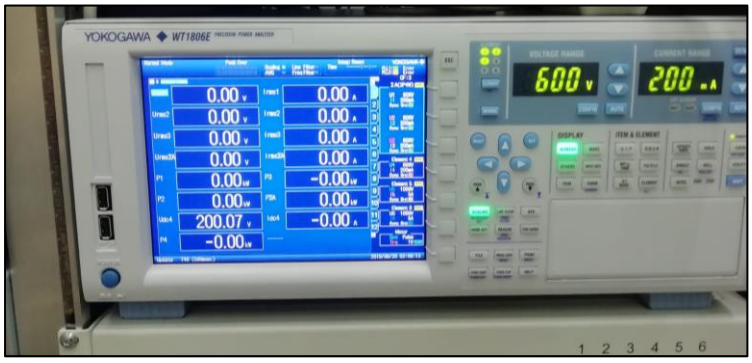

Figure B.7: Yokogawa WT 1800 PowerAnalyser.

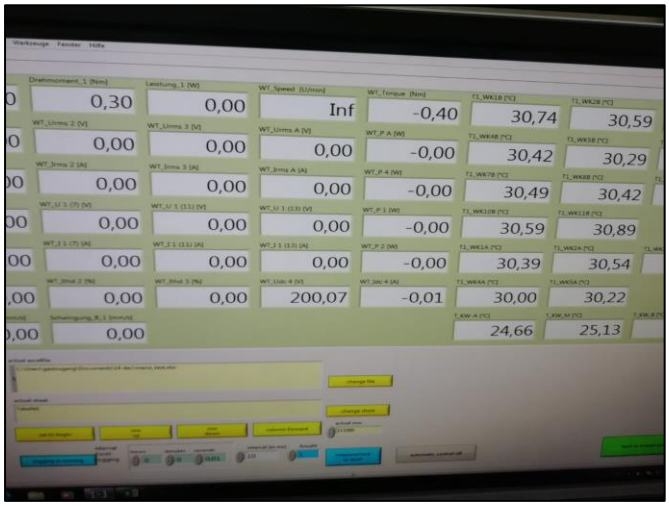

Figure B.8: LabView aplication

Figure B.9: dSPACE Autobox and ControlDesk application

Figure B.10: 8-Channel LeCroy HDO8108 Oscilloscope

7.3. Reading Script for dSPACE Files

The script for reading the dSPACE exported files follows the algorithm below:

1. Obtain the names of all .mat files in the directory and selecting those containing raw data
2. If previously stored, load the time windows data

For each of the data files:

3. Check if the file identification is part of the list of experiments

If it is:

4. Load the experiment name and separate it into the appropriate categories
5. If previously stored, load the time window for that specific test

6. Load the signals listed in Table B.1 according to their identifiers in the raw data file (Name or Name and Path information). Store in a temporal structure with its new name, label and time interrupt used for its acquisition.
    a. The identifier (id) selected is searched in the directory (a) selected
    b. The Name is compared to the name provided ('nameid')
    c. If there is some data satisfying the search
    d. If multiple variables match both identifications, the one with the highest number of points is selected (higher resolution timer)
    e. The data and the information about the timer used is stored in a provisional signal structure. If the timer used has higher resolution than the originally considered one, the data is interpolated on the higher resolution time vector
    f. The provisional signal structure is stored into the provisional experiment structure
7. Interpolate all signals to the longest time interrupt stored (preserving the original data in another category)
8. Save all the time signals
9. If specific time windows are to be selected and the data for them is not stored from previous attempts to read the experiment data:
    a. Confirm if a window is to be selected or the whole data is valid
    b. Plot the data for the complete time stored
    c. Input the initial and final time of the desired window
    d. Plot the data for the selected time window
    e. Confirm the selected window or repeat from 'b'
10. Save the data in the appropriate categories of the final structure
11. Save the time window selected for later speeding the loading of the data
12. Repeat from 3 until all raw data files are checked

The "Read_Steady_state" script is a special case of "Read_dSpace" in which the window selected corresponds to a certain steady state to be analyzed instead of the operation during the change of the operating point or some parameter affecting the operation. Similarly, "Read_Transient" is another special case selecting multiple time windows corresponding to the transients between specific operating points.

Signal label	Signal name	Units
Torque	Tq	Nm
Torque set point	TqSp	
Torque set point Limited	TqSpLim	
Rotor speed	Speed	rpm
Power estimated	Power	W
Estimated flux	Ydq	Vs
Flux set point	YdqSp	
Y_MTPA LUT	Y_MTPA1	
Y_MTPA new	Y_MTPA2	
Y_MTPA old	Y_MTPA_o	
Y_MTPA new	Y_MTPA_n	
Flux d-axis	Yd	
Flux q-axis	Yq	
Total Current	Istrr	A
	Istrr123	
Phase current a	ia	
Current d-axis	iD	
	iDobs	
Current q-axis	iQ	
	iQobs	
DC link	Udc	V
Voltage set point d-axis	UdSp	
Voltage set point q-axis	UqSp	
Total Voltage set point	UdqSp	
Voltage alpha-axis	Ualpha	
	Ualpha2	
Voltage beta-axis	Ubeta	
Duty phase a	da	[]
Duty phase b	db	
Duty phase c	dc	
Modulation index	Midx	
PM flux	Ypm	Vs
Inductance d-axis	Ld	H
Inductance q-axis	Lq	

Stator resistance	Rs	Ω
M DB-DTFC	M	[]
B DB-DTFC	B	Vs
B0 DB-DTFC	B0	
Yd1 DB-DTFC	Yd1	
Yq1 DB-DTFC	Yq1	
Vertex chosen (new algorithm)	SixStep_k	1-6
SRC saturation active	SRC_cond	1/0
Transformation angle	theta_trans	°
DTC block angle	theta_DTC	
Main Switch	MainSwi	1/0

Table B.1: Varaiables stored from the dSPACE system.

7.4. Reading Script for Measurement Files

The script for reading the sensors and power analyser exported files follows the algorithm below:

1. Obtain the name of the '.xlsx' file in the directory
2. If previously stored, load the time windows data
3. Obtain the names of the sheets in the loaded file

For each of the data files:

4. Check if the sheet identification is part of the list of experiments

If it is:

5. Load the experiment name and separate it into the appropriate categories
6. If previously stored, load the time window for that specific test
7. Load the signals listed in Table B.2 according to their identifiers in the raw data file (column in the sheet). Store in a temporal structure with its new name and label.
8. If specific time windows are to be selected and the data for them is not stored from previous attempts to read the experiment data:
    a. Confirm if a window is to be selected or the whole data is valid
    b. Plot the data for the complete time stored
    c. Input the initial and final time of the desired window
    d. Plot the data for the selected time window

e. Confirm the selected window or repeat from ‘b’

9. Save the data in the appropriate categories of the final structure
10. Save the time window selected for later speeding the loading of the data
11. Repeat from 3 until all raw data files are checked

Signal label	Signal name	Units
Udc measured	Udc_xcl	V
U1 RMS measured	U1rms_xcl	V_{rms}
U2 RMS measured	U2rms_xcl	
U3 RMS measured	U2rms_xcl	
U RMS summed measured	UTotrms_xcl	
U1 THD measured	U1thd_xcl	%
U2 THD measured	U2thd_xcl	
U3 THD measured	U3thd_xcl	
Idc measured	Idc_xcl	A
I1 RMS measured	I1rms_xcl	A_{rms}
I2 RMS measured	I2rms_xcl	
I3 RMS measured	I2rms_xcl	
I RMS summed measured	ITotrms_xcl	
I1 THD measured	I1thd_xcl	%
I2 THD measured	I2thd_xcl	
I3 THD measured	I3thd_xcl	
Electric power	ElecPower_xcl	W
Mechanical power	MechcPower_xcl	
Mechanical power WT	MechcPowerWT_xcl	
Speed measured	Speed_xcl	rpm
Speed measured WT	SpeedWT_xcl	
Torque measured	Torque_xcl	Nm
Torque measured WT	TorqueWT_xcl	
Power calculated	Power_xcl	W
Power calculated WT	PowerWT_xcl	
Mech. harmonic A	HarmA_xcl	mm/s
Mech. harmonic B	HarmB_xcl	
time measurements	time_xcl	s

Table B.2: Varaiables stored from the sensor measurements.

There were other measurements available, such as multiple temperature sensors, power calculated for each of the phases and the dc supply and cooler flow to the inverter and motor.

7.5. Reading Script for Oscilloscope Files

The script for reading the sensors and power analyser exported files follows the algorithm below:

1. Obtain the names of the '.csv' files in the directory

For each of the data files:

2. Detect the signal and the experiment it belongs to
3. Store the scaled data, label and time in the appropriate category of the final structure according to its experiment

For each of the experiments:

4. Replace the experiment name with the assigned one according to the table

For each of the experiments, if the duty calculation is required:

If the experiment contains the information of the three line to line voltages

5. Detect or assign the value of the DC bus voltage

For each of the voltage signals:

6. Compare at each time the absolute value of the signal with half of the dc bus voltage (This converts the measurements in 1,0 and -1 values)
7. Reject pulses of 3 or less points (the pulse detection being triggered by transients or noise)
8. Detect the switching instants (changes of the pulses from 0 to 1 or -1)
9. Calculation of the duty between triggers (this includes the assumption of a trigger instant in between two detected ones if the time between them is higher than the switching period of the inverter)
10. Conversion of the calculated duty signal to the original time vector using a zero-order-hold
11. Naming and labeling of the duty signal according to the voltage signal analyzed

For each of the experiments, if the phase voltage calculation is required:

If the experiment contains the information of the three line to line voltages:

12. Convert the line to line voltages into phase voltages assuming a balanced 3 phase system (this required a careful evaluation of the dSPACE an Oscilloscope signals to ensure the same names were given to corresponding signals)
13. The same is done for the duties if they had been calculated before.

For each of the experiments:

14. Save the data in the appropriate categories of the final structure

7.6. Merging of Measurement and dSPACE Files

The script for merging the data from the sensor measurements and the dSPACE is executed only if both measurements file ('XCL') and dSPACE signals file ('dSP') have the same number of categories. Considering the 'level' in which the signals are stored within the structure, the loading of the data takes a slightly different form, but once this is done, the script follows the algorithm below:

For all experiments in the dSP file

1. For each of the variables stored in dSP, store them in an equivalent structure
2. If the same experiment is present in XCL, store them in the new structure and remove them from the XCL file

For all the experiments in the XCL file

3. If there are any non-empty experiments (i.e. they have not been merged with the previous algorithm), create the category for this experiment in the merged structure and store the signals

7.7. Merging and Synchronization of Oscilloscope and dSPACE Files

The scripts for merging and synchronizing the data from the oscilloscope and dSPACE are executed only if both oscilloscope file ('Oscil') and dSPACE signals file ('dSP') have the same number of categories. Considering the 'level' in which the signals are stored within the structure, the loading of the data takes a slightly different form, but once this is done, the algorithm followed is presented below:

For all experiments in the dSP file:

1. For each of the variables stored in dSP, store them in an equivalent structure
2. If the same experiment is present in XCL, store them in the new structure and remove them from the XCL file

For all the experiments in the XCL file:

3. If there are any non-empty experiments (i.e. they have not been merged with the previous algorithm), create the category for this experiment in the merged structure and store the signals

Only if both 'Oscil' file (Oscilloscope) and 'dSP' file (dSPACE signals) have the same number of categories, the files are synchronized. The algorithm followed is presented below:

1. If previously stored, load the time lag for that specific test (this corresponds to the time that must be added to the dSP time signal so that the data from both instruments is synchronized)

For all experiments in both files:

2. New provisional structures 'Oscil' and 'dSpc' are created for easier handling of the data
3. If previously stored, load the time lag for that specific test. If not, the time lag is considered 0.
4. Modify the oscilloscope time signal so that it starts from 0
5. Store all variables from 'Oscil' into a category of a new structure 'Sync'
6. Remove the fields from 'dSP' corresponding to the timer interrupts, and modify the time signal to start from 0
7. Store all variables from 'dSpc' into a category of a new structure 'Sync'
8. Add the time lag to the 'dSpc' time
9. Plot variables from 'Oscil' and 'dSpc' together to identify where the trigger takes place in both measurements (Voltages, currents, torque, Main Switch activation, duties)
10. Input the time at which the trigger takes place in each of the experiments, and if the synchronization must continue to take place.
11. Calculate the new time lag and the total time lag (accumulation of previous ones for that experiment)
12. If the synchronization must continue, repeat from (8)
13. Remove the data points for which there is a NaN value in the time vector

14. If both experiments are to be combined (for later frequency analysis)
    a. Displace both time signals by the maximum of the starting point of both time windows
    b. Calculate the minimum of the maximum ending point of both time windows
    c. Remove the data in both time windows corresponding to a negative time
    d. Remove the data in both time windows corresponding to a time bigger than the one calculated in (b)
15. Store the signals from 'Sync.Oscil' in a new structure 'Sync_same' adding the string '_oscil' at the end of their name
16. Store the signals from 'Sync. dSpc' in the new structure 'Sync_same'
17. If both experiments are to be combined (for later frequency analysis)
    a. Interpolate the data from the dSPACE to match the time from the oscilloscope signals
    b. Remove the original dSPACE time signal (they are the same now from both instruments)
18. The processed data and the time lag are then stored into new structures with categories analogous to the previous ones depending on the experiments.

7.8. Frequency Analysis

The frequency analysis is only applied to the oscilloscope data and the data from the dSPACE that was obtained with a high-resolution timer (ADC timer tasks). After the synchronization has been completed, the algorithm followed by the script is:

1. If previously stored, the windows and variable names to be analyzed are loaded. Otherwise, the appropriate signals are selected form the data structure. An interactive figure generation and input program allows for the selection of an appropriate window for the frequency analysis.

For all signals to be analyzed in the selected time window:

2. The time and data vectors are stored in new variables
3. The time vector is readjusted to start from 0, and NaN values are removed
4. The time vector is substituted with another of equal length and time span but with equally spaced points. The data vector is interpolated in this new time vector

5. The frequency vector is calculated
6. RMS and mean value of the data vector are computed.
7. Hanning window is applied to improve angle estimation of the frequency analysis
8. Discrete fast Fourier transform is applied to the data signal.
9. The fundamental frequency is detected
10. The first n harmonics are detected by dividing the frequency response according to the fundamental frequency. The frequency, amplitude and angle of each of them are stored.
11. The higher frequency peaks of the signal are detected and stored as well.
12. The frequency analysis data is stored in a structure

If the command was set at the start to apply window averaging.

13. The data signal is divided in equal length time intervals according to the number of windows desired and the fundamental period (in order for the intervals to include a whole number of fundamental periods)
14. The time window k is selected, and points from 5 to 11 are executed to the corresponding window data
15. The information obtained from all the windows is averaged and stored in a structure.
16. The information about the window selected and signals analysed is stored for later convenience.

Appendix C: Testbench Analysis Figures

8.1. Back-EMF Frequency Analysis

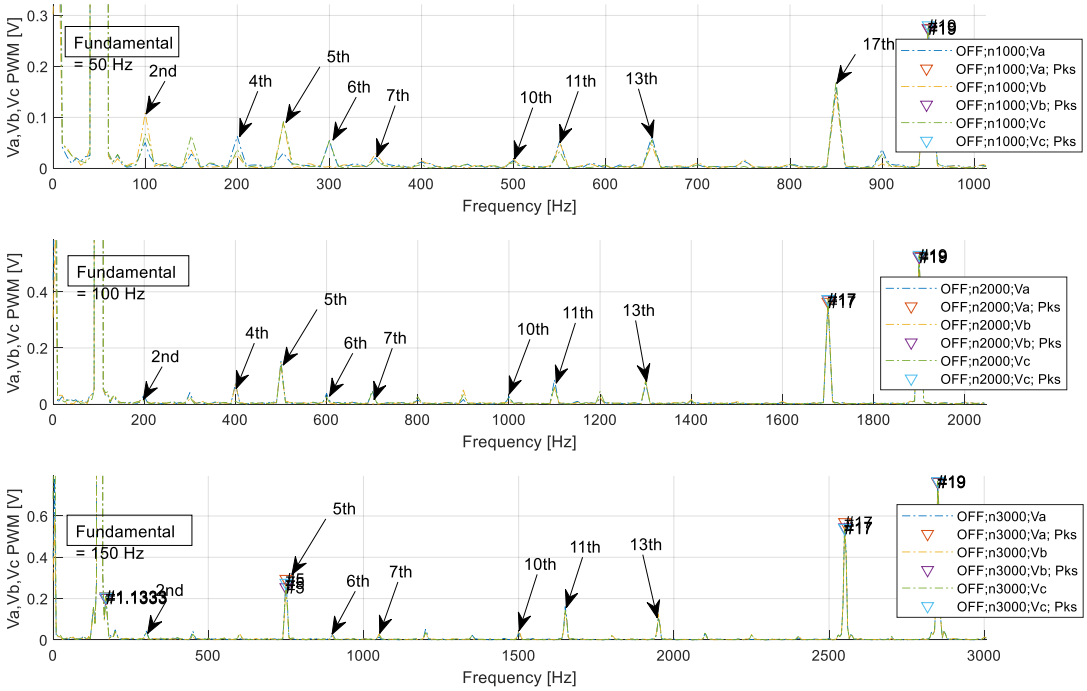

Figure C.1: Frequency analysis of the back EMF in the stator windings at three different speeds

8.2. Oscilloscope Waveforms Comparison with dSPACE and Power Analyzer Data

Results for V_{DC} = 100 V

n = 500 rpm	n = 1000 rpm
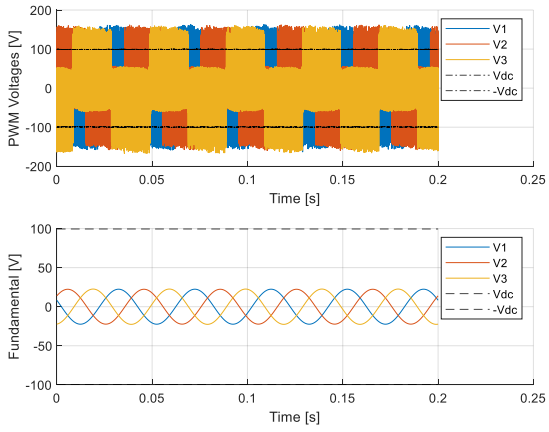	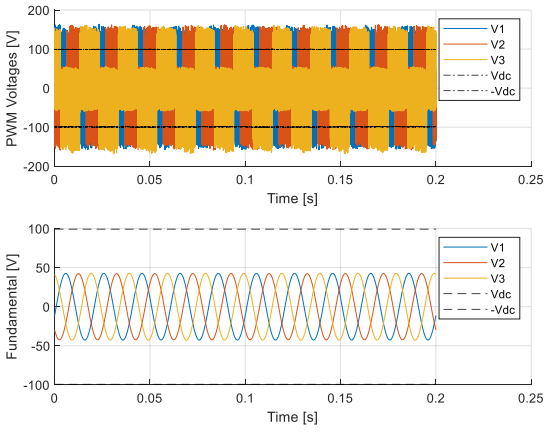

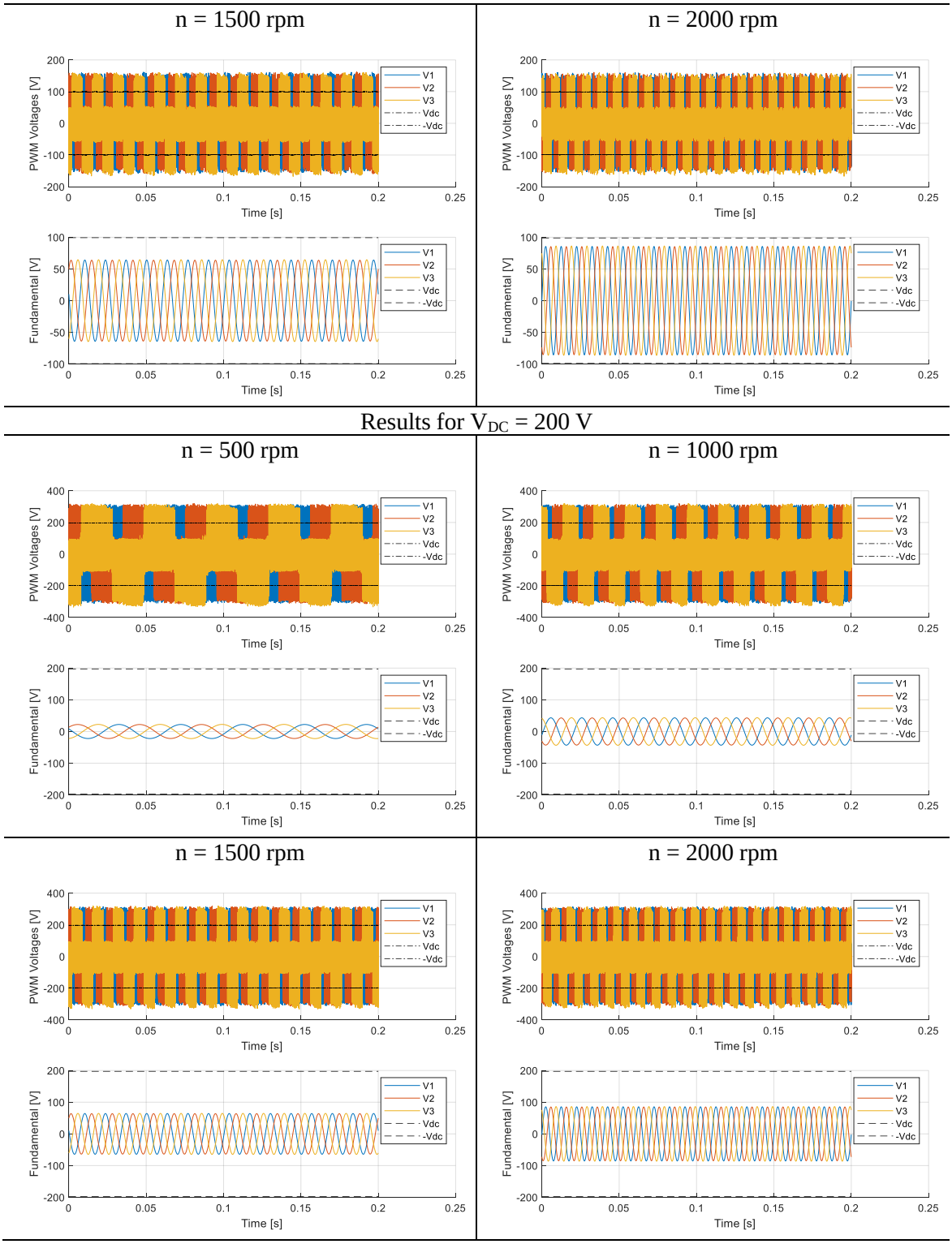

Figure C.2: Oscilloscope waveforms and fundamental component for differnts speeds and DC bus voltages and constant torque operation

8.3. Synchronization Effort for Comparison of Stator Voltage Command with Oscilloscope Measurements

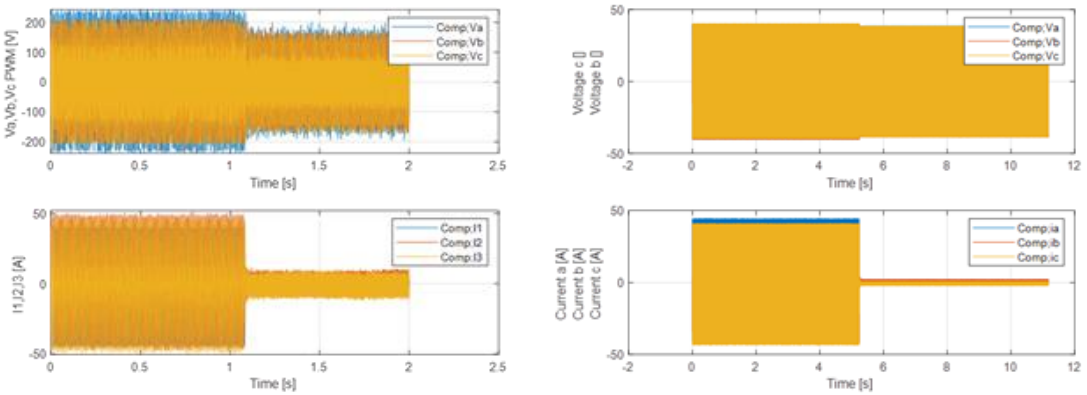

Figure C.3: Obtained waveforms. Left: Oscilloscope; Right: dSPACE; Up: Voltages; Down: Currents.

The measured voltage appears to oscillate between 200 and -200 but this is only due to the overshoot during the PWM pulses. The pulse generated oscillates between 100 and -100 V (DC bus voltage).

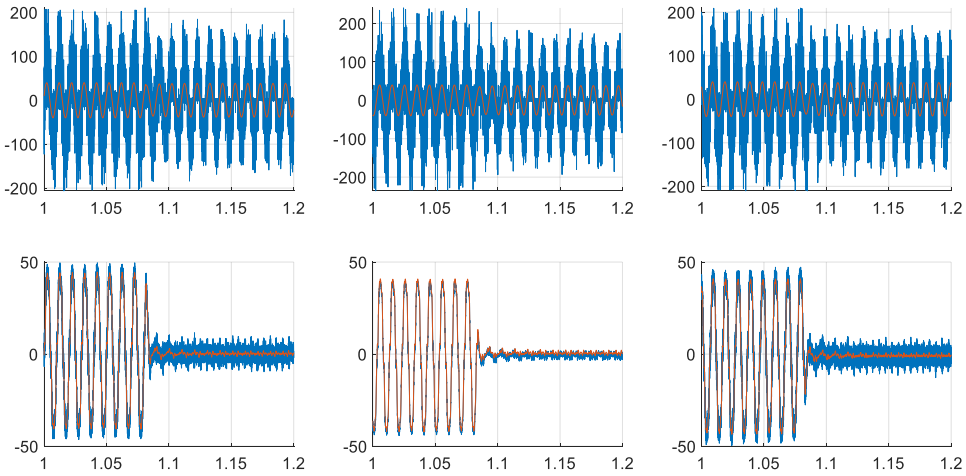

Figure C.4: Synchronized signals. Upper row: phase voltages; Lower row: phase currents. Blue: Oscilloscope; Red: dSPACE.

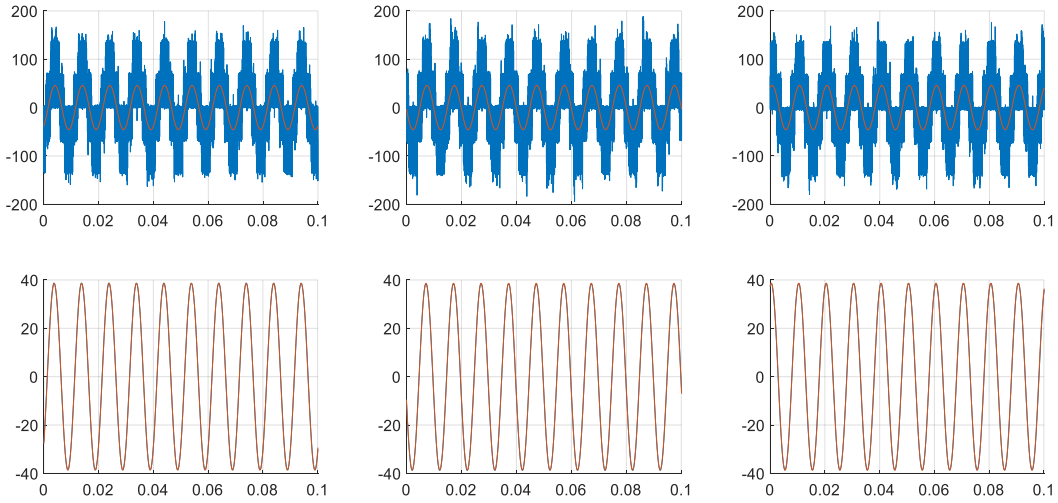

Figure C.5: Voltages frequency analysis. Upper row: Oscilloscope; Lower row: dSPACE. Blue: Original signal; Red: Fundamental component.

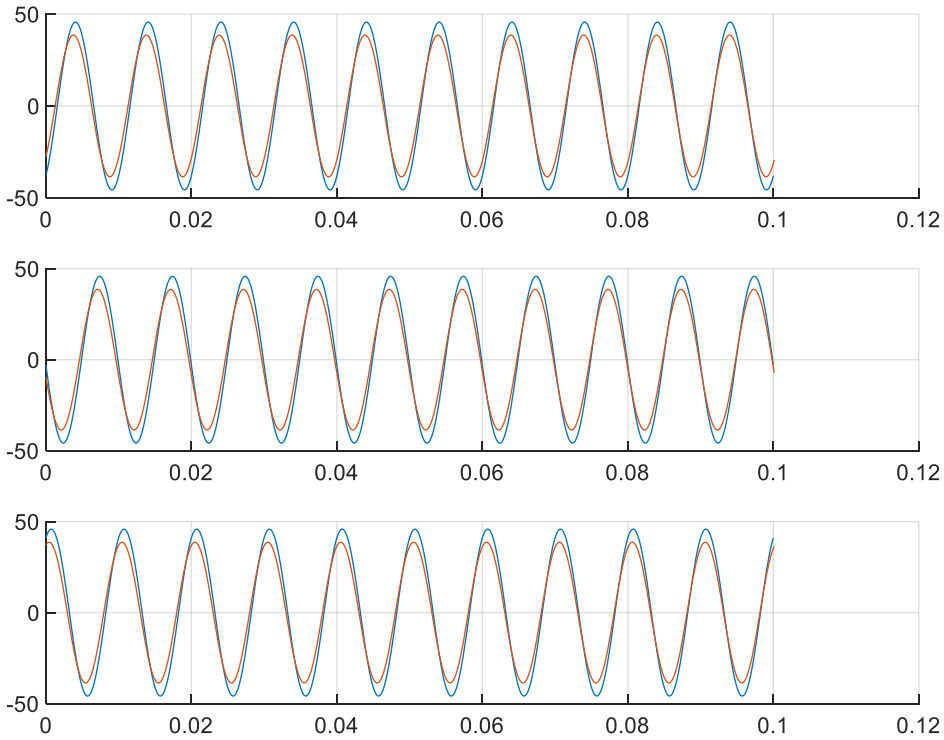

Figure C.6: Fundamental voltage comparisson. Blue: Oscilloscope; Red: dSPACE.

Appendix D: Overmodulation Strategies Tests

9.1. DTC Six-Step Condition Implementation

```
% Six step operation
if flux_cond == 1
    if mod(theta,pi/3)<=pi/6
        if dT ==1
            dY = 0;
        else
            dY = 1;
        end
    else
        if dT == 1
            dY = 1;
        else
            dY = 0;
        end
    end
    if Ydq >= Ymax
        dY = 0;
    end
    if Ydq <= Yref
        dY = 1;
    end
end
```

Script D.1: Six step condition for DTC implementation.

9.2. DB-DTFC Switching Table Implementation

```
% Voltage hexagon in dq reference frame
V_vert = Udc*Ts*sqrt(2)/3;
ang_vert = (pi/3)*[0 1 2 3 4 5 6].';
Amp_Hex_dq = V_vert;
Ang_Hex_dq = mod(ang_vert - thetae,2*pi);
UdTsk = Amp_Hex_dq.*cos(Ang_Hex_dq);
UqTsk = Amp_Hex_dq.*sin(Ang_Hex_dq);

%Torque line for delta_T = 0
M  = [(Lq-Ld)*Yq]/[(Ld-Lq)*Yd+Lq*Ypm];
b2 = w*Ts*[(Yd^2-Yq^2)*(Ld-Lq)+(Ypm*Yd*Lq)];
b3 = [(R*Yq*Ts)/(Ld*Lq)]*[Yd*(Ld^2-Lq^2)+Ypm*Lq^2];
B  = [1/((Ld-Lq)*Yd+Lq*Ypm)]*[b2+b3];

%Torque condition
B_Hex = UqTsk - M*UdTsk;
T1_v = B_Hex>B;

%Flux circle for delta_Y = 0
```

```
%Flux circle for delta_Y = 0
Yq1 = Yq-R*iq*Ts-w*Yd*Ts;
Yd1 = Yd-R*id*Ts+w*Yq*Ts;
Y2 = Yq^2+Yd^2;

%Flux condition
Y_dist2 = (UdTsk + Yd1).^2 + (UqTsk + Yq1).^2;
Y1_v = Y_dist2>Y2;
```

Script D.2: Matlab code for DB-DTFC six-step voltage torque and flux condition evaluation

9.3. Flux Limit Calculation in terms of Maximum Voltage Setting

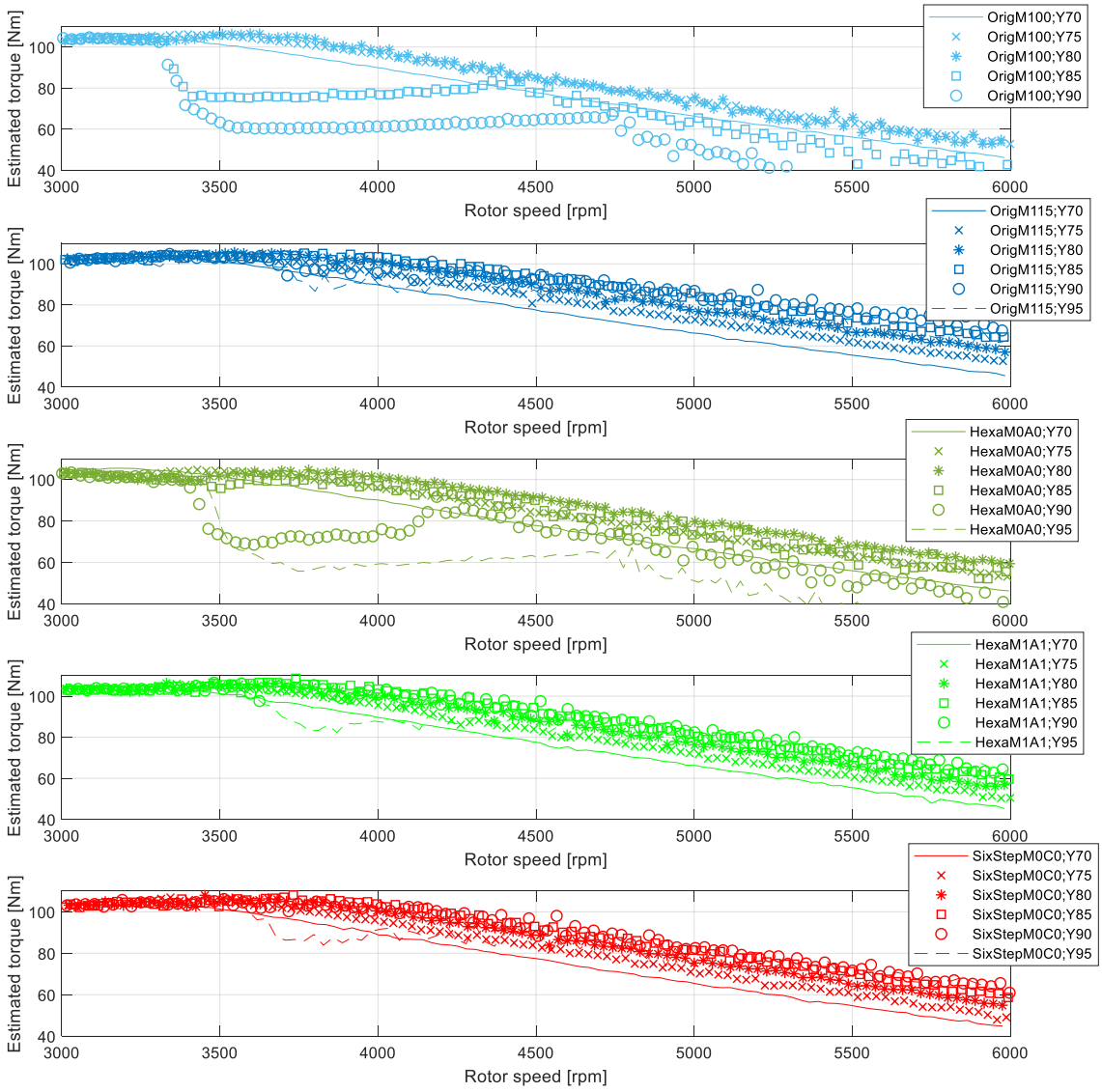

Figure D.1: Torque performance of overmodulation strategies according to V_{max} value. Individual subplots for each strategy.

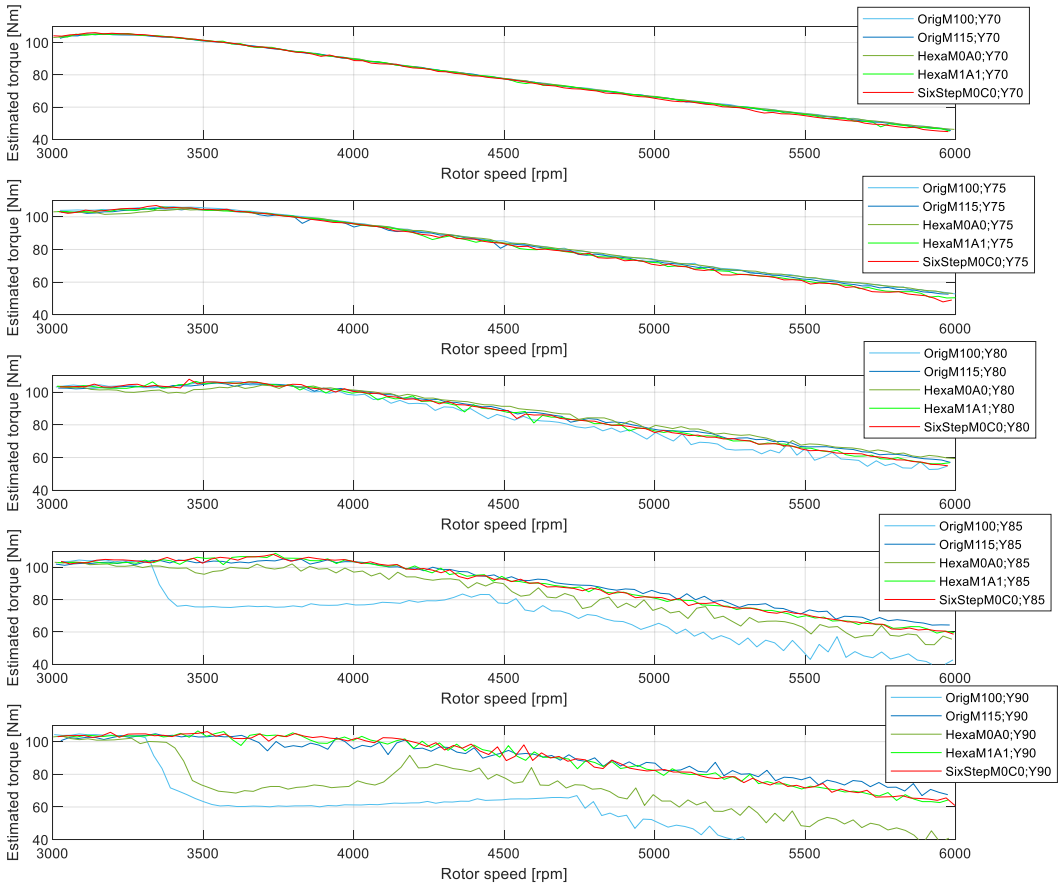

Figure D.2: Torque performance of overmodulation strategies according to V_{max} value. Individual subplots for each strategy. Filtered data.

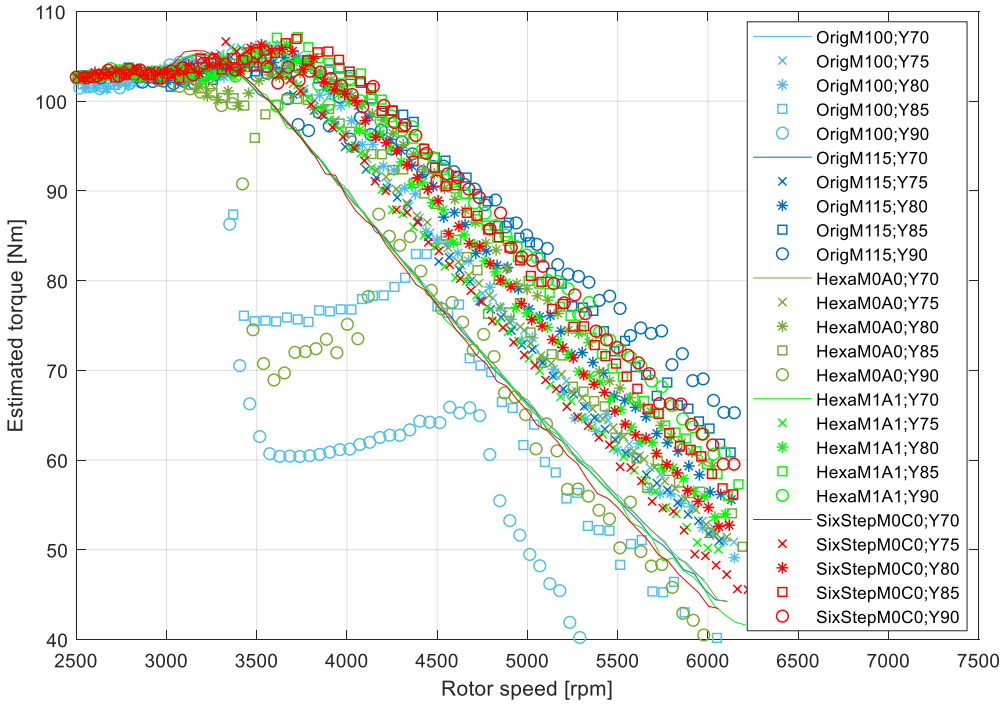

Figure D.3: Torque performance of overmodulation strategies according to V_{max} value.

9.4. Flux Limit Calculation in terms of Voltage Margin Gain Setting

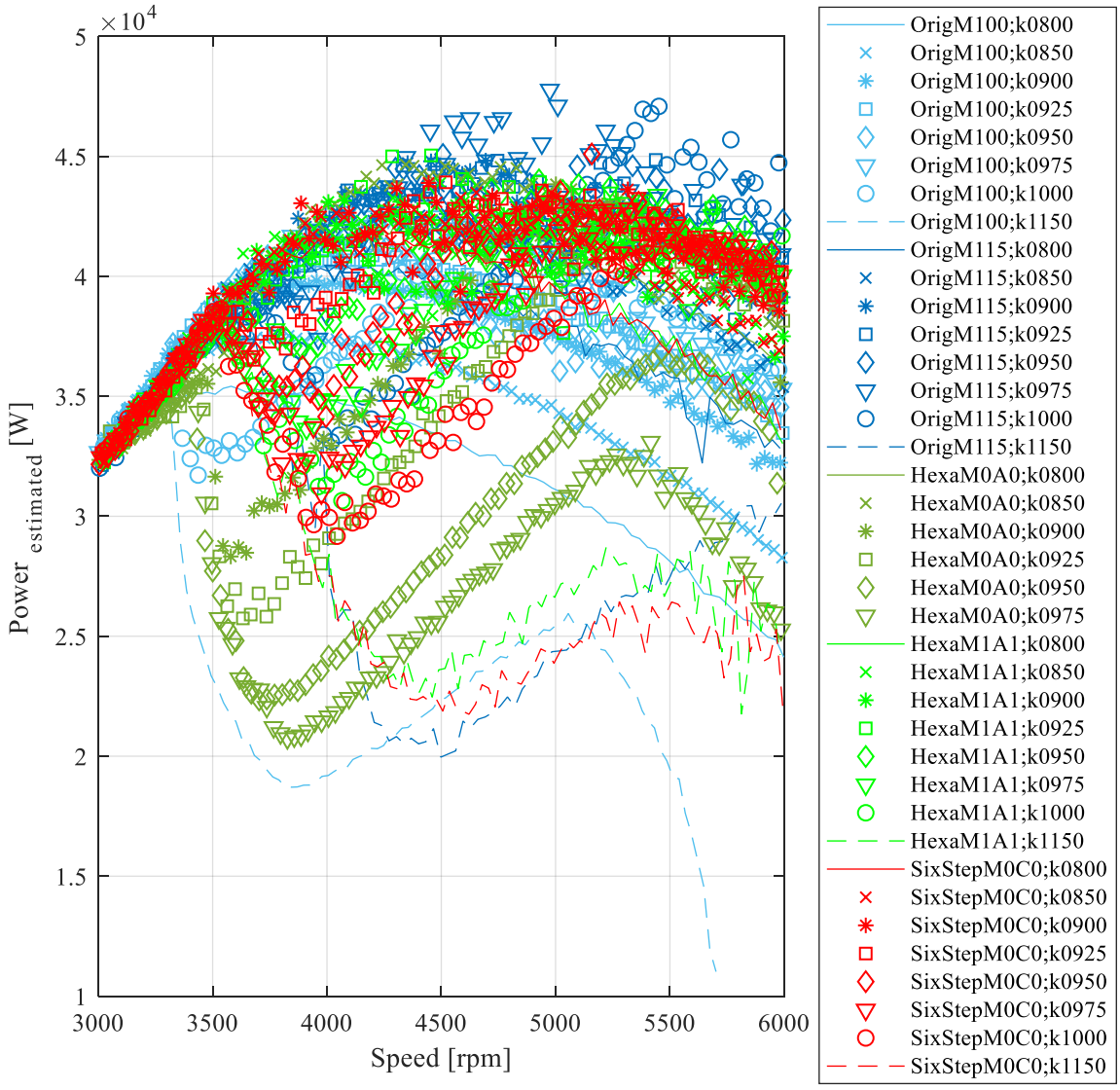

Figure D.4: Power performance of overmodulation strategies according to k_{max} value.

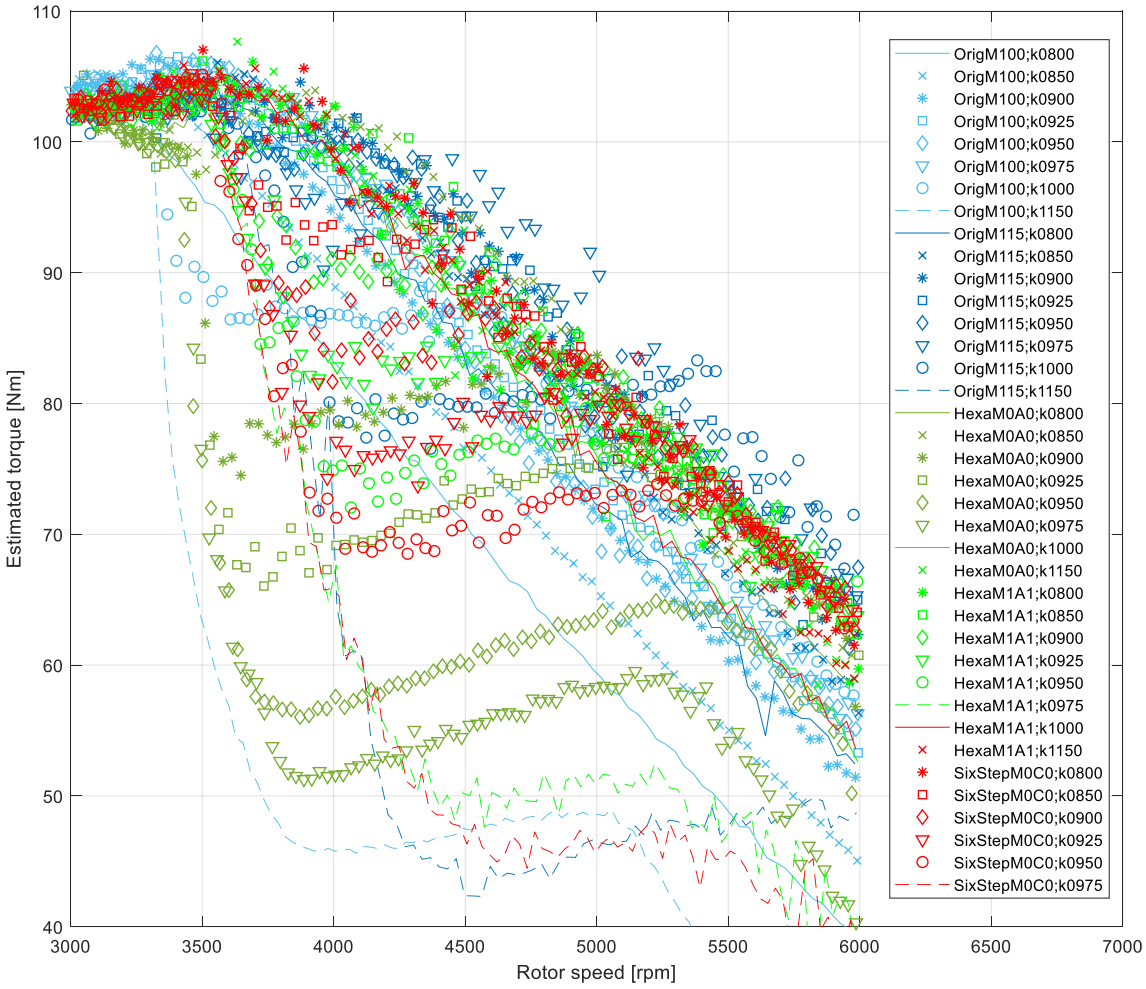

Figure D.5: Torque performance of overmodulation strategies according to k_{max} value.

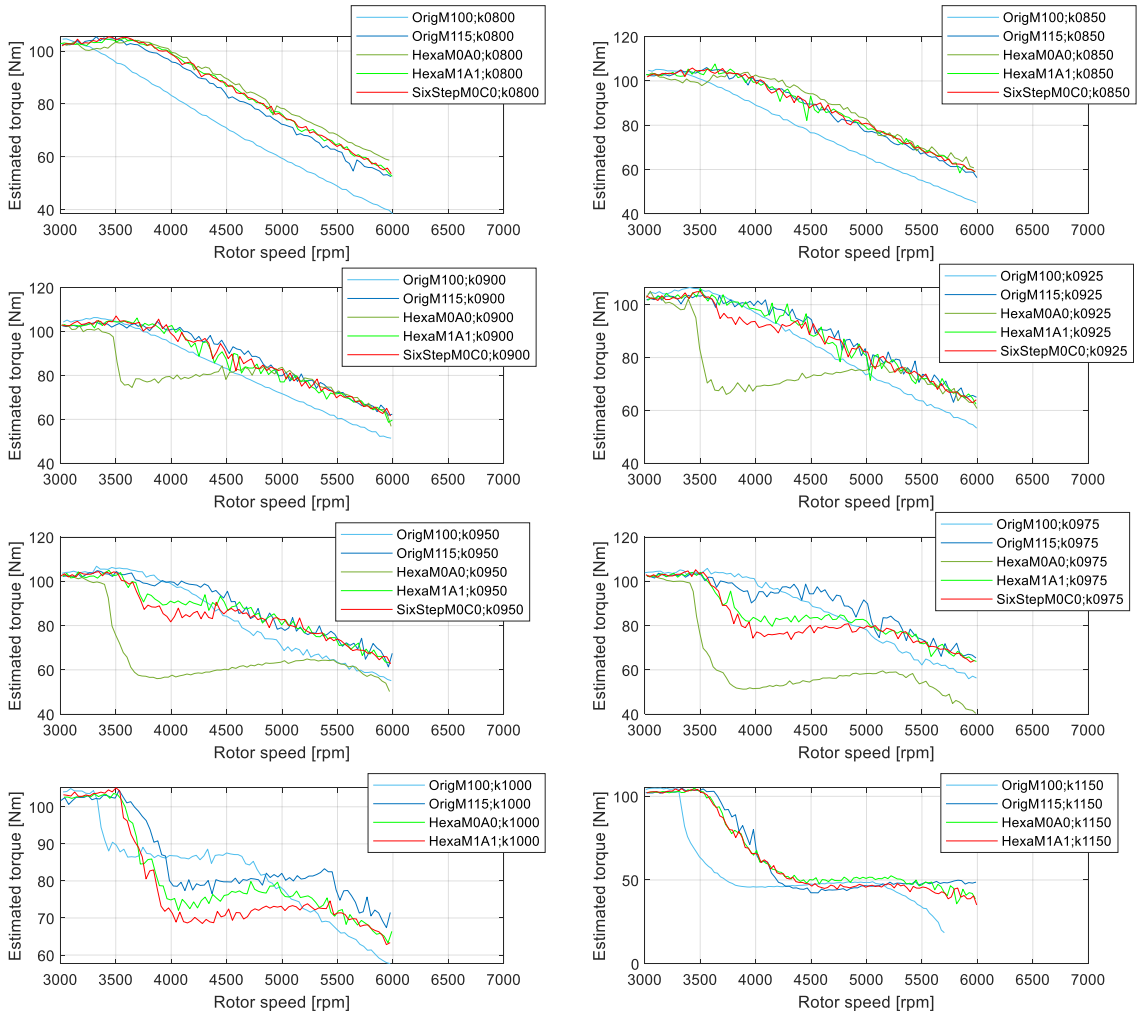

Figure D.6: Torque performance of overmodulation strategies according to k_{max} value. Individual plot for each k_{max}. Filtered signals.

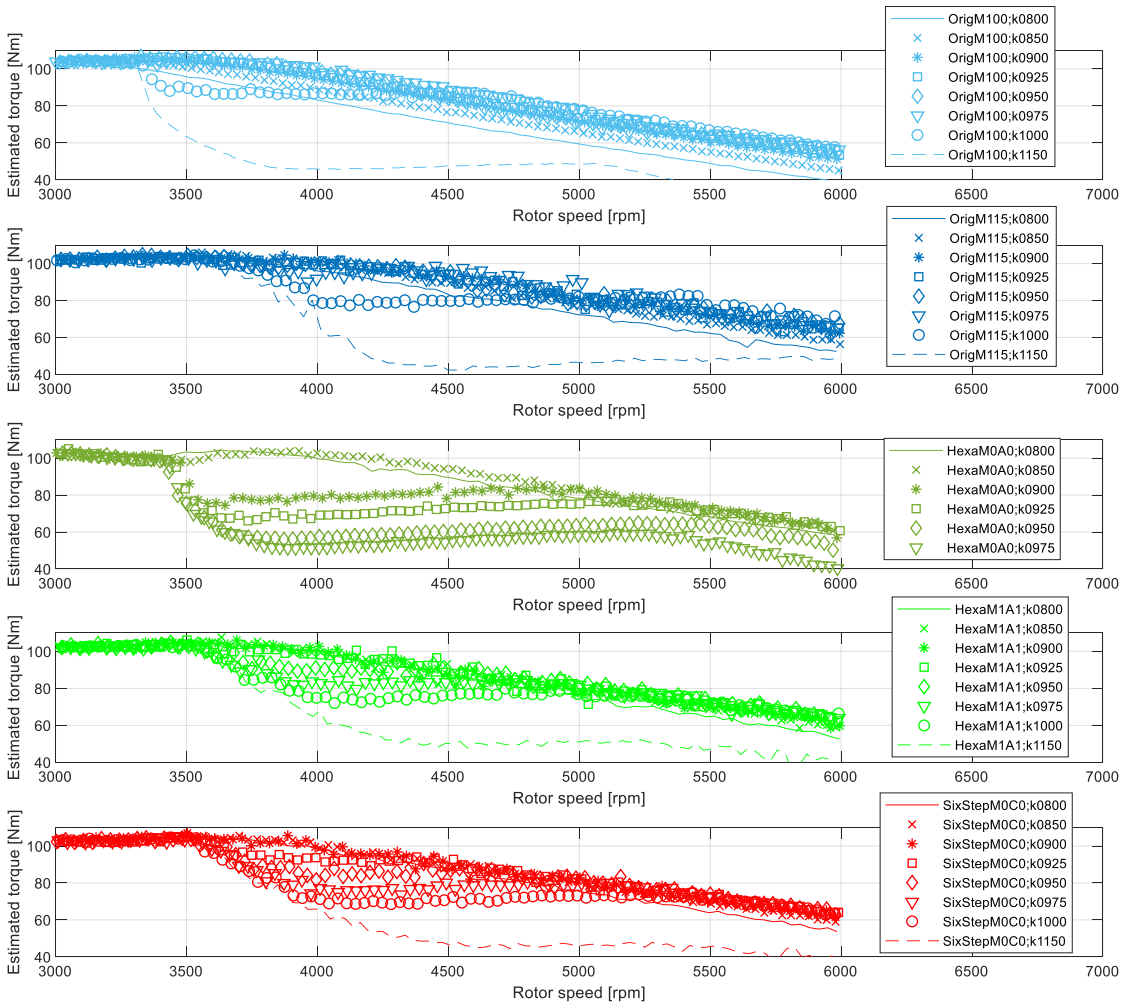

Figure D.7: Torque performance of overmodulation strategies according to k_{max} value. Individual subplots for each strategy.

9.5. Dynamic Flux Weakening Limit Adaptation

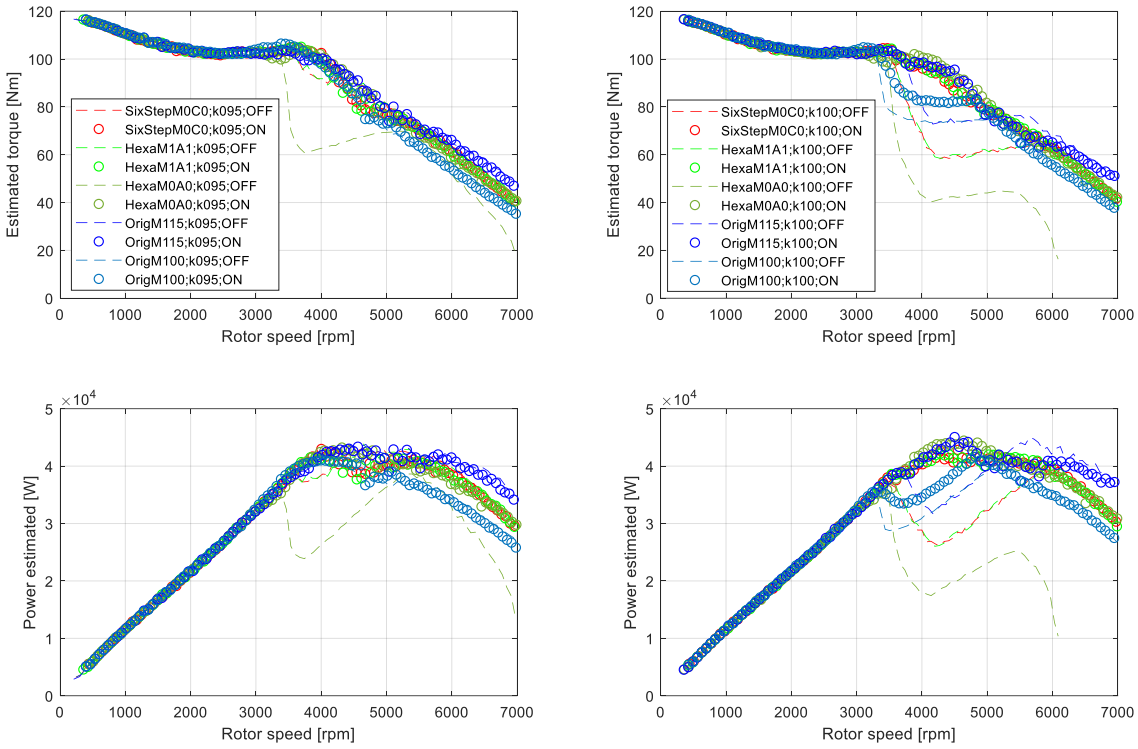

Figure D.8: Maximum torque and power performance with active or inactive dynamic flux weakening reference adaptaiton for two different (Left: k_{max}= 0.95; Right: k_{max}= 1.00)

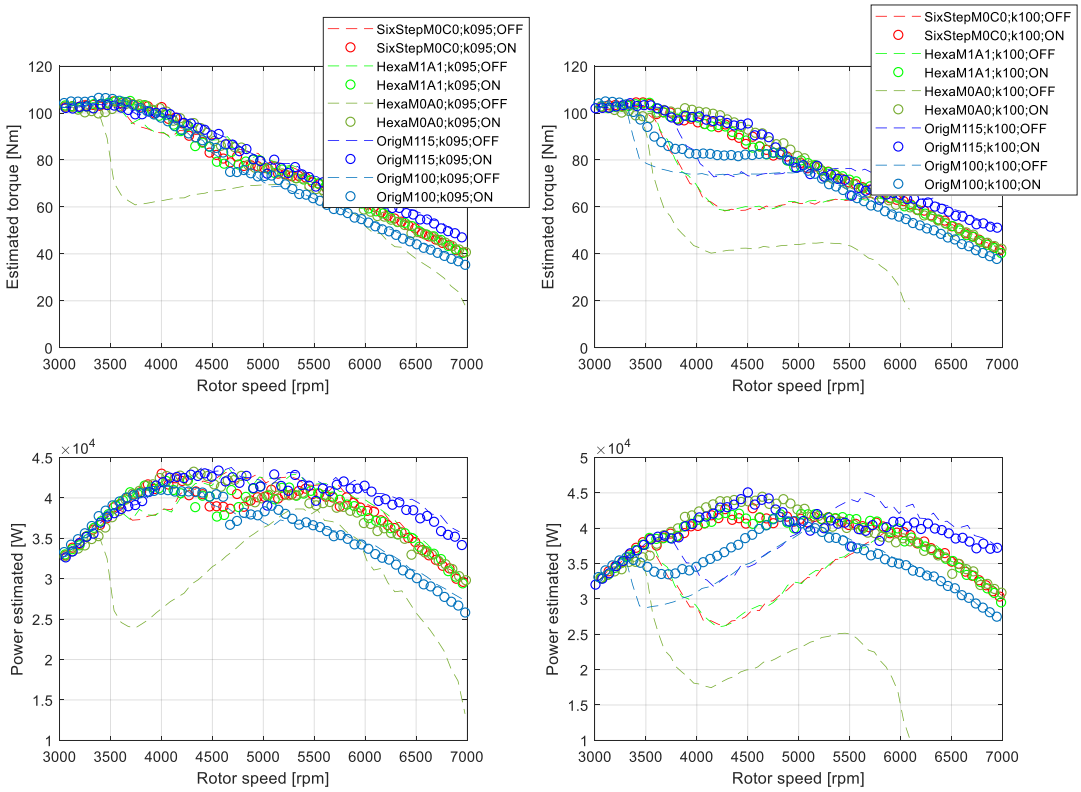

Figure D.9: Zoomed in view of Figure D.8.

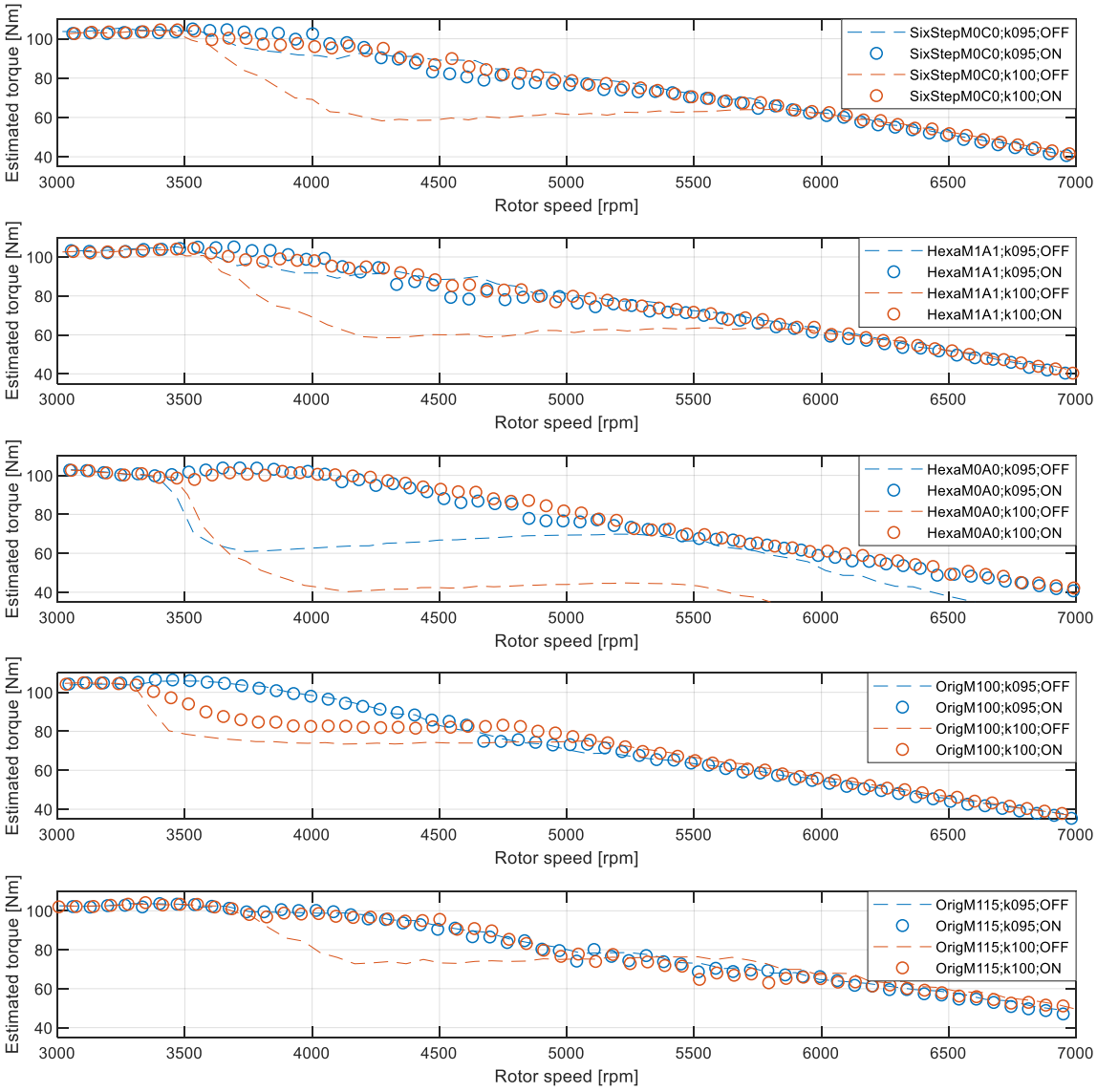

Figure D.10: Maximum torque and power performance with active or inactive dynamic flux weakening reference adaptaiton for two different. Plots separated for each overmodulation strategy.

The new algorithm improves all responses, although there is still a diminishing of the maximum torque for a range for speeds for the linear operation when there is no voltage margin considered (k100 tests). The highest power response is consistently found with the duty saturation overmodulation strategy.